— 4 —

In-Flight Instrument Calibration and Performance Verification

JAMES P. MCFADDEN[1], DAVID S. EVANS[2], WAYNE T. KASPRZAK[3], LARRY H. BRACE[4], DENNIS J. CHORNAY[3], ANDREW J. COATES[5], BRONISLAW K. DICHTER[6], WALTER R. HOEGY[3], ERNEST HOLEMAN[7], KATHERINE KADINSKY-CADE[6], JUSTIN C. KASPER[8], DHIREN KATARIA[5], LYNN KISTLER[9], DAVIN LARSON[1], ALAN J. LAZARUS[8], FORREST MOZER[1], TOSHIFUMI MUKAI[10], KEITH W. OGILVIE[3], GÖTZ PASCHMANN[11], FRED RICH[6], YOSHIFUMI SAITO[10], JACK D. SCUDDER[12], JOHN T. STEINBERG[13], MARTIN WÜEST[14], AND PETER WURZ[15]

[1]*Space Sciences Laboratory, University of California, Berkeley, CA, USA*
[2]*Space Environment Center, NOAA, Boulder, CO, USA*
[3]*Goddard Space Flight Center, NASA, Greenbelt, MD, USA*
[4]*Leelanau Research, Empire, MI, USA*
[5]*Mullard Space Science Laboratory, Holmbury St. Mary, Dorking, Surrey, UK*
[6]*Air Force Research Laboratory, Hanscom Air Force Base, MA, USA*
[7]*Institute for Scientific Research, Boston College, Chestnut Hill, MA, USA*
[8]*Massachusetts Institute of Technology, Cambridge, MA, USA*
[9]*EOS, University of New Hampshire, Durham, New Hampshire, USA*
[10]*Institute of Space and Astronautical Science, Sagamihara, Japan*
[11]*International Space Science Institute, Bern, Switzerland*
[12]*University of Iowa, Iowa City, IA, USA*
[13]*Los Alamos National Laboratory, Los Alamos, NM, USA*
[14]*INFICON Ltd., Balzers, Liechtenstein*
[15]*Physikalisches Institut, University of Bern, Bern, Switzerland*

4.1 Introduction

In-flight calibrations are an essential component of any experiment plan for space-based instruments. These calibrations are necessary not only to verify instrument response and correct for instrument degradation, but also to identify unforeseen changes in response. Verifying proper operation after launch is necessary since the instrument has just experienced large stresses, both thermal and mechanical. In addition, post-launch is often the first time the instrument will experience the full spectrum of spaceflight perturbations, UV photon exposure, and particle flux levels. These perturbations result from the space environment, on-board subsystems, other experiments, or from some combination of these. The experimenter must develop procedures for in-flight testing and calibration of the instrument to assure its proper operation and to provide reliable data to the scientific community.

Once an instrument is launched into space, the science team will spend several weeks in a "commissioning phase" where instrument turn on is done step by step, proper instrument operation confirmed at each step, and inter-experiment compatibility verified. The extended time for this check-out reflects both the limits of real time ground communication, and a general caution during instrument commanding since any mistake could be catastrophic. This check-out does not end with the commissioning phase. Several months of intense data monitoring are normally required just to confirm that the instrument is operating as planned. For interplanetary missions, this commissioning may take place several years after launch. Once proper operation has been confirmed, the instrument team must perform in-flight calibration checks to both confirm and possibly refine the calibrations determined on the ground. In-flight calibrations may be a one-time event to confirm a pre-launch value, or may be an ongoing effort throughout the life of the mission. These calibrations may include "relative calibrations" that account for variations in instrument sensitivity with look direction or particle energy, and "absolute calibrations", which are used to determine overall sensitivity and accuracy of the particle flux measurements.

For some instruments, in-flight calibrations may be the only absolute calibrations possible. Absolute calibration done before launch often requires support facilities with relatively high costs, and may not be practical for some experiments. For other instruments whose absolute calibration is known to change over time, determination of the pre-launch absolute calibration may be an unnecessary step. In this case procedures should be developed to conduct an in-flight calibration that can determine the instrument sensitivity to the accuracy required. The needed accuracy of an instrument can be in the percent range (composition, isotope ratios) all the way to tens of percent. For example, for many single spacecraft missions, absolute calibrations to better than $\sim$30 % may not be necessary in order to fulfill the mission requirements. If the primary measurement is energy spectral shape rather than absolute flux values, an accurate absolute calibration may not be required as long as the instrument relative response can be verified within some general range. However, for multi-spacecraft missions where differences in measurements between spacecraft are critical to the science, careful in-flight absolute calibrations are essential.

This chapter is structured in the following fashion. The first section identifies known sources of instrument degradation, noise and spurious responses that necessitate in-flight calibrations for data validation. The material in this section includes descriptions of problems and, when known, explanations of their origin. Separate sub-sections concentrate on different types of instrumentation.

The next section in this chapter deals with the in-flight procedures and techniques that have been used to expose and correct some of the forms of instrument degradation that were described in the first section. Examples of the results obtained from implementing these procedures on space-flight instruments are provided.

While some missions, for example routine monitoring missions, may require little more than correcting for instrument degradation and spurious sensor response, other missions may require the more difficult step of in-flight determination of absolute instrument calibration. The subsequent sections in this chapter describe the in-flight calibration techniques designed to establish the much more difficult absolute calibration and accuracy of space plasma and particle sensors. Separate sections are devoted to the procedures for establishing the absolute calibration of plasma ($<$30 keV), energetic particles ($>$30 keV), and neutral gas experiments. The material also provides examples of in-flight calibrations that have been performed on single- and multi-spacecraft missions.

Throughout the chapter the material is infused with much of the current "lore" and "experience" gained by those individuals who have performed these tasks. The material points out where in-flight calibrations may fail and where one can be fooled by false agreements. A major objective of the chapter is not only to present useful calibration techniques but also to describe pitfalls and problems in performing these tasks.

For those who attempt these tasks in the future, here is a word of caution: If one can explain away a calibration disagreement, what do agreements tell you? Calibrations require a continuing effort to understand and explain the data.

4.2 Sources of Instrument Degradation, Noise, and Spurious Responses

This section identifies various sources of instrument degradation and discusses how this degradation affects an instrument's response. Degradation is the primary reason that periodic in-flight calibrations are required. Since degradation may manifest itself in the form of noise and since noise removal is required before performing in-flight calibrations, sources of spurious or background noise are also discussed, including those not related to degradation. This material is a necessary prelude to the discussions of in-flight calibration because unforeseen noise will often accompany an instrument's first operation in the harsh environment of space. To the extent possible the problems are characterized quantitatively and, when possible, solutions are provided. Where appropriate, diagnostics that could help identify problems on future experiments are suggested. Much of this discussion centers on the detectors and how radiation, contamination, and extended use affect their life. However, information is also provided on analyzers and associated electronics, in particular how those can contribute to instrument degradation and noise.

The first two sections discuss electrostatic analyzers and electron multiplier (MCP and CEM) detectors, which form the heart of most plasma instruments. A separate section on time-of-flight systems addresses problems associated with these more complex instruments that incorporate carbon foils. These sections are followed by a compact summary of well-known problems with energetic particle detectors. Problems specific to neutral gas instruments and ENA instruments, which incorporate many of the same analyzer and detector systems, are discussed separately. Separate sections are included for Faraday cups, which are frequently used to measure the intense solar wind ion flux, and Langmuir probes that are often used to infer plasma density. This section closes with some examples of unexpected sources of noise that warrant a more extended discussion.

4.2.1 Electrostatic Analyzers (ESAs)

There is no known mechanical degradation experienced by ESAs other than catastrophic failure due to vibration at launch. However, there are a number of processes that give rise to spurious, undesirable, and unexpected responses associated with ESAs.

Response to ultraviolet photons

Electrostatic analyzers do allow several forms of background "noise" to reach the plasma detectors. Perhaps the most serious form of spurious response experienced by ESA plasma

instruments is caused by photons that scatter in the analyzer to reach the detector. In particular, solar UV often produces large background responses in sensors whose aperture faces the Sun. Proper analyzer design must include serrating (or scalloping) the outer analyzer surface and blackening both surfaces. Scalloping the outer plate was found to reduce scattered UV by an order of magnitude in a gold-blackened, top-hat analyzer designed to require a photon to make two reflections to reach the detector [*Carlson and McFadden*, 1998]. Serrating (scalloping) the inner plate was not necessary because three reflections were required to reach the detector from the inner plate.

The Cluster HIA top-hat ion analyzer [*Rème et al.*, 1997] (with $\Delta R/R$=0.065, $R \sim$ 4 cm, scalloped outer sphere, Cu_2S blackening of both spheres) had extremely low solar UV response ($\sim$50 counts s^{-1} peak rate), demonstrating that the technique was adequate. In contrast, the FAST ion analyzers ($\Delta R/R$=0.075, $R \sim$4 cm, scalloped outer plates) and electron analyzers ($\Delta R/R$=0.060, $R \sim$4 cm, scalloped outer plates) used gold-black and experienced peak solar UV background count rates as high as $\sim$650 s^{-1} and $\sim$400 s^{-1}, respectively, indicating gold-black is not as effective. *Zurbuchen et al.* [1995] provided a comprehensive analysis of blackening techniques and concluded that CuO and Cu_2S provide the lowest UV reflectivity.

The electron and ion analyzers in the Low-Energy Particle (LEP) experiment on Geotail [*Mukai et al.*, 1994] used both serrated analyzer plates and carbon blackening (Aerodag G) to reduce the efficiency of counting solar EUV photons by a factor of 10^7. Even then the sensors had a residue response to solar EUV when the Sun was in the field of view that was significant when the instrument was in a low-density plasma regime. In this case modeling, based on laboratory calibrations, permitted a subtraction of the remaining EUV response from the sensor measurements to correct the data.

As the experience with the CELIAS-STOF instrument on SOHO shows, Lyman-α is not alone in producing solar photon background in detectors. STOF was designed to reduce Lyman-α background but was still swamped with spurious response from other UV light that made the sensor usage much more complicated. Although Lyman-α is the most intense solar line, other UV lines can contribute substantially. The integral of the UV intensity from $\lambda = 0$ to 250 nm (corresponding to the work function of carbon) is about a factor of 300 larger than the Lyman-α intensity. *Bamert* [2004] discusses the ground processing correction for solar UV contamination and, after significant effort, STOF can provide usable data.

Other instruments have introduced UV light traps at the ESA entrance aperture, either in lieu of serrated analyzer plates or to add to the UV suppression provided by plate serration. Among those are the PEACE electron instrument on Cluster [*Johnstone et al.*, 1997] and the ASPERA-3 electron spectrometer (ELS) on the Mars Express mission [*Barabash et al.*, 2004].

In addition to spurious responses from photon scatter, solar UV will produce photoelectrons within the ESA whenever the sensor aperture faces the Sun. These photoelectrons will produce a response in detectors when the analyzer is operated to select low-energy electrons. Elimination of this background is probably not possible and necessitates special data handling that can reduce its impact on the measurements. Section 4.4.3 describes in detail how the effect of photoelectrons from the Geotail satellite was handled in the computation of total ion and electron densities.

Scattered Electrons

Scattered and secondary electrons introduce still another form of background in electron ESAs. Electrons impinging at low angle of incidence on the analyzer plate surface have a 50 % or higher probability of scattering with little energy loss and can result in an out-of-energy-band response in ESA detectors. For an incident monoenergetic unidirectional electron beam this scattering can produce a spurious detector response at ESA angles and energies other than the incident beam angle and energy. The magnitude of the problem depends upon details of the ESA design. It often appears in an ESA designed for high geometric factor, such as top-hat analyzers, whose small deflection angle ($<90°$) permits electrons outside the selected energy pass band to pass through with a single scatter.

For these sensors, the amplitude of the response in the wings may be a few percent of that at the nominal central beam energy and extend from about half to twice the beam energy before the analyzer structure forces a second bounce. For broad electron energy spectra, this scattering has a negligible effect. For steep spectra, the sensor response due to electron scattering will set an upper limit to the resolution of high-energy tails in the spectra. For highly peaked spectra, as found in the Earth's auroral zones, internal scattering and secondary electron production can also produce an apparent low-energy component to the electron spectrum. This component is difficult to distinguish from atmospheric secondary electrons and may require complex ground processing for its removal. Ground testing should be undertaken to measure the extent that electrons can gain access to the detector by scattering in the analyzer.

Scattered electrons can also lead to spurious response in ESAs operated to measure positive ions. Top-hat design ion ESAs on the FAST spacecraft experienced increased background counts when intense fluxes of 10 keV electrons were present. Intense electron fluxes below 2–3 keV generally do not pose a problem for ion sensors since the front surface of the detectors (MCPs or CEMs) are typically biased negative at 2–3 kV, preventing these electrons from reaching them.

Scattered Ions

Problems similar to those arising from scattered electrons may also occur for scattered ions. Ions entering an ESA with energies outside the selected passband or angles outside the nominal ESA field-of-view may strike the analyzer plate at glancing incidence and have a small probability of being specularly reflected. Such ions would have a non-zero probability of passing through the analyzer to the detector despite having an incorrect energy-to-charge ratio. This process would diminish, or smear the instrument energy resolution and could produce ghost peaks in the ion energy spectrum. The application of a rough surface coating to the analyzer plates, or employing serrated analyzer plates, would minimize specular reflection by reducing the area exposed for small-angle scattering. *Wüest and Bochsler* [1992] have shown that the application of a CuS_2 coating to the analyzer plates reduces the ion scattering by about an order of magnitude, more so at the extremes of the energy passband than towards the center (Figure 4.1).

Field Emission

Field emission of low-energy electrons from exposed insulating surfaces within the ESA structure can be still another source of spurious response in the particle detector. This can arise when highly insulating metal oxide surfaces (aluminum or magnesium oxide,

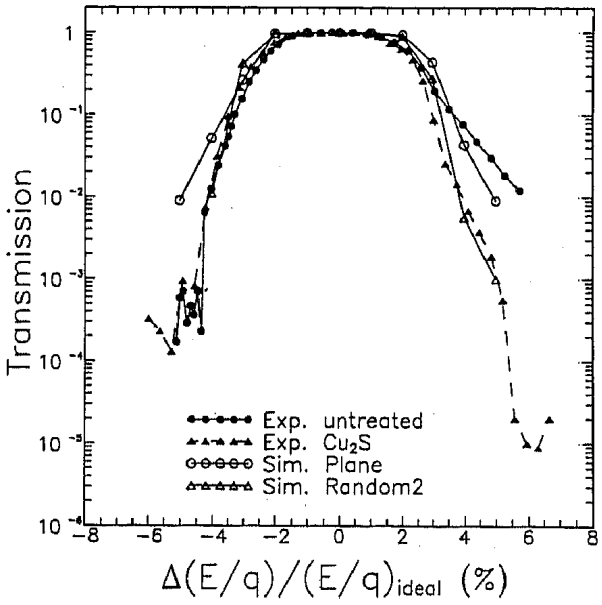

Figure 4.1: Transmission of He^{2+} through a spherical section analyzer (Wind/MASS ESA prototype) as function of the deviation from the nominal incidence energy. The results of experimental measurements, using an untreated and a copper sulfide treated analyzer, are compared to theoretical results obtained from a Monte Carlo simulation that included particle scattering from the analyzer plates. From *Wüest and Bochsler* [1992].

for example) are directly exposed to fluxes of hot plasma and acquire a surface charge. The electric field strength between the charged surface and the underlying conducting metal can become so large that electrons are field emitted from the surface [*Malter*, 1936] and counted by the particle detector. Care must be taken in the choice of materials and to insure that insulating surfaces within an ESA are not exposed to incident plasma or viewed directly by the particle detector positioned behind the ESA plate structure.

High Voltage Problems

Noise counts associated at the highest energy steps of top-hat ESAs have been observed in several instruments. These counts were observed in relatively compact analyzers (R=4 cm), both ion and electron, and when the deflection voltage was ∼4 kV. The magnitude of these noise counts varied from zero to several hundred counts per second among essentially identical analyzers. Field emission or electrical discharges within the ESA is believed to be the cause, possibly due to microscopic variations in blackening. Other than replacing an entire unit, no solution was found for this problem. In what may be a related problem, during thermal vacuum testing for the FAST spacecraft, operator error resulted in several ESAs having their high voltage turned on in poor vacuum resulting in internal arcing. During subsequent operation in high vacuum, these sensors showed a high noise level that increased with the higher deflection plate voltage. Inspection showed that the

insulator supporting the inner hemisphere of the analyzer had discoloration streaks due to surface arcing. Once a surface arc path is formed, there continues to be an arcing problem even in high vacuum. Noise from this arcing was capacitively coupled to the charge sensitive preamplifiers to produce a spurious response. Cleaning the insulators eliminated this source of noise.

ESA electrical failures typically involve the loss of the high voltage sweep supply and hence the complete loss of the instrument. However, there have been partial electrical failures that result in degraded operation. The ISEE-3 electron electrostatic analyzers were designed to sweep in energy from 1.2 to 16 keV. During post-launch testing, the CEM count rates above 8 keV particle energy were observed to be independent of ESA energy setting, whereas it was known that the electron flux decreased dramatically at higher energies. There were no diagnostics available to check the high voltage output. It was postulated that the sweep high voltage supply was prevented from reaching its maximum voltage due to excessive leakage current while the lower energy portion of the sweep worked properly. An extrapolation of the solar wind spectra (measured by a separate instrument) to higher energies was consistent with the 1.2–8.0 keV measurements and dispersion analysis of solar electrons during Type III events confirmed that the lower energy channels were operational. This partial failure, whose cause was never unambiguously determined, was an indication of future troubles and the high voltage supply failed completely after $\sim$15 months. Modern experiments should include diagnostics that directly measure the sweep supply voltage and current to confirm proper operation and diagnose malfunctions.

Opto-coupler degradation

Some of the more recent ESA plate voltage sweep designs incorporate opto-couplers to obtain fast plate voltage sweeps and voltage resets (e.g., *Carlson et al.* [2001]). Historically, ESAs swept particle energy by using a rapid analyzer plate charge to high voltage followed by a slow, exponential (or pseudo-exponential) voltage decay during which particle data were taken. The charging time represented a period when useful data were not collected. Opto-couplers are devices that incorporate light emitting diodes (LED) operated at low voltage to control the conductance of photodiodes that, in turn, govern the charging (or discharging) current delivered from a high voltage supply to the ESA plates. The light signal from the LED is coupled to the photodiode by a light pipe thereby providing electrical isolation between the low and high voltage portions of the system. The LED can be driven by a low voltage signal to modulate the conductance of the photodiode and so tailor the voltage profile imposed on the ESA plates. In FAST two separate opto-coupler systems are used; the first to control the charging of the analyzer plates, which can be made very rapid because of the very high conductance capability of the photodiode, and the second to control a slower discharge phase during which particle data are obtained. Radiation damage to opto-couplers and their drive circuits is a concern. Radiation damage can decrease the conductance of the photodiode for a given illumination, can change the light emission from the LED for a given drive signal, or can change the transparency of the light pipe.

The FAST satellite utilized 24 pairs of opto-couplers (AMPTEK HV601B) in a radiation environment anticipated to be $\sim$20–30 kRad per year after shielding. Ground testing showed the opto-couplers to be fairly rugged, with only a 13 % drop in photodiode conductance after a 98 kRad dose in 8 hours. After 7 years on orbit, all FAST opto-coupler

circuits are still functioning although they have experienced degradation. Analyzer plate charge times have increased from pre launch values of <1 ms to between 3 and 8 ms.

In the case of the 8 ms charging time constant, the analyzer plate voltage only reached $\sim$40 % of the available voltage indicating that the opto-coupler transconductance had decreased by at least a factor of 20. The opto-coupler circuits with the most degradation were those circuits that experienced the largest drive currents. The two most degraded circuits were operated to sweep the ESA from 8 to 30 keV ($\sim$30 mA drive current) every 6.4 ms continuing in that mode at a $\sim$40 % sweep duty cycle for 3 years. During the remaining 4 years those circuits operated in a less stressful mode where the ESA plate voltages remained fixed for about half the time with much reduced photodiode current demand.

In comparison, the two circuits that operated the 2 to 8 keV ESA energy sweep during the same period had their transconductance decreased by only about a factor of $\sim$10. The remaining circuits, which were operated at still lower voltages, retained about 1/3 of their initial conductance for the recharge opto-couplers. There was also evidence that a plate voltage discharge opto-coupler in one of the most highly stressed circuits (8–30 keV ESA energy sweep) has degraded enough ($<1/20$ the initial conductance) that the sweep voltage slew rate was affected over a limited energy range.

These results suggest that opto-coupler degradation is not just a function of the radiation environment but also depends upon the drive current. In the case of FAST, this degradation affected the higher energy steps of the ESA making data analysis difficult. For experiments with opto-couplers that require large drive currents in a high-radiation environment, designing in the ability to increase the plate voltage charge time by ground command will help alleviate the loss of high-energy channels.

4.2.2 Gain Degradation in Electron Multiplier Detectors

While other types of electron multiplier particle detectors have been used in the past (such as the Johnston discrete dynode multiplier), microchannel plate (MCP) and Channel Electron Multiplier (CEM) detectors (see Section 2.2.3) are currently the most common low-energy particle detectors used in plasma sensors. Both devices operate as electron multipliers, with typical output charge pulses of $\sim 10^6$ electrons for chevron configuration MCPs and $>10^7$ for CEMs for a registered ion or electron. Their properties depend on the manufacturing process (glass type, chemical treatment, etc.) and any exposure to contaminants. In general, MCP and CEM properties are similar enough that the following discussions will treat them together. Properties peculiar to one or the other will be pointed out.

MCP and CEMs are known to age. This aging manifests itself in two ways, and both effects must be identified and compensated for in order to maintain the integrity of the observations throughout a space mission. The first is a decrease in electron gain that depends upon total extracted charge and results in a decrease in pulse counting efficiency. This gain decrease is discussed in greater detail below.

The second is a decrease in the efficiency for an incident particle to produce secondary electrons at the entrance aperture of the device necessary to initiate a detectable output pulse. This decrease is primarily related to hydrocarbon contamination. Such contamination may not be initially detectable because a contaminated MCP or CEM may have particle conversion efficiencies similar to clean devices. However, under UV or particle

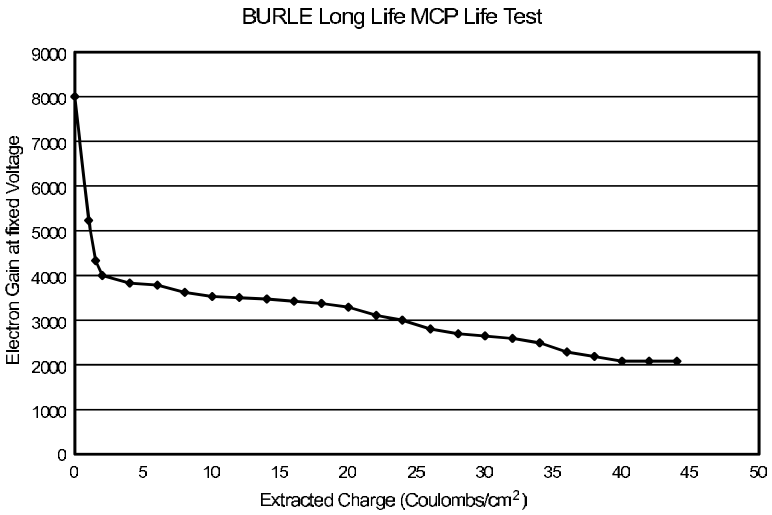

Figure 4.2: MCP gain vs. extracted charge.

bombardment, hydrocarbon chains may form on the sensitive area of the input face of the device, effectively changing its properties. An efficiency decrease may be observed with fewer than 10^{13} counts cm^{-2} for MCPs, which may be less than a mission lifetime. To avoid these problems we strongly suggest washing all detectors in a 50:50 mixture of isopropanol and methanol, followed by baking at 100 °C for ∼30 minutes.

New MCPs and CEMs show an abrupt decrease in gain early in their life. This initial decrease is believed to be related to changes on the interior surface where contaminants (adsorbed gases, water vapor, etc.) are slowly scrubbed away by electron bombardment. Typically the detector bias voltage must be raised several times during the first few months or years of operation to compensate for this gain decrease. After the initial scrubbing period, the devices exhibit a rather slow decrease in gain that will still require monitoring, but usually with less frequent changes in bias voltage required. The initial gain decrease can be avoided by performing scrubbing prior to launch [*Martin et al.*, 2003], but this will necessitate subsequently maintaining the detectors isolated in a high vacuum or a dry nitrogen purge.

Because of their large collecting area and ability to resolve the spatial location of an event on the surface of the device, MCPs have become the low-energy particle detector of choice on recent space missions. However, MCPs also have a finite operating life. Testing indicates that the total charge per unit area that can be extracted from the MCP is between 10 and 100 C cm^{-2} before the device becomes unusable (Figure 4.2). This limit appears to be due to changes in the micro-pore glass due to alkali metal migration. While the progressive decrease in MCP gain can be compensated by increases in the bias voltage, eventually the voltage capability of the bias supply may reach its limit or voltage breakdown within the MCP may occur. This suggests that it is better to operate the MCP at the lowest acceptable gain to maximize lifetime.

MCPs have been used in a number of experiments and scientific missions in recent years. Considerable, and very diverse, experience has been accumulated concerning MCP

lifetimes in terms of total charge extracted from the device leading to some possible insight into those factors that govern total lifetime. Among those factors that may play a role are the selection of bias voltage to optimize the pulse height distribution (PHD), the length to diameter ratio (L/D) of the MCP pores, and the MCP resistivity that is often tailored to improve the count rate dynamic range of the device. The following details some representative examples of MCP lifetime and makes suggestions for procedures that may improve operating lifetime.

The MCPs in the Wind 3D Plasma (1994 launch) and FAST ESA (1996 launch) instruments continue to function normally after many years on orbit. The Wind 3D Plasma, EESA-L, sensor (180° FOV) has experienced the largest integrated fluxes, with a total count estimated as of late 2003 to be $\sim 10^{14}$ or $\sim 8\,\mathrm{C\ cm^{-2}}$ of charge extracted from the device active area. The EESA-L sensor used MCPs manufactured by Mullard (currently Photonis) in the form of half-annulus rings L/D=80 with resistivities of $\sim 400\,\mathrm{M\Omega\ cm^{-2}}$. Bias voltages were increased several times during the first two years of operation (from 2.2 kV to 2.4 kV), but no further increases have been required in recent years. These MCPs were not scrubbed prior to flight, so the initial voltage increase was likely necessitated by gain loss from in-flight scrubbing. The Wind high voltage supply currently has an additional 1.2 kV of capability for future voltage increases.

The FAST analyzers used Galileo (currently Burle), higher-current, larger-pore MCPs ($\sim 180\,\mathrm{M\Omega\ cm^{-2}}$, L/D=40) with the same overall dimensions as the MCP used in the EESA-L instrument. MCP bias voltages were initially set between 1.7 and 1.9 kV, and were increased to 1.9–2.15 kV after 7 years operation. Typically the major increase in bias voltages on the FAST MCPs were required during the first and second year of operation with additional increases not required until much later in mission life. The required voltage increases varied among individual MCPs with the smallest bias voltage increases (100–150 V) associated with those MCPs that started the mission at higher voltage. The largest bias voltage increase ($\sim$400 V) was for a sensor that experienced identical fluxes to a sensor with the lowest bias increase ($\sim$100 V), suggesting that the MCP gain loss was not strictly a function of integrated counts. Both these sensors currently have similar bias voltages indicating that the primary difference between those two MCPs was their change in response during early orbit scrubbing. The MCP in the FAST electron ESA (360° FOV) has experienced an integrated count of $\sim 8\times 10^{12}$, or $\sim 0.34\,\mathrm{C\ cm^{-2}}$ extracted from the MCP active area, with no signs of degradation. This sensor required a $\sim$250 V increase in bias voltage during the first two years, with only an $\sim$100 V increase during the following 4 years. The rather small gain loss after initial scrubbing was typical of all 16 MCPs on FAST indicating gain losses occur rather slowly for the fluxes encountered during this mission.

Unlike the FAST and Wind MCPs, the Cluster/PEACE MCPs required significant bias voltage increases during the first 2 years of operations. Figure 4.3 shows the gain history of the LEEA and HEEA MCPs on one of the Cluster spacecraft. The periodic increases in MCP gain are associated with bias voltage adjustments. In the absence of such adjustments, the MCP gains decrease by nearly a factor of 10 over several months of operation.

The PEACE electron plasma analyzers used Philips (currently Photonis), chevron-configuration MCPs with 12.5 μm pores, L/D of 80, and pore bias angles of 13°. The plates were not scrubbed prior to flight. Initial bias voltages of 2.8 kV were required for an average gain of $\sim 2\times 10^6$. During the first two years of operation, the sensors have seen total counts estimated at $2.6\text{–}3.6\times 10^{12}$ (currently being corrected for counts below

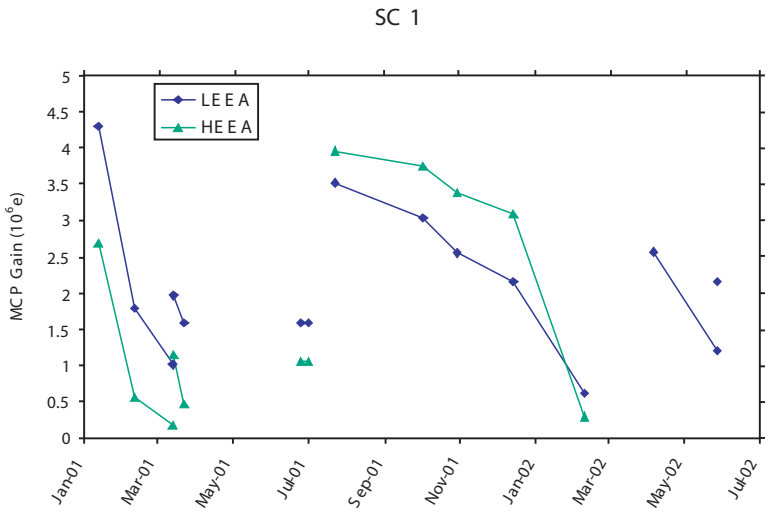

Figure 4.3: The time history of the MCP gains in the PEACE LEEA and HEEA analyzers on Cluster SC1. The periodic increases in gain are due to changes in MCP bias voltages. These MCPs suffered significant gain losses over periods of only a few months of operation.

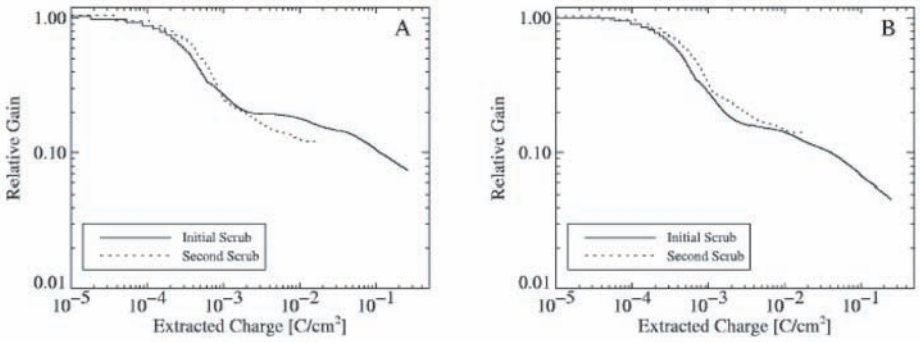

Figure 4.4: Relative gain as a function of charge extracted for the scrubs of the two MCP segments A and B of the COS-FUV01 instrument on HST. From *Martin et al.* [2003].

threshold) for the Low-Energy Electron Analyzers (LEEAs) and $3.6–4.4\times10^{12}$ for the High-Energy Electron Analyzers (HEEAs). Corresponding charge extraction is estimated at 0.38-0.6 C and 0.47–0.84 C (0.042–0.067 and 0.052–0.093 C cm^{-2}). Significant gain drops were observed and compensated by voltage changes, which were between 450–570 V for the LEEAs and 570–800 V for the HEEAs. In general, larger changes were required for MCPs with lower gain. This relatively rapid decrease in gain has required MCP bias voltages to be increased to near the HV supply limits. To increase instrument's lifetime, the sensors are no longer operated at their full duty cycle, with some sensors turned off in high flux regions such as the magnetosheath.

What has caused the unexpected degradation of the Cluster/PEACE MCPs? The results of *Martin et al.* [2003] on the scrubbing profile of MCPs (Figure 4.4) show that scrubbing continues until more than 0.1 C cm^{-2} charge has been extracted. Since the charge extracted from the PEACE MCPs was rather small (<0.1C cm^{-2}), those devices should have been still experiencing scrubbing and not have been anywhere near the lifetime charge extraction limit.

Similar MCP cleaning and contamination control (dry N_2 purge) were implemented for all these projects. Internal insulators were similar low outgassing materials, such as PEEK (Polyetheretherketone), Kapton, Polyimide, Glass Laminate, Vespel, Ultem, and Macor. In addition, the Cluster/HIA sensors experienced identical pre-launch environments as PEACE but have shown no signs of degradation other than early orbit scrubbing. A possible and likely explanation is that the PEACE design required too high an MCP bias voltage at the mission start, and that subsequent voltage increases to compensate for scrubbing quickly used up the additional range of the HV supplies. PEACE used microchannel plates with L/D=80, which require higher bias voltage in the Chevron configuration than plates with L/D=40 would for the same gain. This lower gain can be compensated by either using a thin spacer (∼0.025 mm) between the plates to increase the number of microchannels firing in the second plate, or by increasing the bias voltage. The PEACE team chose to increase the bias voltage because this resulted in narrower MCP pulse height distributions (see PHD, Section 2.2.4 for a discussion) at mission start, and therefore better performance with fewer charge pulses near their preamplifier threshold. However, a high bias voltage (∼1.4 kV per plate) was required to get the peak in the PHD ($\sim 2 \times 10^6$) well above their preamplifier threshold ($\sim 4 \times 10^5$), which meant the plates were being driven near their gain limit. Subsequent small drops in gain due to scrubbing required large voltage increases to compensate, resulting in some sensors being driven at the HV supply upper limit after only <0.1 C cm^{-2} charge extraction. In retrospect, a better solution may have been to use a spacer between the MCPs and accept less than ideal PHDs early in the mission. We note that for plates with L/D=40 in Chevron configuration, spacers are not required for gains of $\sim 2 \times 10^6$ with modest (∼1 kV per plate) bias voltages.

Monitoring and compensating for gain loss in MCP detectors is complicated by the fact that gain loss is often not uniform over the sensitive area of the device. For example, a solar wind ion detector may have the bulk of its count rate confined to a small portion of the MCP area, as is the case for the Wind 3D Plasma and Cluster/HIA sensors. This can cause the gain to decrease more rapidly over a part of the detector requiring an increase in bias voltage. However, this leads to excessively high gain in other parts of the MCP and may result in higher noise levels. This problem can be mitigated with proper laboratory MCP scrubbing, however it may be better to avoid this problem by designing the instrument so that the MCP sensitive area is more uniformly exposed to the incident particles. For example, a top-hat ion ESA could be designed so its 360° planar FOV responds to solar wind ions in a spacecraft spin plane oriented to correspond to the ecliptic plane. This would produce a uniform dose on the MCPs since the solar wind is generally confined to the ecliptic plane. Deflectors at the ESA entrance could be used to provide a small out-of-plane measurement of the solar wind. In principle, this arrangement could also provide extremely fast measurements of the solar wind independent of spacecraft spin.

A final point of caution. Instruments that incorporate MCPs are often designed with safety features that shut off the experiment if too much detector current is drawn. The threshold current level for these features should be adjustable in-flight since MCP currents

change substantially during the mission, for example with increases in MCP bias voltages to compensate for gain loss. MCP resistance also decreases with increased temperature, so currents will rise when the instrument gets hot with the potential for destructive thermal runaway . To prevent this problem, current trips or limiters should be included in the high voltage supply design together with adequate heat sink capability in the MCP mounting structure.

Section 4.2.9 describes in greater detail some instances of subtle and, as yet, unexplained, cases of noise counts arising from MCP and CEM detectors.

4.2.3 Time-of-Flight Detector Systems

Time-of-flight (TOF) systems are inherently less susceptible to noise because of the coincidence requirements for a measurement. In order to count as a valid event, two or three signals must be triggered within a set time window. For example, an ion must trigger a "start," a "stop" and perhaps also a "position" or "energy" detector. Thus, a random penetrating particle from the radiation belts that results in a single count on one detector is not counted as an event, and so does not create background. Only when the rates are high enough that random counts are measured for "start" and "stop" and "position" will they actually be counted as an event in the instrument. Cluster/CODIF measures singles rates of 30,000 counts per second (cps) from penetrating ions from the radiation belts. Despite this high rate, CODIF can still measure the ion composition, while the background severely degrades the Cluster/HIA electrostatic analyzer measurements.

Time-of-flight mass spectrometers typically use thin carbon foils, which are traversed by the particle to be registered, to create a start signal. The passing particle (an energetic ion or atom) releases secondary electrons both on the entrance and the exit side of the carbon foil. Depending on instrument design either the entrance or exit electrons are guided to a detector for the start pulse. The yield of secondary electrons depends strongly on the chemical nature of the surface (the outer-most layer). When at air all surfaces are covered with a thin water layer, possibly creating a thin oxide layer. Other residues from processing the carbon foil may also be present initially. Typically, these surface coatings increase the secondary electron yield. Since this layer is thin it evaporates with time in vacuum (e.g. during the mission) or is sputtered away and the secondary electron yield is reduced by a factor two to six when reaching a clean carbon surface. This results in a degradation of the start efficiency or total electron yield and cannot be separated from a gain reduction of the start MCP. For example, for the MTOF sensor of the CELIAS instrument on SOHO the start rate decreased by a factor of 3 during the first 2 years of operation, which is mostly attributed to the decrease in secondary electron yield of the carbon foil (F. Ipavich, private communication).

Time-of-flight instruments are limited in their maximum count rate for two reasons. First, the dead time is significantly longer for TOF instruments because of the length of time required to process each event. For Cluster/CODIF, the time to process an event is 5.25 μs, including acquiring the event, calculating the time-of-flight, and validating the coincidence requirements. Dead time effects are evident at 20,000 cps, but can be corrected up to 200,000 counts per second (see Section 3.1.3 for discussions of dead time). The larger problem at high rates is a background generated by false coincidences. If the rate is high enough, more than one ion may enter the instrument during a measurement and there is no way to determine if the "start" signal and "stop" signal come from the same ion. As

the rates get higher, a background of false coincidences is generated from unrelated starts and stops. This effect is worse if the individual efficiencies are low, since there is a larger chance to have "start" with no "stop," or a "stop" with no "start." Cluster/CODIF exhibits these types of background events contaminating the minor ions when it observes proton rates of about 5000 counts per seconds at one angle and energy. These rates are commonly observed when using CODIF's high geometric factor section within the magnetosheath. There is almost always a background generated in the magnetosheath which contaminates the measurements of minor ions like O^+ at the energy and direction of the main flow.

In addition, time-of-flight systems use Micro Channel Plates for their "start" and "stop" signals, and these detectors are subject to degradation as was discussed earlier. Systems that use the same MCP for the "start" and "stop" signal can have the problem of non-uniform gain degradation. In the design used for the FAST/Cluster/Equator-S series of instruments, focused electrons generate the start signal, while the stop signal is generated by the ion impacting the MCP. Because the ion scatters in the entrance foil, the position of the ion on the MCP is much less focused than the position of the electrons. As a result, the start efficiency degrades faster than the stop efficiency. For Cluster/CODIF, the stop efficiency is still at 80–90 % of its initial value after the first three years of the mission, while the start efficiency has degraded by ∼50 %. As a result, the MCP voltage cannot be raised any further because that leads to too high a current for the stop signal, which disables the high voltage power supply. Therefore the instrument is forced to operate with reduced efficiencies. Using separate MCPs with separate control voltages would alleviate this problem. Similarly, the TEAMS instrument on FAST suffered greater MCP degradation in the positions that looked in the ram-direction of the spacecraft. Since the degradation was not uniform, the MCP voltages could not be raised enough to compensate without disabling the high voltage power supply.

The methods used for verifying MCP gain are described in Section 4.3.1.

4.2.4 Energetic Particle Detectors

Silicon solid-state detectors (SSDs) used to detect energetic particles suffer damage from the very particles that they are designed to measure. The damage can be classified into two types: bulk and surface damage. The first type occurs when an incident particle collides with a Si atom in the crystal lattice displacing the atom from its location in the lattice. The displaced atom and the resulting vacancy form a defect in the lattice (sometimes termed a Frenkel defect), that is capable of trapping a charge carrier for periods of time ($\sim$ ms) long compared to the charge collection time for the circuit reading out the Si detector ($\sim \mu$s). These defects, scattered through the volume of the sensor, decrease the ability for ion-electron pairs produced by an incident particle to be completely collected during the circuit integration time resulting in misidentification of particle energy. In space applications, lower energy protons are the primary cause of lattice defects both because they are plentiful and because their damage is concentrated near the surface of the detector. Protons, even with energies of only a few keV, create defects readily. In fact, incident protons can create clusters of many defects along their stopping path. Electrons, on the other hand, require at least 250 keV to have an appreciable chance of creating a defect, with a very small probability of creating a second one. Since the proton damage is predominantly near the surface of the detector, the reduced charge collection primarily affects the lower energy particles being measured, effectively increasing the detector's dead layer.

The production of bulk lattice defects also results in increased leakage currents through the detector. The primary effect of increased leakage current is degradation of detector energy resolution. A large enough leakage current can result in noise appearing in the lowest energy channels. Increased leakage current can also result in a lowering of the bias voltage applied across the detector because of an increased voltage drop across the series bias resistor in the voltage supply. The reduced detector bias voltage reduces the depletion layer thickness and contributes to lowering the fraction of the charge collected. This latter problem can be mitigated by designing for bias voltage increases during the mission.

The second type of defect, a surface defect, is also produced by the impact of particles on the detector structure but is localized at or near the surface electrode. The net result of a surface defect can be increased leakage currents, increased dead layers, or damage to the detector junction. The energy broadening due to increased surface leakage current introduced by surface defects can be nearly eliminated by detector designs that use separate metal rings at the detector edge to collect these edge currents. High fluxes of low-energy ions that penetrate only the outer exposed surface increase the dead layer (as discussed above) causing the detector noise to increase with time. Most detector designs have the blocking or junction surface facing inward, reducing radiation damage to the device. Operating with the junction surface exposed to space can have the beneficial effect of reducing the dead layer and decreasing the minimum detectable particle energy. However, this will be at the expense of increasing the device's exposure to intense low-energy ion fluxes that may eventually cause the detector to fail.

A population of protons stopping near the surface can cause both types of degradation to occur. Low-energy protons are particularly damaging because of their short ranges in Si. Protons with energies below 100 keV have a range less than 1 μm in Si resulting in both surface and lattice defects. Significant degradation effects can be expected after an irradiation of 10^{12}–10^{13} protons cm^{-2} [*Knoll*, 2000]. In contrast, 10^{14} protons cm^{-2} with energies $>$ 250 keV will result in similar degradation.

Particle radiation damage can impact other types of solid-state detectors in exactly the same way as occurs in energetic particle SSDs. An example of such degradation was observed in an instrument on NASA's Chandra X-ray observatory. After only a few weeks on orbit, a solid-state Si CCD began to suffer performance degradation. The problem was traced to proton damage of the highly sensitive surface region of a CCD containing thousands electronic circuits deposited on the Si chip. Calculations showed that protons with energies above 80 keV had access to the device by undergoing grazing angle scattering from the X-ray mirrors resulting in surface and bulk defects. Further degradation was avoided by moving the detector into a shielded region whenever the spacecraft was exposed to high fluxes of low-energy protons in the radiation belts [*Dichter and Woolf*, 2003].

In summary, radiation damage to solid-state detectors can, over time, lead to greatly increased detector noise and degraded energy response. Section 4.3.3 describes in more detail the evidence for radiation damage in the performance of the solid-state detectors on the NOAA/POES satellites. Examples are given of both the impact of increased noise on the response of one solid-state detector telescope and the impact of reduced charge collection on the performance of detectors exposed to fluxes of low-energy protons. Section 4.3.3 also shows examples of the magnitude of the changes experienced in detectable proton energies as a result of this damage, deduced from inter-satellite comparisons of sensor responses between newly launched and long-operating instruments.

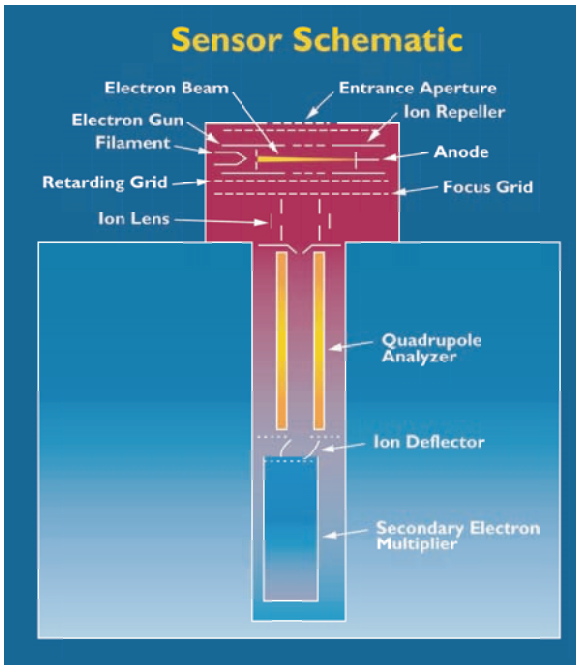

Figure 4.5: Schematic of the ONMS instrument.

4.2.5 Neutral Gas Instruments

The neutral gas mass spectrometer is designed to measure the ambient gas composition. These instruments use MCP and CEM detectors and so are subject to some of the same problems described in Section 4.2.2. Identifying and correcting for degradation of those sensors would follow the procedures discussed in Section 4.3.1 and an example specific to the Cassini INMS is described there. Anomalies have also been encountered in neutral gas mass spectrometer data while operating in space that are beyond the mainstream experience with similar instruments and warrant further discussion.

Niemann et al. [1980b] has described a problem encountered in low altitude (near or below 150 km) thermosphere measurements with the Pioneer Venus Orbiter Neutral Mass Spectrometer (ONMS). As seen in Figure 4.5 this instrument has a series of grids in the ion source [*Niemann et al.*, 1980a] with the ion repeller grid near +40 volts. Other grids between the grounded entrance aperture and the ion repeller reject ambient low-energy electrons. At low altitudes where the CO_2 density was high, the spacecraft speed of 9.8 $\mathrm{km\,s^{-1}}$ produced a high CO_2 flux that sputtered trace alkali metal ions (Na^+, K^+ and Ca^+) from the gold plating of the positively charged ion repeller grid. The variation of the instrument signal as a function of the angle between the normal to the entrance aperture and the spacecraft velocity vector was significantly different from that expected for the ambient gas. The ions were detected whenever the velocity vector was nearly aligned with the instrument axis. This variation along with the observed mass-to-charge ratios formed a diagnostic tool for the anomaly.

An additional spurious ion signal was observed in the ONMS data at a mass-to-charge ratio of 19. This signal was most likely due to fluorine (F) desorbed from grids and surfaces under electron bombardment or from the filament itself. The signal was not spin modulated or related to the ambient atmospheric flux but did gradually increase in magnitude over the 14-year life of the instrument. Similarly designed instruments with filament ionization sources also show this characteristic mass 19 peak.

Another type of problem arises when background gases are emitted from the surrounding ion source surfaces at mass-to-charge ratios that interfere with those produced by ambient gases. In this case it is necessary to subtract the background contributions due to the desorbing species. Usually there is a drop in the magnitude of surface outgassing over time. Typical background gases in the ONMS ion source, after the source was opened prior to entry into the ambient atmosphere, were H_2, CH_4, H_2O, CO, and CO_2 at very low count level. However, many of the background contaminant gases were renewed each orbit from surface reactions as a result of low altitude exposure to ambient atomic oxygen. In fact, not all surface reactions are necessarily bad. For ONMS [*Niemann et al.*, 1980b; *Kasprzak et al.*, 1980] the reaction O(wall) + O(gas) $\rightarrow$ O_2(gas) and O(wall) + N(gas) $\rightarrow$ NO(gas) stabilized after about 20 orbits such that O_2 and NO were used as a measure of O and N, respectively, in the ambient atmosphere.

Ultraviolet light can also be a source of background. The ONMS instrument had its ion source, quadrupole mass analyzer and Cu-Be, box and grid, multiplier detector on a co-linear axis. The spacecraft orbit was nearly polar with a spin axis normal to the ecliptic plane and the ONMS axis at 30° angle with respect to the spin axis. On the dayside of Venus during certain parts of the spin period and orbit, the sensor detected a background signal due to ultraviolet light scattered from the planet's clouds. This signal was of the order of several counts per second and independent of the mass-to-charge ratio. A similar signal seen near midnight was correlated with an intense UV emission observed by the Ultraviolet Spectrometer. Geometry calculations confirmed that the signal was observed only when light from the planet could enter along the instrument axis, unaffected by the quadrupole mass analyzer, and reach the detector.

Another source of background was observed when the INMS instrument sampled close to Saturn. Laboratory calculations indicated that measurements of low densities in Saturn's magnetosphere by the INMS [*Kasprzak et al.*, 1996; *Waite et al.*, 2004] would be difficult due to radiation background contaminating the CEM detectors. A tantalum shield was placed around the detector housing to reduce the background radiation level. Backgrounds of this type are identified as a mass independent signal when a mass scan is performed with the quadrupole mass analyzer and must be subtracted from the data in all mass channels.

Desorbing gas species from the exterior of the satellite can also interfere with the measurement of ambient species. Generally speaking, a gas inlet design whose field of view (field of response) does not include satellite surfaces precludes this from happening in a free molecular flow regime. However, in the case of INMS, the original mounting of the instrument on the Cassini spacecraft was on the same surface as a forward firing thruster. Earlier, *Scialdone* [1972] performed calculations on the condensation region in front of a satellite that resulted from impinging neutral ambient particles. These reflected particles form a stagnation region ahead of the satellite and potentially can contaminate ambient gas measurements. An experimental test on the Atmosphere Explorer satellite AE-D using a mass spectrometer and a neon gas jet source was done to determine the return flux due to scattering [*Scialdone et al.*, 1978]. Using a similar calculation technique, it was shown that

at low altitudes on Titan (high gas densities), Cassini orbiter thruster gas products would be scattered backward into the INMS field of view [*Waite et al.*, 2004]. The thrusters were relocated on an orthogonal axis to circumvent this problem.

Although instrument mechanical misalignments are not properly an anomaly, they can cause measurement problems in instruments with narrow fields of view (FOV). The CONTOUR (COmet Nucleus TOUR) Neutral Gas and Ion Mass Spectrometer (NGIMS) [*Mahaffy et al.*, 2002] has an open ion source that was designed to measure both ion and neutral species at high flyby speeds (28 km s^{-1} for comet Encke). The FOV of the source is only 6° by 2°. As mounted on the spacecraft, the bore sight of the open source was misaligned with the main spacecraft axis by ∼0.6° (specified to be ±0.1° rotational alignment about the spacecraft axes). The bore sight of the open source was measured optically relative to a fixed optical cube on the sensor and later referenced to the master optical cube on the spacecraft. An analysis of the data demonstrated that a misalignment of 0.6° resulted in nearly a factor of 2 loss in signal compared to that at 0°. Mechanical methods of correcting the problem were not feasible because the instrument was already mounted in the dust shield of the spacecraft when the comparison with the master cube was made and there was no time left in the integration schedule. Eventually a solution was adopted that involved the reorientation of the spacecraft near closest approach, with minimal impact on the optical instrument pointing. The determination of the alignment of instruments such as the NGIMS with a narrow field of view is important both in the laboratory during calibration as well as when mounted on the spacecraft.

4.2.6 ENA instruments

Energetic Neutral Atom (ENA) instruments have many components in common with ion instruments, however at lower particle energies additional elements for registering or ionizing an ENA are necessary [*Wurz*, 2000]. As final step in the particle registration, ENA instruments also use MCP, CEM and solid-state detectors and thus are also subject to the same problems described in Sections 4.2.2 and 4.2.4.

At the lowest energies, 10–1000 eV, neutrals must be ionized for successful detection and analysis. Ionization of ENAs is done via surface ionization where an electron is transferred from a specially selected conversion surface to the neutral particle when scattering off this surface under a glancing angle forming a negative ion [*Wurz*, 2000]. This ionization process is very sensitive to the chemical nature of the conversion surface. For example, the LENA instrument on the IMAGE mission used a tungsten conversion surface covered with a thin water-oxide layer, like most metals that have been exposed to air [*Moore et al.*, 2000]. This thin layer improved the ionization efficiency by about a factor of 3. In space the water-oxide layer would have disappeared by evaporation and sputtering except that the perigee of the IMAGE satellite was low enough so that exospheric oxygen replenished the oxide layer on the conversion surface and maintained constant ionization efficiency for the mission duration.

Because ENA instruments have straight entrance systems, they are much more susceptible to contamination by UV light. Since ENA instruments typically have large geometric factors due to low ENA fluxes, UV light from stars and interstellar Lyman-α background causes a noise signal that may be in the same range as the actual signal. If ENA instruments are also imaging instruments, the susceptibility to UV light can be used to check and improve the knowledge of the instrument in space. For example, the pointing knowledge

of the GAS instrument on Ulysses has been improved using the UV signal from 70 stars with positions well known from star catalogues [*Witte et al.*, 2004]. Another example of the UV susceptibility of an ENA instrument is the Neutral Particle Detector (NPD) of the ASPERA-3 instrument on Mars Express [*Barabash et al.*, 2004], which is a TOF instrument designed to register ENAs in the energy range of 100 eV to 10 keV. The singles rates are typically 10^4 s^{-1} for the start and 10^3 s^{-1} for the stop detector because of the registered UV photons. The actual ENA counts (TOF coincidence) are in the range up to a few 10 s^{-1} with a UV background in the range of 0.1–1 s^{-1} because of accidental coincidences. The susceptibility of the NPD sensor for UV photons could even be used to measure the UV air glow of the Martian exosphere [*Galli et al.*, 2006]. Finally, most of the UV sources in the sky are relatively constant over time, thus the signal resulting from registering UV photons can be used to check on the time dependence of the instrument efficiency, e.g., start and stop detector gains.

4.2.7 Faraday Cup Instruments

As pointed out in Sections 2.2.1 and 2.4, plasma measurements that employ Faraday cups do not require electron multiplier particle detectors whose properties depend critically on surfaces that change with time. The stability of a properly designed Faraday cup instrument depends, essentially exclusively, upon the stability of electronic circuits and components that, with careful design and component choice, can be achieved. Faraday cup sensors can achieve great long-term stability as is shown in Section 4.3.6.

Nevertheless, Faraday cups are susceptible to mechanical noise that can couple to their suppressor grid. Vibration of the suppressor grid will introduce small currents at the collector plate due to $V\mathrm{d}C/\mathrm{d}t$, where V is the grid voltage and C is the capacitance between the grid and collector plate. Vibrations change the gap between these surfaces that changes the capacitance. Currents as large as $(2\text{–}3)\times10^{-13}$ A were experienced by one of the two Faraday cups on Wind when an adjacent tape recorder was in use. This noise introduced negligible errors in the density measurements since it was 2–3 orders of magnitude below typical currents measured looking into the plasma flow. (Eventually that recorder failed, and the other recorder introduced negligible vibrations probably due to its greater distance from the instruments).

A similar problem was experienced by the PLS experiment on the Voyager spacecraft. In that case, a stepper motor for the LECP cosmic ray telescope introduced vibrations as the telescope changed its orientation. This was unfortunate because the vibration could have easily been reduced had the stepper motor manufacturer known about the concern for mechanical noise. The vibrations induced in the PLS grids are damped quickly enough that the issue was resolved simply by pausing PLS measurements during the actual movement of the LECP motor.

For spacecraft containing Faraday cups, a mechanical noise cleanliness specification is advised, and it is important that the spacecraft builders be reminded of its existence. If a spacecraft is known to produce mechanical noise, there are mechanical approaches that can reduce the problem. For the ALSEP lunar mission, grids were made from perforated thin metal sheet, producing much stiffer grids that would experience negligible deformation. This solution has some drawbacks including mass and reduced transparency. For the Triana mission the Faraday cup was to be placed near the filter wheel for the main telescope, which contained a stepper motor. Mechanical isolators, essentially mounting

bolts enclosed in steel wool, were used to damp vibrations from the spacecraft. Another approach is to reduce the sensor's response to frequencies in the acceptance band of the electronics. On the Wind spacecraft, care was taken to control the resonant frequencies of the grids by adjusting their tension. The modulator ran near 200 Hz and the resonant frequencies and their harmonics of the sensor grids were adjusted to be lower than that frequency. It is important to realize that the quality factor, Q, of the grid vibration may be increased in a vacuum where damping is reduced. On Voyager, the measured Q of early design grids, were increased by factors of 100 compared to their Q at normal pressures. The grids for Wind were made of knitted tungsten wire and did not show an appreciable change in Q in vacuum. In any case, it is important to measure the vibration response of grids as part of the calibration effort.

4.2.8 Langmuir Probes

The use of Langmuir probes to measure the local plasma environment may conveniently be divided into two plasma regimes, high-density low-temperature ionospheres and low-density higher-temperature regions. In the first regime the Langmuir probe is normally operated in a mode where the collection current is measured as a function of an impressed voltage (Section 2.3). The current-voltage relation provides information about both the electron density and temperature. In the second regime the current-voltage relation does not reflect the local plasma properties because currents are dominated by photoemission currents from the probe, or by collection of photo-electron currents from surfaces adjacent to the probe or from the spacecraft. In low-density regimes, Langmuir probes are generally driven at a fixed current corresponding to 10 %–50 % of the photoemission current. The probe then floats to within 1–2 volts of the plasma potential and the probe potential is measured relative to the spacecraft. The spacecraft potential is primarily a function of the ambient electron density, with a weak electron temperature dependence [*Escoubet et al.*, 1997]. Instrument degradation in these two regimes are discussed in turn below. Section 4.3.7 provides a discussion of in-flight techniques for identifying these problems.

4.2.8.1 Current-Measuring Probes

As pointed out in Section 2.3 describing the design and operation of Langmuir Probes (LP), the basic data obtained is the curve relating the voltage applied to the probe and the current collected. For a plasma in thermal equilibrium, there always should be a characteristic current-voltage ($I - V$) curve as described earlier. Contamination on the surface of the probe, that may introduce a non-uniformity in the work function of the probe surface, can distort the ($I - V$) curve. This, in turn, can introduce errors in recovering the plasma parameters.

While the collectors may have been cleaned prior to launch, they can be re-contaminated during the launch phase or by outgassing from the spacecraft after orbit has been achieved. The contaminating material then can experience chemical changes under the action of solar EUV radiation and exposure to thermospheric atomic oxygen. If the resulting contaminating layer is a poor conductor and is not uniformly distributed, different areas of the surface may charge to different potentials, thus producing energy smearing of the electron retarding region that significantly affects the T_e determination as described above. Surface contamination has its greatest effect at high densities because the correspondingly

larger currents produce larger voltage drops across the insulating surface layers. While the voltage drop may be smaller at low densities, the discharge time of the insulating layer will be longer because the ion and electron fluxes from the ionosphere are lower. This effect can be seen as an exponential discharge signature in I_i at the beginning of the ion saturation region immediately following the retrace of the saw tooth sweep (from positive to negative). Such signatures were observed in curves from the AE-E probes later in that mission. The use of redundant LP sensors made it easier to detect the presence of surface contamination, since the different probe locations may lead to different degrees of contamination and different delays in their onset.

In anticipation of the possibility of contamination, the AE-C, D and E probes were designed to be heated by internal filaments. However, due to high radiative heat loss, the available electrical power was insufficient to achieve and maintain effective bake-out temperatures ($>300\,^{\circ}$C). One of the AE-C collectors developed symptoms of contamination about 6 weeks after launch, while the other remained free of contamination throughout the 5-year mission. Both of the collectors on AE-D and E eventually became contaminated to some degree, and the internal heating could not improve the quality of the $I - V$ curves. Eventually these probes became useful only for measuring N_i, which is not affected by contamination.

The ineffectiveness of collector heating experienced with some of the AE probes led *Brace* [1998] to use an electron bombardment technique instead. The DE-2 mission employed ionospheric electrons to bombard the probe surfaces. The cleaning was achieved by applying +150 V to one of the probes as the spacecraft traversed the denser parts of the ionosphere [*Krehbiel et al.*, 1981]. This method is simpler than internal heating, requires less power, is faster, and has been proven more effective. The probe was cleaned about 6 days into the mission by electron bombardment for a full orbit. No evidence of patchiness or hysteresis was evident in the $I - V$ curves at that time, since the cleaning did not change the quality of the curves. The probe was cleaned again 18 month later just before the end of the mission, with the same result. The $I - V$ curves from the other DE-2 probe, which was not designed to be cleaned, began to show evidence of contamination several weeks after launch, and its effects were evident throughout the remainder of the mission.

These two results led the instrument team to conclude that both probes had become contaminated prior to or during the launch, and that the initial cleaning of the first probe was successful in removing the contamination before exposure to solar EUV and chemically active atoms (O and O^+) could reduce the conductivity of the contaminating layer. From this limited experience we have concluded that electron bombardment should be used early in the mission to clean the probes before they have experienced extended exposure to the space environment.

As illustrated in Figure 4.6, a cleaning procedure of the type used on DE-2 was not required for the Langmuir probes on the Pioneer Venus Orbiter (PVO) mission [*Brace et al.*, 1988]. The figure shows that early in the PVO mission, when the periapsis altitude was low, the photoelectron yield of the Langmuir probe was low. Presumably this was because encounters of the satellite with Venus' thermosphere deposited a surface layer of O_2 on the probe. Later in the mission, when the periapsis altitude was raised and the satellite was exposed continuously to the solar wind, the photoelectron yield increased by a factor of two and stabilized. This improvement in performance is believed due to the cleaning of the surface of the probe by the impact of solar wind ions. (Exposure to solar UV may also contribute to surface cleaning.) One might expect similar ion and electron sputtering to

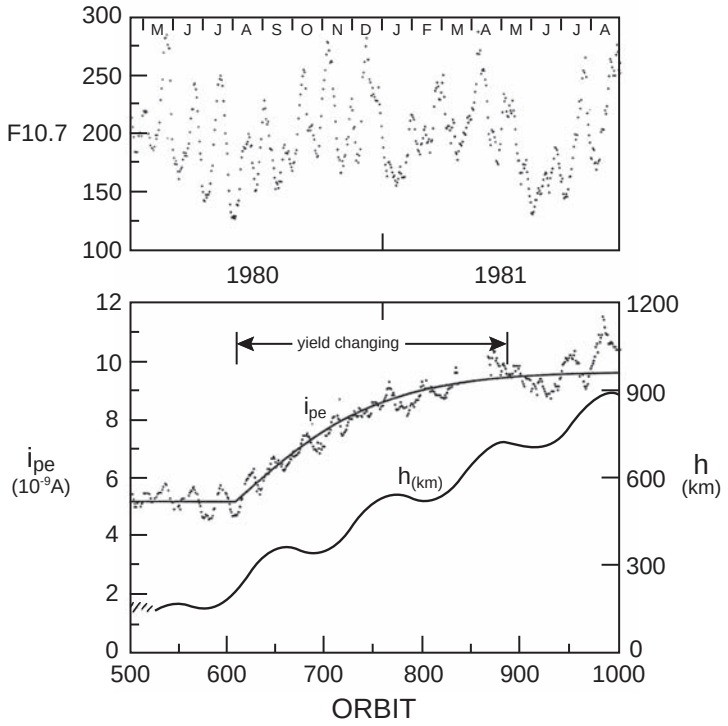

Figure 4.6: The photoelectron yield from the Langmuir probe on the PVO spacecraft, together with the periapsis altitude of the spacecraft, are plotted as a function of time during the mission. The improvement in photoelectron yield is well correlated with the rise in periapsis altitude and is thought due to reduced exposure to atmospheric oxygen that forms a poor photoemission layer on the probe surface. The solar F10.7 flux data are used to correct the photoelectron yield for changing solar ultraviolet fluxes. From *Brace et al.* [1988].

occur in high inclination Earth orbits that encounter energetic ions and electrons at high latitudes. This kind of natural in-flight cleaning could account for the absence of Langmuir probe contamination in the early missions that did not dip into the atmosphere and were in high inclination orbits (Explorers 17, 22, 31, 32, Alouette-2, ISIS-1, and ISIS-2.)

4.2.8.2 Voltage-Measuring Probes

Langmuir probes operated in voltage mode and used to infer plasma density based on spacecraft potential experience two primary changes with time: 1) the leakage current of the probe's preamplifier will increase with radiation damage and 2) photoemission currents from the probe and spacecraft generally increase during the first 2–4 months on orbit. Leakage current changes depend upon the radiation tolerance of the probe preamplifier, the radiation environment, and the amount of shielding. Leakage current problems with the FAST probes resulted in noticeable instrument degradation after ∼3 years, with severe degradation after ∼5 years. This was quite good for a mission in a high-radiation

environment, and designed for a one-year nominal life. In contrast, the Polar spacecraft's Langmuir probes continue to perform well after 8 years in a similar radiation environment, with no signs of leakage current problems.

The increases in photoemission currents result from an evaporation of surface contaminants and generally requires an increase in the bias current applied to the probes to maintain a constant probe-to-plasma potential. The increased photoemission of the spacecraft means that the plasma density versus spacecraft potential relationship will change as surface contaminants are removed. A related change in photoemission properties can occur if the spacecraft orbit takes it close to a planet, in particular less than ∼600 km for the Earth. In this case probe and spacecraft surfaces can absorb enough oxygen to change the photoemission properties. On-board thrusters can also contaminate surfaces and change the photoemission properties.

In addition to these overall changes, there are several periodic variations in photoemission that affect the inferred plasma density. Since spacecraft are generally asymmetric about their spin axis, the amount of surface area exposed to sunlight will change as the spacecraft rotates, causing small changes in spacecraft potential. Often the largest variations come from the Langmuir probes' deployment wires, whose outer conducting jacket is typically tied to spacecraft ground. For Cluster, spacecraft potential modulations of ∼0.4 V and ∼1.5 V were observed superimposed on average spacecraft potentials of ∼5 V and ∼30 V, resulting in inferred plasma density variations of ∼12 % and ∼20 %, respectively.

Since the inferred plasma density is obtained from a difference measurement between the spacecraft and a Langmuir probe, variations in probe-to-plasma potential will affect that result. Small variations in probe-to-plasma potential caused by plasma density changes or by spacecraft produced electric fields, which scale with plasma density, will not introduce errors since these variations are included in the in-flight cross-calibration between plasma density and spacecraft-to-probe potential. However, the probe-to-plasma potential can change with spin due to variations in the probe's photoemission or due to geophysical electric fields. To reduce Langmuir probe emission variations, probes are normally spherical, coated with a graphite paint (Dag 213, Acheson Colloids) to provide uniform photoemission, and carefully handled to prevent any non-uniform contamination. However, should a non-uniform surface be present, as might occur from a fingerprint, then a spin period modulation of the probe-to-plasma potential may be observed. These contamination problems often clean up as the probe is exposed to sunlight and/or intense particle bombardment from the plasma. The Cluster mission uses spherical probes that are attached by a fine wire. The exposed area of the wire is ∼10 % of the probe's surface area, resulting in small variations in photoemission with spin. Spin-frequency probe-potential variations induced by contamination or varying solar illumination on the fine wire are smaller than the spacecraft potential variations with spin. Probe operation is also influenced by solar illumination and therefore brief entry into the spacecraft shadow will result in a brief spike in potential at the spin period. Shadow problems can generally be avoided by tipping the spacecraft spin axis away from the normal to the Earth-Sun line. In addition, any geophysical electric fields will create modulations of the probe-to-spacecraft potential. The use of two (or four) probes located on opposite sides of the spacecraft will eliminate these electric-field-induced problems unless the scale size of the fields is small compared to the probe antenna lengths.

Since plasma densities inferred from the spacecraft potential are made for low density regimes, it is generally assumed that the plasma current to the probes is small and has

little impact on the probe-to-plasma potential, which is mainly controlled by the probe's bias current. However, when plasma densities are greater than a few particles per cm^3, or when intense electron fluxes are present such as in aurora, the plasma currents can become significant. In this case a change of the plasma current as a probe goes into the spacecraft wake or onto the same magnetic field line as the spacecraft, can briefly change the probe's floating potential. In these higher density regimes, the inferred plasma density is a stronger function of relative potential between the probe and spacecraft, so that small variations in probe-to-plasma potential may significantly affect the inferred density. In addition, intense fluxes of energetic electrons, as observed in the aurora or at times in the magnetosheath, may cause a deviation from the nominal spacecraft potential versus local plasma density curve, even if electron thermal corrections are included. When the spacecraft potential is small, these energetic electrons will also produce secondary electrons that will complicate the inferred density versus potential relation.

4.2.9 Unexpected Sources of Noise

Often an instrument will encounter unexpected sources of noise, background, or spurious sensor responses. Unless on-board diagnostics are capable of identifying and eliminating these effects that can obscure the intended measurements, data analysis efforts can be greatly complicated. This section presents several examples of unexpected noise that illustrate real problems encountered in flight. The purpose is both to provide a forum where these problems can be recorded for future reference and to suggest design modifications and laboratory testing that allow identification of similar problems before they are discovered again during the next missions.

Both CEMs and MCP exhibit several forms of background noise or spurious counts that instrument designers should be aware of. For example, MCPs produce background counts from radioactive decay in the glass, edge effects, and through a process called "after-emission". Radioactive decay will contribute a background rate of $\sim$0.2–1.0 count s^{-1} cm^{-2} of MCP area. The edges of MCPs are always a source of noise and care should be taken to design the MCP mounting so that collection anodes do not collect charge from within 2 mm of the MCP edge.

Penetrating radiation, in particular MeV electrons, from the radiation belts and energetic solar particles are the most obvious source of unwanted background. Penetrating radiation can affect all types of detector systems from low-energy plasma instruments to solid-state detector instruments. Other than increasing the thickness of material around the detector, which is normally precluded by limited mass resources, little can be done to prevent this background. If mass is available, the use of graded-Z material is preferred [*Robertson*, 2003]. Graded-Z material not only reduces the flux of penetrating MeV electrons, but also reduces the bremsstrahlung X-rays produced in the shielding that can also trigger the detector. An alternate technique employs a guard scintillator surrounding the detector and coincidence rejection to eliminate background response from penetrating radiation. Such a system was developed for the Wind 3D Plasma sensors [*Lin et al.*, 1995]. For Wind 3D Plasma this background removal allowed better measurements of the tenuous flux in the solar wind suprathermal tail [*Lin et al.*, 1998]. A drawback of coincidence detection is a reduction of the capability to handle high counting rates. For instruments that will experience both low and high background rates, the ability to disable the coincidence feature is preferred.

Background count rates in the MCP detectors from penetrating radiation (or radioactive decay in the glass) will produce an exponential PHD since the pulses are initiated throughout the device and not at the entrance aperture. Because the exponential distribution is more sensitive to MCP voltage changes near the pre-amplifier threshold, variation in MCP bias voltage can affect the background rates more than they affect the efficiency for counting particles. Therefore it is better to keep the MCP bias voltage at a lower level. For a Gaussian PHD, a reasonable value for the peak of the PHD is about five times the preamplifier threshold, where the preamplifier threshold is set high enough to avoid any electronic noise. The primary sources of penetrating radiation seen in the FAST sensors are from the inner and outer radiation belts, and from energetic solar protons associated with large flares. FAST does not collect data inside the inner belt due to high background (>40 kHz). Background rates of 1–10 kHz are observed in the outer MeV electron belt. Solar proton events can produce high background rates. The solar proton event of November, 2000 had a maximum of >30 kHz background count rate in the FAST instrument and noticeable background lasted several days. These sources of background responses appear as slowly varying, analyzer-energy-independent low-level count rates.

The "after-emission" phenomenon in an MCP is when a microchannel continues to produce output pulses after the original stimulus has been removed [*Lees et al.*, 1990]. After the stimulus is removed, the probability of such after-emission is observed to decrease with a power law time constant, t^{-m}, where m may range from 0.5–1.0 depending upon the stimulus. The elevated noise levels may last for hours. The source of this noise is not understood but its similarity to the increase in background counts seen at operating pressures in the 10^{-4} to 10^{-5} mbar range suggest that it may result from an increase in pressure at the back of the MCPs due to vaporization of surface contaminates by the charge pulses. This type of noise is particularly noticeable when an incident flux varies from a large value to near zero in a short interval. For example, solar wind ion instruments, which measure a large flux over a small portion of a spacecraft spin, may observe after-emission for the remainder of the spin.

After-emission from CEM's, similar to the MCP artifact discussed above, has been observed in the TED instruments on NOAA-10 and NOAA-14. This curious phenomenon was initiated when the satellite encountered intense auroral particle fluxes that produced large count rate responses in the TED particle sensors. The elevated CEM responses continued after exiting the region of auroral particle fluxes, both in data taken during the ESA energy sweep and during the short period at the beginning of each sweep when the analyzer plate voltage was forced to zero so that a background CEM response could be obtained. Figure 4.7 illustrates this effect as it appeared simultaneously in two CEM systems on NOAA-14. The counts from the two CEMs accumulated in 16 consecutive background intervals (1.23 seconds every 32 seconds) are shown for an entire transit over the auroral zone. The shaded area indicates where intense natural aurora was encountered. The CEM background unexpectedly increased during those encounters and required some minutes to decay to normal levels after the auroral stimulus had been removed.

The explanation for the long-lived spurious count phenomenon on NOAA-14 remains unknown. The problem did not appear until after about six months of on orbit operation. It was suspected at the time that the problem arose from the Malter effect [*Malter*, 1936], the field emission of electrons from an exposed aluminum oxide surface that had charged under the impact of auroral particles entering the ESA. The six-month time constant was explained as being the time required to erode away a protective black coating, perhaps by

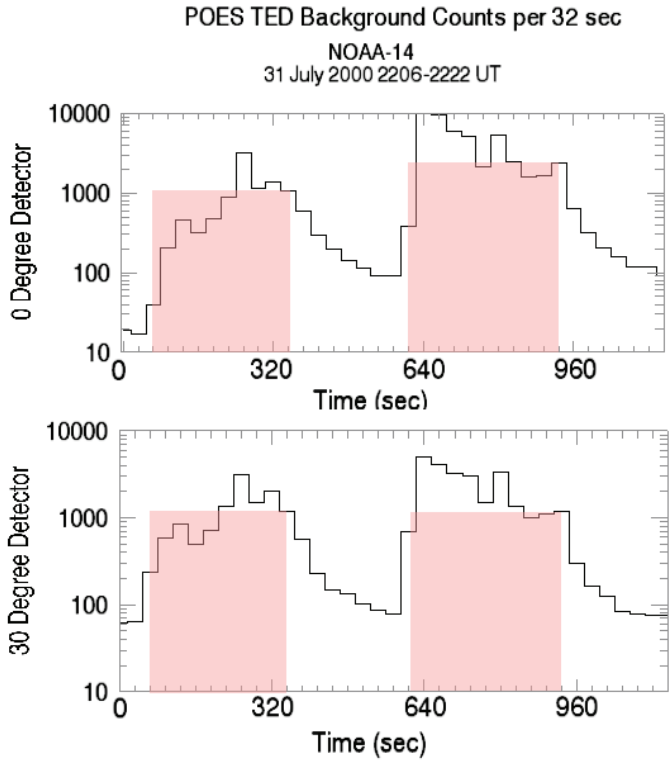

Figure 4.7: Background counts from two NOAA-14 TED electron analyzers, with Channeltron detectors, as a function of time. Background counts were accumulated over 1.23 seconds of a 32 second period containing 16 consecutive analyzer energy sweeps. Background counts were registered during a portion of the energy sweep when zero bias voltage was applied to the analyzer plates. The shaded areas mark periods when large auroral electron fluxes were measured and which correlate with large increases in background counts. After exiting these intense aurora, the background counts decay away with a time constant the order of one minute.

atomic oxygen impact. However, late in the NOAA-14 mission, the signal threshold discriminator level was increased in order to eliminate an electrical noise source from being counted. Astonishingly, this step virtually eliminated the after-emission phenomenon and demonstrated that the source of the CEM response must originate from within the CEM itself rather than from electrons field emitted from an exterior surface. The CEM design used in the NOAA-14 instrument was a two-stage device with a separately biased "pre-amplifier" stage feeding charge pulses into a "post-amplifier" stage. The two sections of the CEM were joined using a conducting epoxy (of unknown manufacture, but perhaps aluminum based) that served also as the electrical contact for the bias voltage. One explanation of the NOAA-14 CEM after-emission phenomenon could be a Malter effect field emission process from the epoxy. CEM pulses originating from that location would not have undergone the full gain of the device and, so, would have amplitudes that would fall below the increased threshold level.

The Wind 3D Plasma PESA-H ion sensor experienced unexpected MCP noise counts in look directions near the ecliptic plane where no counts above background were expected. The noise counts were modulated at twice the ESA energy sweep rate, producing a two-humped spectrum with a factor of four count rate modulation. The noise counts scaled with solar wind flux and were confined to those anodes that were exposed to the intense solar wind protons when the sensor faced sunward.

The PESA-H sensor was not designed to measure the intense solar wind protons, but rather the supra-thermal tail of the ion distribution. PESA-H was expected to saturate when facing the Sun, and to recover quickly to make the off-sunward measurement. Although this noise is not completely understood, it appears to be related to "after-emission" [*Lees et al.*, 1990] in the MCPs after being exposed to high solar wind ion fluxes. To reduce these background counts, the PESA-H sweep was modified to perform only a partial sweep when facing the Sun, avoiding the solar wind protons. This eliminated the problem and allowed more accurate measurements of the solar wind's suprathermal tail.

The modulation at twice the PESA-H energy sweep rate is most puzzling. This modulation is at the same sweep rate as an adjacent PESA-L sensor, however arbitrary phase shifts are observed in this modulation that appear unrelated to any identifiable instrument operations. One possibility is that the MCP pulse height distribution (PHD) of the "after-emission" signals is near the fixed discriminator thresholds ($\sim 2 \times 10^5$ electrons) of the PESA-H preamplifiers. In this case a few percent modulation of the MCP high voltage could produce a significant change in counts above threshold. No evidence of such high voltage modulation was recorded during the ground testing, and no test data exists on the "after-emission" PHDs in the PESA-H MCPs since this phenomenon was not recognized as a potential problem until after the sensor was on orbit. This explanation requires a PHD near the discriminator threshold, which differs from that described in *Lees et al.* [1990], so the nature of this noise problem is still a mystery.

Although the PESA-H noise problem is still not understood, its observation suggests several tests and design modifications. Raw HV supplies for MCPs should be tested and shown to have a voltage ripple of $<1\,\%$, otherwise noise near the discriminator threshold may be modulated, making its removal difficult. Sensors should be designed with adjustable threshold discriminator levels since new forms of noise may manifest themselves on orbit. For sensors exposed to high fluxes, ground tests of after-emission should be performed to characterize it, including determination of its PHD. Finally, designing in the ability to eliminate exposure to high fluxes would allow sensors to provide more accurate measurements of weak fluxes.

4.3 Identification of Instrument Degradation, Noise, and Spurious Responses

This section details the in-flight calibration procedures and techniques that are used to identify instrument and particle sensor degradation. A major sub-section concentrates upon the identification of gain degradation in electron multipliers that are the sensor of choice in space plasma instruments. Numerous examples of gain loss in these devices, as exposed by various types of in-flight calibration procedures, are provided as well as examples of gain restoration by increasing sensor bias voltage. Separate sub-sections are devoted to identifying and quantifying degradation and noise in time-of-flight, solid-state,

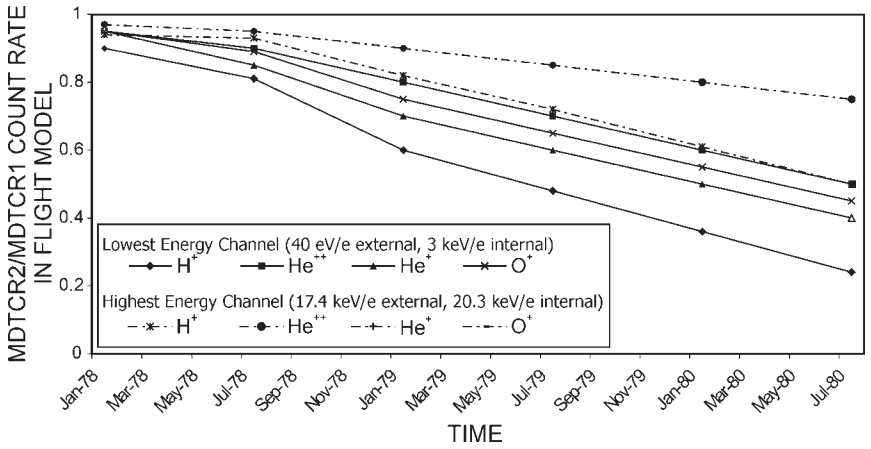

Figure 4.8: Ratio of the count rate at high discrimination level (MDTCR2) and the count rate at low discrimination level (MDTCR1) on the ISEE-1 Ion Mass Spectrometer over the course of approximately 2.5 years. The degradation is species dependent and energy dependent. Note that the high-energy He^+ and He^{2+} data points are superimposed on the high-energy O^+ curve.

and neutral gas instruments. Additional sub-sections are used to demonstrate the long-term stability of Faraday cups and to identify degradation in Langmuir probes. The last section describes use of artificial signal injection to test for degradation.

4.3.1 Identifying Gain Degradation in Electron Multiplier Detectors

Early examples of instrument degradation due to gain loss in electron multipliers can be found in missions prior to ∼1980 that often incorporated fixed high voltage supplies. Electron multiplier gain degradation was anticipated in the design of the ISEE-1 Ion Mass Spectrometer [*Shelley et al.*, 1978]. To maximize the geometric factor, this instrument used the Johnston electron multiplier [*Stickel et al.*, 1980; *Peart and Harrison*, 1981] with a fixed high voltage supply. The signal processing employed two discrimination levels, differing by about a factor of 2.0, for recording counts. By monitoring the ratio between the high discrimination and low discrimination level count rates, an estimate of gain degradation in the multiplier could be obtained and corrections made. As seen in Figure 4.8, the high discrimination level rate declined significantly with respect to the low level, and after about 2.5 years only the low discrimination level count rate could be used. Further degradation, as sensed by the low discrimination level rate, was not detected during the instrument's remaining two years of life. As can be seen in Figure 4.8, the gain degradation was species and energy dependent. This is consistent with known efficiency and gain variations for ion detection by electron multipliers [*Keller and Cooper*, 1996; *Oberheide et al.*, 1997] since higher-mass and higher-energy ions tend to eject more secondary electrons resulting in larger gain.

A significant gain loss was experienced by the CEMs in the electron and proton ESA spectrometers on the SCATHA satellite [*Fennell*, 1982]. The CEM bias supply in this instrument could be commanded to one of three voltage levels. In normal operation the bias voltage was kept at the lowest level. However, periodically, at locations in the

magnetosphere where particle fluxes were expected to be constant, the CEM bias voltage was increased for a short time to each of the two higher levels. During those tests the ratio of sensor count rate at the lowest bias to that at each of the two higher levels was determined, as well as the ratio of sensor count rate at the mid-point bias level to that at the highest. Figure 4.9 shows the evolution with time during the mission of these three ratios for the electron ESA and proton ESA CEM, respectively. All three count rate ratios were initially close to 1.0 indicating that the CEM gains were sufficiently high even at the lowest bias voltage. With time each of these ratios declined, the most serious decline being in the ratios that compared the CEM response at the lowest bias and highest bias levels. Functional fits were made to these experimental data and used to correct the SCATHA observations for CEM gain degradation.

Later instruments generally incorporated detector bias supplies whose voltages could be increased with time to restore electron multiplier gain. In addition, the more recent instruments are able to cycle the signal electronic discrimination through multiple levels to obtain information on the detector's pulse height distribution and the degree of multiplier gain loss. The Total Energy Detector (TED) in the Space Environment Monitor on the POES satellites uses such a system to track the gain loss in the CEM particle detectors. Figure 4.10 shows an example of this procedure and the effect of raising the CEM bias voltage to restore the electron gain. The CEM response is plotted as the threshold discriminator cycled through four steps, the level at each step increasing by a factor of 2.0 over the previous step. The top panel in Figure 4.10 shows significant decrease in sensor response with increasing discriminator level, indicating insufficient CEM gain. The bottom panel shows the results after the bias voltage had been increased. The variation in sensor response with discriminator setting is much decreased and is largely dominated by temporal variations in the natural auroral electron flux at the time. It should be noted that in routine operation, the threshold discriminator is always set to its lowest level.

Data from the SSJ4 precipitating particle spectrometers of the Defense Meteorological Satellite Program (DMSP) are provided by the Air Force Research Laboratory and are widely used. The calibrations are done as carefully as possible in a vacuum chamber before flight, however the laboratory calibration data do not account for the on-orbit degradation of the Channeltron detectors. Comparisons of in-flight auroral particle data from newly launched spacecraft with data from similar instruments on older spacecraft in the same orbit plane have been problematic because two spacecraft almost never cross the auroral zones simultaneously.

In a promising new technique, the flux of MeV particles in the South Atlantic Anomaly (SAA) region has been used as a standard for determining the degradation of the detectors. The SSJ4 instruments were not built with the intention of detecting and measuring MeV particles. However the MeV particles are capable of penetrating the sides of the instrument case and reaching the Channeltron detectors. The SAA is a source of particles that exhibits almost no variation in flux from day to day and month to month, but does vary with respect to the 11-year solar cycle. While the pulse height distribution (PHD) of a CEM from penetrating particles is not optimum, if carefully used the SAA particles can be used as a standard because the flux is a much steadier source of particles than any other location available.

Ten SSJ4 instruments have been flown on DMSP spacecraft, from DMSP/F6 (launched December 1982) to DMSP/F15 (launched December 1999). Each instrument includes a pair of electrostatic analyzers (ESAs) for electrons and a pair for ions. The high-energy

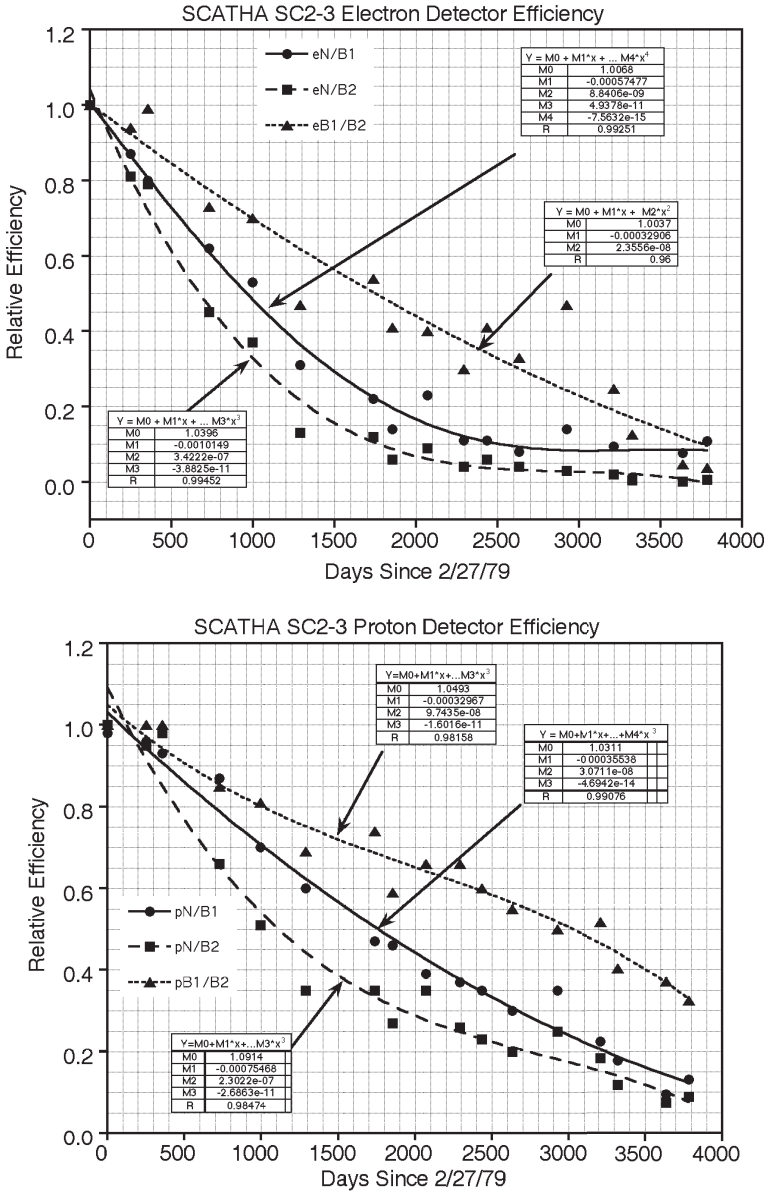

Figure 4.9: The figure illustrates the decrease in CEM detector efficiency in the electron (top) and proton (bottom) ESA spectrometers on the SCATHA satellite. The parameter eN/B1 in the top part is the ratio in electron ESA CEM response between the lowest bias setting and the mid-point bias setting. eN/B2 is the response ratio between the lowest bias setting and the highest. eB1/B2 is the ratio between the mid-point and highest bias setting. The parameters in the bottom part that characterize the CEM in the proton ESA have a similar meaning.

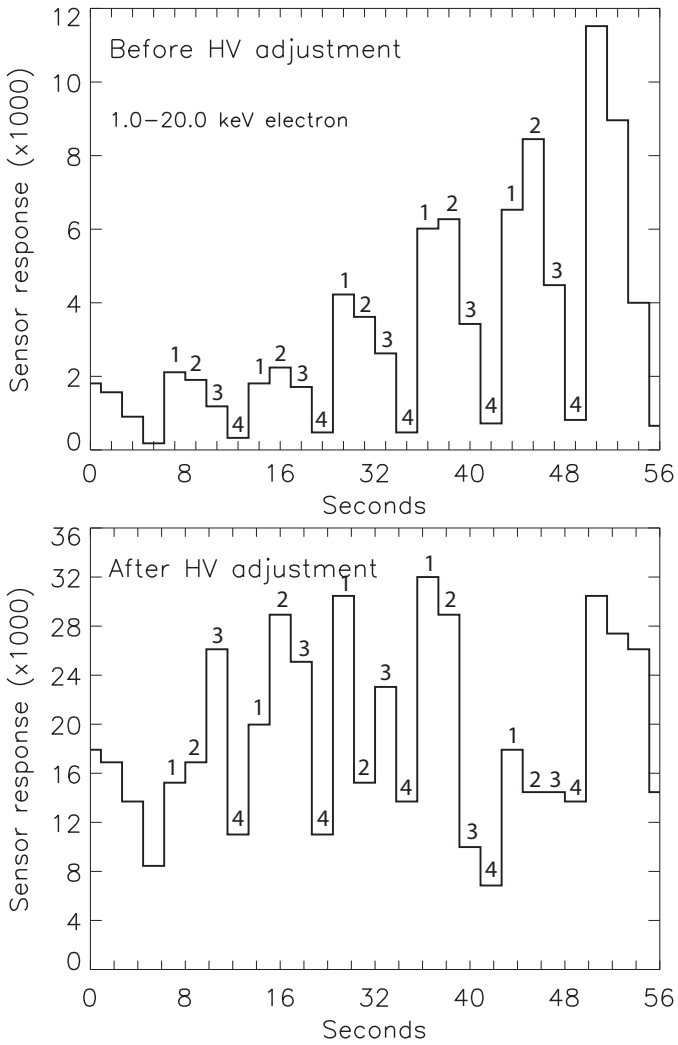

Figure 4.10: The top panel displays the integrated energy flux response of one of the 1.0–20 keV TED electron sensors on NOAA-16 as a function of time. 56-seconds of data are shown. Each discriminator level is held constant for 2-seconds and adjusted through four settings as labeled on the figure. Level 4 is the highest discriminator setting. The dramatic decrease in response at levels 3 and 4 (the highest level in each sequence) indicates insufficient CEM gain. The lower panel displays that sensor's response after the CEM high voltage was adjusted upwards, illustrating a much less systematic decrease in counts with increased threshold indicating sufficient CEM gain.

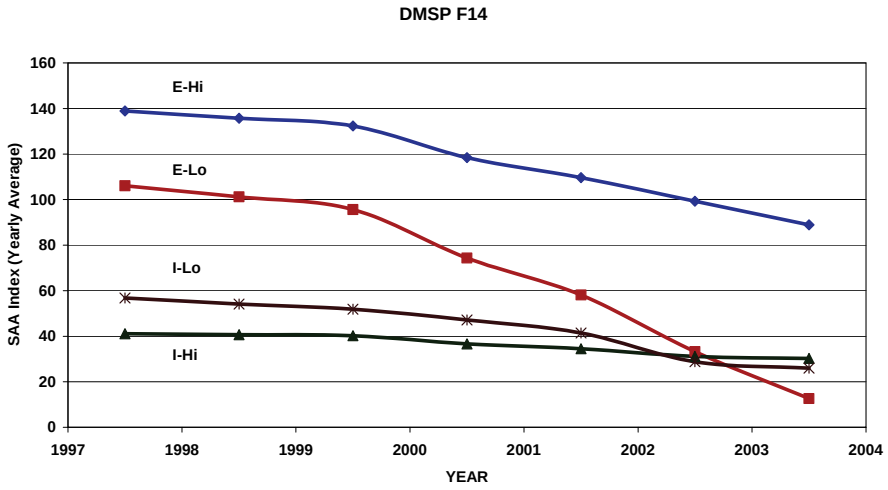

Figure 4.11: Time variation of SAA index for the four detectors in the SSJ4 instrument on DMSP F14, without normalization.

ESA in each pair has 10 energy channels ranging from 30 keV (channel 1) to 950 eV (channel 10). The low-energy ESA in each pair has 10 energy channels ranging from 950 eV (channel 11) to 30 eV (channel 20). A Channeltron detector is used in conjunction with each ESA. Two resulting 20-point spectra are generated each second (one each for electrons and ions).

To determine the SAA index, the daily average of count rates in four energy channels is summed (channels 2, 4, 6, 8 for high-energy ESA; channels 12, 14, 16, 18 for low-energy ESA) while the instrument is traveling through the SAA region. The instrument goes through the SAA 7 to 8 times per day. The SSJ4 sensor experiences spurious responses at SAA locations during some seasons of the year. In order to minimize the effect of the spurious response in the SAA index, yearly averages are used. Figure 4.11 shows the time variation of the SAA index for the SSJ4 instrument on DMSP F14. The plot includes curves from the high- and low-energy electron ESAs (E-Hi and E-Lo), and the high and low-energy ion ESAs (I-Hi and I-Lo). The high-energy ion data are more stable over time than the low-energy ion data or the electron data. This is observed for all of the SSJ4 instruments. Figure 4.12 is a composite SAA index for the F8, F9, F13, F14, and F15 SSJ4 high-energy ion ESAs. The dependence of the SAA on the solar cycle is clear from this figure. Based on Figure 4.12, the low-energy ion data and the electron data in Figure 4.11 are normalized by the high-energy ion curves for all SSJ4s to remove the solar cycle variation. The normalized SAA index then reflects the time deterioration of the CEMs.

The INMS neutral gas instrument for the Cassini mission uses a similar, but more sophisticated method for tracking and compensating gain degradation in the CEM detectors that are used. The pulse height discriminator can be cycled through sixteen different levels while the detector bias voltage is cycled through three settings. Figure 4.13 shows the integrated pulse height data for the three different bias voltage levels chosen for the

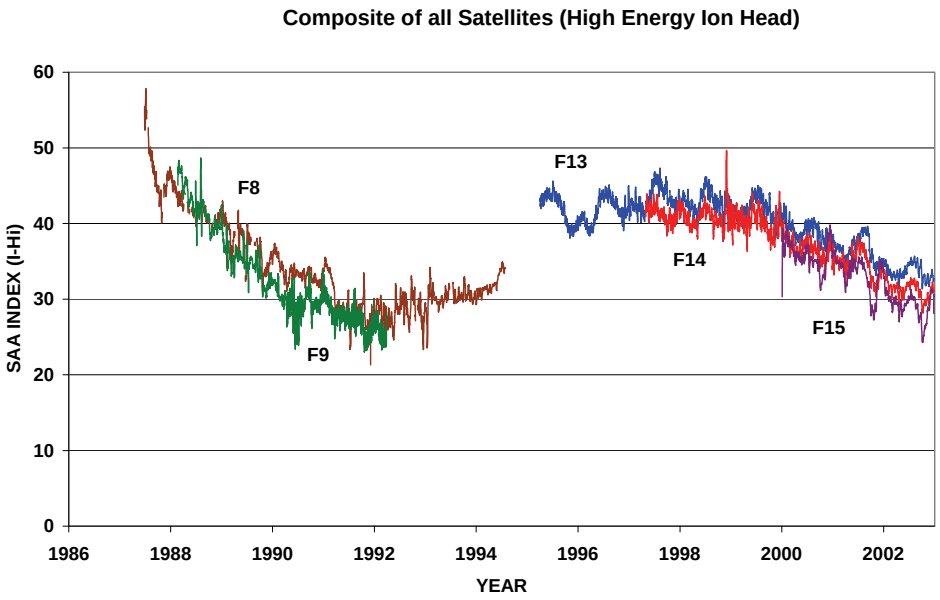

Figure 4.12: Solar cycle variation of composite SAA index for high-energy ion ESAs.

INMS flight configuration at five different times during the instrument's life history. It can be seen that as time progresses, the slope of the curves above discriminator level 4 changes the greatest for a bias voltage of 2500 V and the least for 2900 V. An estimate of the effect of multiplier gain change on a change in absolute sensor sensitivity indicates that a 20 % change in sensitivity will occur for a multiplier gain change from 2×10^7 to 1×10^8 [*Waite et al.*, 2004].

Estimates of the efficiency or electron gain loss in the Wind 3D Plasma Experiment were obtained by inter-comparing solar wind densities inferred from the ion and electron ESAs with the Wind SWE detector. When efficiency or gain loss was detected, the MCP bias voltage was increased to compensate. MCP voltage adjustments were also commanded for short periods to look for changes in calculated density at the MCP voltage change boundaries. However these methods were not very reliable for exposing MCP gain loss since small variations due to the efficiency changes were often masked by larger variations in the actual solar wind density.

Using a method similar to that employed in the INMS instrument, the MCP efficiency decreases in the FAST ESAs are detected by adjusting the preamplifier discriminator threshold at several MCP bias voltages near the currently programmed value. This procedure involves toggling the discriminator threshold between its normal operating level just above the system noise and a test level near the peak in an optimal MCP PHD. The MCP bias voltage is adjusted until the MCP count rate varies by a factor of two as the discriminator level varies. For a nominal Gaussian PHD from the MCP, this procedure insures that the bias voltage is sufficient that virtually all the MCP pulses will be registered.

The PEACE (Plasma Electron And Current Experiment) instruments on the Cluster mission employed MCPs and ESAs to obtain 3-D distributions of electrons. Post-launch

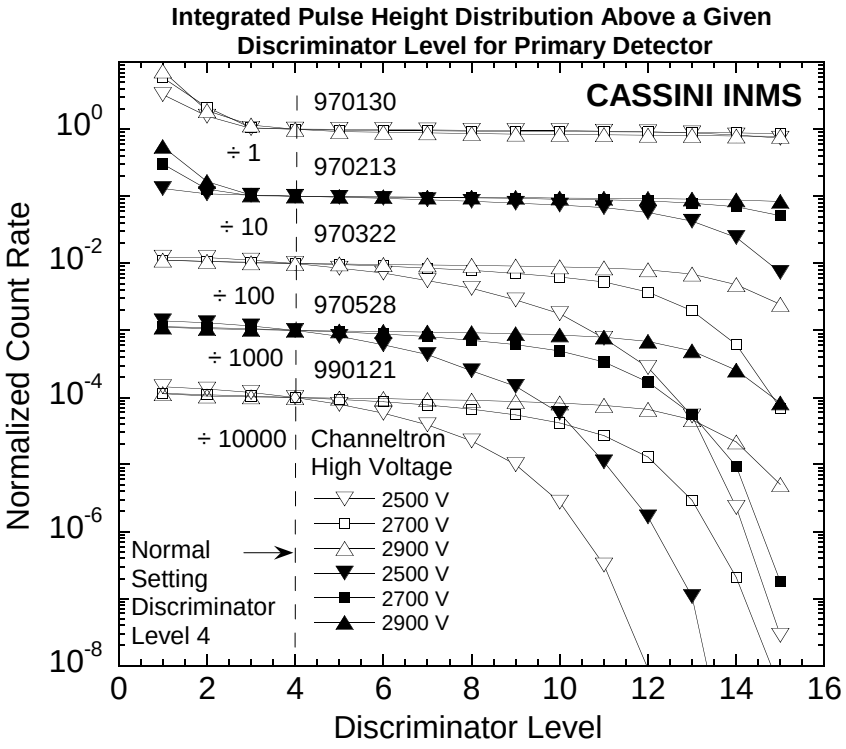

Figure 4.13: Plot of the integrated pulse height distributions for the 3 high voltage levels (Low, Medium, High) used for the Cassini INMS flight unit. The data are for 5 different dates: 970130 (beginning of the CEM laboratory characterization period), 970213 (end of characterization period), 970322 (after environmental testing), 970528 (spacecraft level test) and 990121 (instrument check-out after launch.) Level 4 is the normal level used. Data for 970130 and 970213 used mass 28 from N_2, while 970322, 970528, and 990121 used mass 40 from Ar. For ease of display, the curves have been normalized to discriminator level 4 and the 3 sets of data for each date have been divided by the values shown just below the curves on the left-hand side of the dashed line. The date 970130 is interpreted as year 1900+97=1997, month 01 (January) and day of month 30. From *Waite et al.* [2004].

procedures established for PEACE included gain monitoring of each sensor, comparison between the two sensors on the same spacecraft, comparison with sensors on the other spacecraft and finally, comparing with other instruments such as WHISPER. PEACE did not include the ability to determine MCP pulse height distributions after launch using variable pulse threshold levels in the signal electronics although it did have the capability to vary the individual MCP bias voltages.

Advantage was taken of the fact that the PEACE instrument contained two analyzers (HEEA and LEEA) that had overlap in the measured electron energy range and differed only in geometric factor. The procedure for tracking MCP performance involved commanding the LEEA and HEEA to perform energy sweeps over the same electron energy range so that their expected responses would differ only by the ratio of geometric factors.

The MCP bias voltage in one of the analyzers (either the LEEA or HEEA) would be held constant at its normal operating value while the bias voltage for the MCP in the other analyzer was stepped through a wide range below and above its normal operating value. The response of the one MCP as a function of changing bias voltage compared to the MCP whose voltage was fixed provided information about the adequacy of that MCP gain relative to the fixed discrimination level. The procedure was repeated but the role of the two analyzers reversed to provide information about the gain of the second MCP. In this manner gain degradation was monitored and MCP bias voltages increased as needed.

A few space instruments have integrated a UV lamp with CEM detectors to provide a standard stimulus to electron multipliers that could be periodically commanded on from the ground and thereby track detector gain over time. This approach was first used in the Plasma Experiment on the Helios-1 and -2 missions [*Schwenn et al.*, 1975; *Rosenbauer et al.*, 1981]. Because the pulse discriminator threshold in the Helios instruments was maintained well below the amplitude of the charge pulse from the CEM (insuring all output pulses were counted), a simultaneous measurement of the CEM count rate from the UV lamp and the integrated current output from the CEM would immediately yield an average charge per pulse (the CEM gain). Early in the mission the gain decreased due to scrubbing but was restored with a single increase in bias voltage and remained very stable for remaining five years of this mission.

A second, more elaborate, implementation of a UV calibration lamp system was used in the SWE Vector Electron Ion Spectrometer (VEIS) on Wind [*Ogilvie et al.*, 1995] and again in the Hydra experiment on board Polar [*Scudder et al.*, 1995]. In the Hydra instrument individual light pipes coupled the output from a single UV lamp to 12 separate sensor heads thus providing a common stimulus for all the electron multiplier detectors. In principle this approach would not only track degradation of individual detectors but would permit adjusting individual detector bias voltages so that all sensors had the same sensitivity. After the launch of Polar use of this system was deferred until it had been verified that all the electron multipliers were operating in a saturated mode. Unfortunately during this period of time radiation damage to the light pipes reduced the UV transmission by different, and unknown, factors so that the intended function of calibration of separate sensors from a common, well-defined source, was compromised (Scudder, private communication).

A useful report on the design and use of UV lamps for in-flight calibration of a variety of sensors used in space experiments is provided by *Morrow et al.* [1993].

4.3.2 Identifying Degradation in Time-of-Flight Detector Systems

The CODIF time-of-flight instruments on the Cluster satellites require routine monitoring of the MCPs that are used to generate start signals, stop signals and MCP position information. In order to be counted as a valid event, an event needs to have a start signal, a stop signal, and a single position signal. Thus the overall efficiency is a combination of the start efficiency, the stop efficiency, and the probability of getting a single position. The start efficiency depends on the number of electrons emitted from the carbon foil, and the MCP gain of the start detector. The stop efficiency depends on how much scattering occurs in the carbon foil, as well as the MCP gain of the stop detector. The probability of measuring a single position can be effected by the MCP gain, and the amount of cross-talk

between positions. These efficiencies depend on position within the instrument, and on the ion species and energy.

The count rate of individual signals and coincidence signals are used to give an absolute measurement of the efficiencies of the different contributions. For example, the start rate tells exactly how many events triggered the time-of-flight system (but not how many total ions hit the start MCP), independent of the start efficiency. The start-stop coincidence rate tells how many of the ions that gave a start (i.e., triggered the time-of-flight system), also gave a stop. Thus, the ratio between the start rate and the start-stop coincidence rate is an exact measurement of the stop efficiency. Similarly, the ratio of the stop rate to the start-stop coincidence is a measure of the start efficiency (see also Section 3.4.2.4). Thus the rate ratios can be used to track the efficiency changes during the mission. This analysis should be carried out in regions where background is low to minimize spurious start or stop signals.

To use this method, it is important that the rates reliably reflect the signals actually used by the time-of-flight electronics. On Cluster/CODIF, for example, the start rate measures exactly the same signal that is used to start the time-of-flight measurement and the start-stop coincidence rate also comes directly from the time-of-flight circuitry. Thus the ratio of these two rates exactly gives the stop efficiency for the time-of-flight measurement. The stop rate, while generated from the same charge pulse, is processed with different electronics than the stop pulse as it goes into the time-of-flight electronics. Thus the threshold for the stop rate can be different from the threshold for the stop used by the time-of-flight system. If the threshold is different, then the start efficiency determined by taking the ratio of the start-stop coincidence rate to the stop rate is only an approximation to the true start efficiency. Only one of the 3 operating CODIF instruments has a stop rate close enough to the "real" stop threshold to be used for reliable "start" efficiency measurements.

4.3.3 Identifying Noise and Radiation Damage in Solid-State Detectors

The in-flight identification of noise in the electronics of a solid-state detector system is done by introducing pulses of known frequency and with amplitude that increases monotonically with time into the charge sensitive amplifier and pulse discriminator chain. The pulse amplitude range over which each detector's lowest energy threshold discriminator transitions from no response to full response to the injected pulses provides a measure of noise generated by each solid-state detector. This procedure also verifies that the electronic pulse height discriminator levels are proper and correspond to the energy band edges that were set prior to flight. If the solid-state detector noise level becomes large, the ability to identify discriminator levels is much degraded and ultimately becomes impossible. The procedure does not verify the proper operation of the solid-state detector itself, for example, whether all the charge deposited in the detector by a particle was, in fact, collected by the amplifier, because the pulse insertion point is just after the SSD.

The noise levels of individual solid-state detectors can increase over time, occasionally very abruptly. When a solid-state detector noise level increases, the data become degraded, sometimes to the point of no value at all. For this reason, the detector noise levels must be monitored continually. Figure 4.14 shows the 30 keV threshold discriminator level (in terms of keV equivalent energy loss in the solid-state detector) for a MEPED (Medium Energy Proton and Electron Detectors) proton telescope flown on NOAA-12

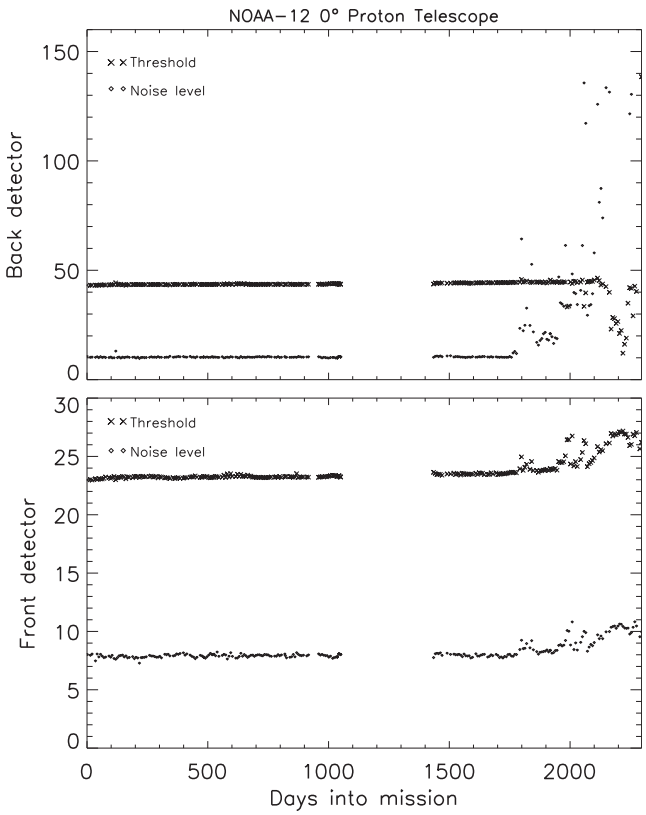

Figure 4.14: A history of the detector noise levels and discriminator threshold levels in terms of keV equivalent energy loss for the front and back solid-state detectors in a NOAA-12 dual detector telescope system. The noise level in the back detector, normally much less than the threshold, increased dramatically after 1800 days of operation and rendered the data from this detector telescope unusable. The gap in the plot was a period when NOAA-12 in-flight calibrations were not exercised.

over the course of many years. Also plotted in Figure 4.14 is the noise level originating from the back solid-state detector in this proton detector telescope, also in units of keV. These data show that after many years of operation, the noise level from this detector suddenly increased in a sporadic fashion. Signals from the back solid-state detector in the two-detector proton telescope assembly are used to "veto" pulses from the front detector in order to provide data on high-energy protons that deposit energy in the front detector but pass entirely through to deposit energy in the back detector as well. When the back detector in this proton telescope became noisy, virtually all the response from the front detector (from low-energy protons stopping in that detector) was vetoed. The instrument count rates ordinarily produced by 30 keV to 2500 keV proton fluxes became very low, and often zero, and that telescope became non-operational.

The first indication that the solid-state detectors in the MEPED proton telescopes on the NOAA satellites suffered radiation damage arose from observations of anomalous

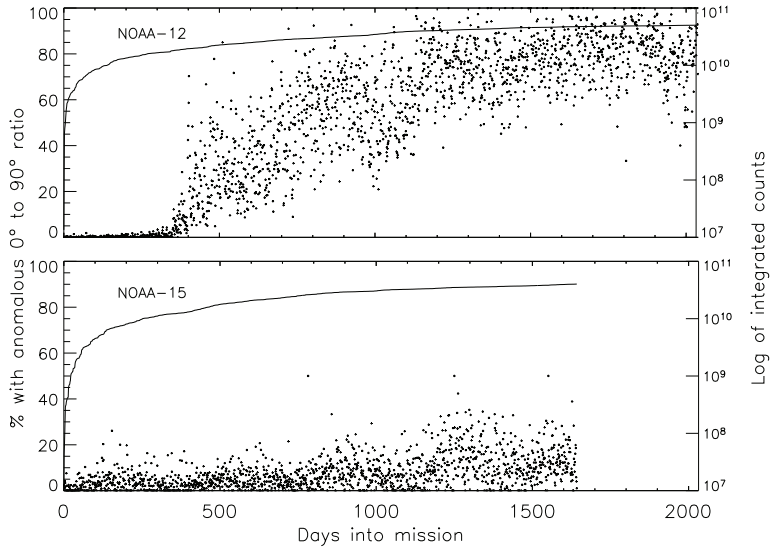

Figure 4.15: The effect of radiation damage to solid-state detectors demonstrated by the probability of anomalous proton pitch angle distributions observed each day during the NOAA-12 mission (top panel) and the NOAA-15 mission (bottom panel.) Also plotted in each panel is the running total of counts accumulated by the 90° proton detector during each mission. It is unclear why the two instruments behaved so differently to this radiation damage. However, the detectors were procured from different lots, stored differently, and launched years apart, so details of the manufacturing, storage, and radiation environment might be required to explain differences in damage caused by regular use.

proton pitch angle distributions. Previous scientific studies of the radiation belt and auroral zone proton populations at low altitude demonstrated that, while the >30 keV proton population may become isotropic (intensities in the atmospheric loss cone comparable with those at high pitch angles) the loss cone fluxes were never significantly higher than the trapped fluxes. Such field-aligned pitch angle distributions are regarded as unphysical and, if observed, might indicate problems with the MEPED proton telescope instruments. MEPED proton telescope observations are routinely surveyed to expose instances of this type of angular distribution. This revealed a subtle, but potentially devastating, solid-state degradation problem.

The analysis of proton angular distributions was restricted to observations in the radiation belts, at L-values between 2.0 and 7.0, and considered only instances where the zenith-viewing detector count rate (averaged over 16-seconds) was greater than 200 counts per second. The number of instances each day that these criteria were satisfied was tabulated, as well as the subset of those instances where the ratio in count rates between the zenith-viewing and horizon-viewing proton telescopes exceeded 1.5 (a field-aligned angular distribution). The upper panel of Figure 4.15 shows the percentage of instances each day that the NOAA-12 MEPED >30 keV proton observations displayed a field-aligned angular distribution, with the linear scale on the left. The running total of counts registered by the horizon-viewing proton telescope is also plotted in the top panel of Figure 4.15, with

the logarithmic scale on the right. The bottom panel of Figure 4.15 shows similar, although less dramatic, behavior on the part of the proton telescope detectors on NOAA-15.

These data make it clear that very significant degradation is occurring in one or both proton telescope detectors. It is certain that this degradation is a consequence of radiation damage to the structure of the solid-state detectors by the impact of low-energy protons stopping in the detector. Damage near the detector surface has reduced the charge mobility to the point that only a fraction of the charge is collected within the integration time of the amplifier (see Section 4.2.4). While detectors in the zenith and horizon-viewing MEPED telescopes must both undergo damage with time, the horizon-viewing detector is more rapidly damaged because the proton fluxes are typically largest at the higher pitch angles. Consequently, the effective threshold proton energy sensed by the horizon-viewing detector increases more rapidly and the integral count rate above that threshold decreases more rapidly than for the zenith-viewing telescope. Eventually, the differences in threshold proton energies between the two are such that the zenith-viewing instrument regularly exhibits a higher count rate than the horizon-viewing telescope.

The precise changes in effective energy thresholds on the part of the MEPED proton telescopes cannot be easily determined. There is no standard proton distribution, with a well defined and time invariant spectrum and intensity available to calibrate the net effects of the radiation damage. Only comparisons of sensor responses between newly launched instruments and ones that have been operating for some time can provide this information.

The first attempt of such a comparison was made between MEPED proton telescope observations on NOAA-15 shortly after the launch of that satellite (when radiation damage to the detectors would have not yet occurred) and the proton observations on NOAA-12 after almost 7 years of operation. While NOAA-15 and NOAA-12 were in essentially the same orbits with almost identical orbital periods, there was roughly one-half an orbit difference in their positions at the same time. The two satellites never sampled the same energetic particle environment at the same time. Thus careful selection of observational data situations, where it was likely that very similar, if not identical, energetic proton populations were sampled, was required so that a comparison between sensor responses could be made. The criteria used to select those cases are described below.

The data selection for both satellites was restricted to locations in the center of the low altitude extent of the outer radiation belt, L-values between 4.0 and 6.0 and in the same hemisphere. Each NOAA-12 transit through the selected location was bracketed in time by a pair NOAA-15 transits, roughly 3000 seconds earlier and 3000 seconds later. Because of the sun-synchronous nature of the satellite orbits, the magnetic local time would be nearly the same for all three data samples. Of the full set of such triads of satellite passes, a reduced database was created by selecting cases where the >30 keV proton telescope responses were significant (more than 1000 cps) at the same L-value location on both the NOAA-15 transits as well as the bracketed NOAA-12 transit. In order to minimize the effect of time variations in the energetic particle population, the criterion was that the proton telescope responses during the bracketing pair of NOAA-15 transits could not differ by more than a small factor. The final database included about 20 cases of favorable comparisons obtained over the course of the first 60 days of NOAA-15 operation.

For each case selected, the NOAA-15 proton telescope responses obtained during the pair of transits were averaged together and used to construct integral proton energy spectra of three functional forms: a power law integral spectrum, an exponential integral spectrum, and an integral spectrum assuming that the differential energy spectrum was Maxwellian.

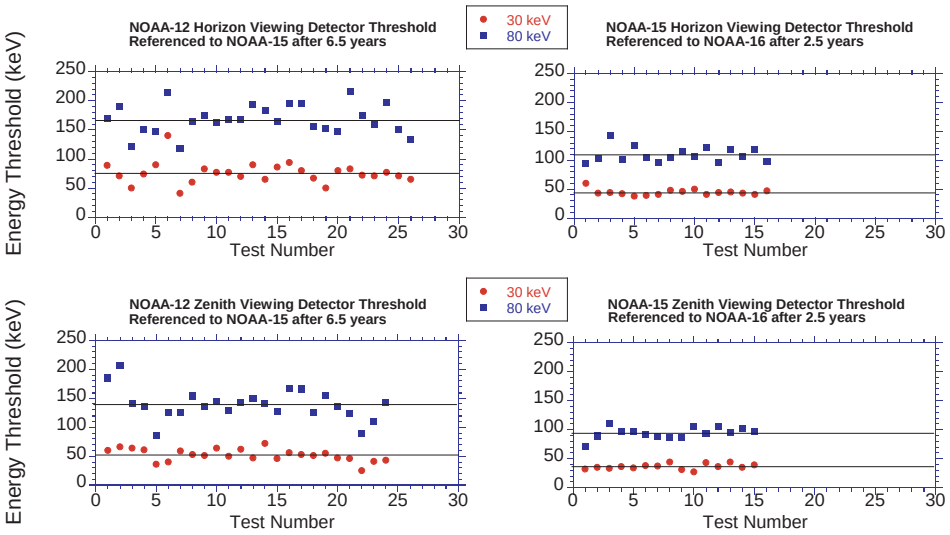

Figure 4.16: Comparisons between the effective proton energy thresholds of newly launched solid-state detector telescopes and telescopes after years of operation. The left pair of panels show the change in the nominal 30 keV and 80 keV energy thresholds in the NOAA-12 instrument after 6.5 years of operation as inferred from comparisons with the newly launched NOAA-15 instrument. The solid-state detector in the zenith-viewing telescope suffered less radiation exposure and less degradation of the threshold. The right pair of panels show the results of a similar comparison between the NOAA-15 instruments after 2.5 years of operation as referenced to the newly launched NOAA-16 instruments.

Because the NOAA-15 detectors were newly launched, it was assumed that no radiation damage had occurred and the proton energy spectra constructed from those data would well represent the proton energy distributions sampled by the NOAA-12 proton telescope systems during the intervening time. The proton integral energy spectra defined from the NOAA-15 observations were then applied to the NOAA-12 proton telescope responses and the proton energy thresholds consistent with those spectra calculated.

The left pair of panels in Figure 4.16 shows the results of about 25 separate energy threshold comparisons between NOAA-12 and NOAA-15 horizon- and zenith-viewing telescope pairs. The nominal energy thresholds at the beginning of life of NOAA-12 would have been 30 keV and 80 keV. While there is considerable variability from case to case, it is clear that radiation damage has at least doubled the effective proton energy thresholds on the NOAA-12 horizon viewing instruments from their original values (30 and 80 keV) to approximately ∼75 and ∼165 keV, respectively. The zenith viewing detectors have also suffered considerable damage (∼50 keV and ∼130 keV thresholds) in spite of their total radiation dose being significantly less.

The right pair of panels in Figure 4.16 show results of a similar comparison done between the NOAA-15 proton telescope instruments after 2.5 years of operation and the NOAA-16 telescopes soon after that satellite was launched. Early in the life of NOAA-16, the orbits of the two satellites crossed one another at nearly the same time when instruments on both satellites observed significant proton fluxes. The NOAA-16 to NOAA-15

comparisons thus were less compromised by possible temporal or spatial variation in the energetic particle population between observations. Over the 2.5 years, the nominal 30 keV and 80 keV energy in the NOAA-15 zenith viewing telescope had increased to about 45 keV and 110 keV while the thresholds in the zenith viewing telescope had increased to only 36 keV and 94 keV, respectively. It is clear that after only 2.5 years of operation, the solid-state detectors in the NOAA-15 proton telescopes were already suffering the effects of radiation damage.

As can be appreciated, whenever the actual proton energy thresholds of proton detector telescopes are uncertain to a factor of 2 or more, estimates of energetic particle fluxes and energy deposition into the atmosphere will be greatly in error. This error could be as much as a factor of 10 or more depending on the steepness of the proton energy spectrum. Therefore the uncertainty in the energy response of solid-state detectors produced by radiation damage is a serious problem.

4.3.4 Identifying Degradation in Neutral Gas Instruments

The primary elements in neutral gas instruments that should suffer in-fight degradation are the CEM or MCP detectors. The method for tracking degradation in those detectors would generally replicate the techniques described in Section 4.3.1. In addition it is known that ion sources experience a loss in efficiency with operation time, especially in the presence of reactive gases. Reactive gases and radicals produced in the ion source change the surface properties of the electrode surfaces, perhaps resulting in insulating layers on electrodes, which can charge up during operation and distort the electric fields. Also, hot wire filaments (e.g. tungsten-rhenium) change their shape with operation time, becoming thinner because of evaporation and chemical attack which may result in a degradation of the ion source efficiency. Other electron emitters, such as cold electron emitters (e.g. micro-tips), also suffer from degradation with time due to the reactive chemical environment and ion bombardment. Identifying and tracking this degradation is usually performed by designing the source to have a constant ionization current of electrons, and by monitoring the voltage required to maintain this current. However, distortion of the filament with age may result in not all of the emitted electrons arriving in the volume where the gas should be ionized. Since the filament current is generally not measured at the place where the ions are created, this degradation may not be easily identifiable and might not be distinguished from a degradation of the detector performance. In addition, electrodes in the ion source may be contaminated from radicals or material entering the source resulting in insolated patches forming on the electrodes which can degrade the collection, trapping, and transfer of the created ions into the mass analyzer. Again this degradation is difficult to separate from degradation of the detectors that register the particles.

As an example of degradation tracking in neutral gas instruments, consider the Double Focusing Mass Spectrometer (DFMS) of the ROSINA instrument that is included in the Rosetta comet mission. The DFMS is unique in that it includes MCPs, CEMs, and a Faraday cup in its detector system. The extreme stability of the Faraday cup detector serves as the standard for identifying and tracking degradation in the far less stable CEM and MCP detectors, as well as degradation of the ion source. Since the operation range of these three detectors is different, cross-calibration between them can only be performed for the limited pressure range of overlap. Linearity of the detectors outside the band of cross-calibration has to be assumed, which is very reasonable since the extrapolation is

towards lower gas pressures. During the ground calibration of the DFMS sensor, several cross-calibrations between the three detectors were performed for CO_2, Ne, and Xe in the pressure range 10^{-8}–10^{-6} mbar using electron emission currents in the ion source between 2 and 200 μA. In all cases each of the two filaments was used. As an example of the intercalibration, for 20 μA emission current and 4×10^{-8} mbar CO_2 one obtains a current of 40 fA in the Faraday cup. The same current gives 22,500 cps in the CEM and 21,900 cps on the MCP detector. In flight, a gas mixture in the pressure range of 10^{-8}–10^{-6} mbar can be released into the ion source from a reservoir to track degradation over the mission duration of ~12 years (see Section 4.6 and *Balsiger et al.* [2007]). In addition, the ROSINA instrument has two total pressure sensors (Bayard-Alpert type) to aid the absolute calibration of the two mass spectrometers [*Balsiger et al.*, 2007].

There are several sources of background whose identification may not be possible until in-flight measurements are made. These can include sputtering of ions from grids by a high speed gas flux, de-absorption of gases from grids or walls, UV light contamination, penetrating background radiation, and backscatter from thrusters. Thruster backscatter will be correlated with thruster firings making identification simple. Hydrazine ($C_2H_8N_2$) thrusters produced a mass 2 peak (H_2) in the INMS on Cassini. Mass independent background generally means that the signal originates in the detector section, after the mass analyzer, and is due to an uncharged particle (photon) or energetic particle not affected by the mass analyzer. Radiation will produce a mass-independent background that can be modulated with detector orientation if the radiation source is not isotropic or the detector shielding not complete. Similarly, UV contamination produces a mass-independent background whose signal should correlate with a UV source such as a planetary atmosphere clouds. (Neutral gas instruments are generally not oriented where direct sunlight has access to the entrance aperture.) A geometry calculation is normally required to determine the linear configuration of the entrance aperture and detector and the projection of the line of sight to the background source. UV light that gains access to surfaces near the detector can release electrons at the multiplier that do not originate in the mass analyzer or ion source section.

Background can also originate in or near the ionization source. The Pioneer Venus Orbiter Neutral Mass Spectrometer (ONMS) detected alkali metal ions that were being sputtered from the grids by an intense CO_2 flux at low altitudes (see also Section 4.2.5). The ions were focused forward into the ion source. This produced an undesirable background signal that raised the threshold for the detection of atmospheric species, in this case ^{40}Ar and ^{20}Ne which were expected or might be expected in the atmosphere of Venus. Identification of these counts as background was made by examination of the angle variation of the signal which did not have the expected cosine dependence for an incoming gas species but displayed a much narrower, forward sputtering angular dependence. In addition, the mass peak width was much wider than usual for the atmospheric gas species due to the higher energy of the sputtered ions and due to the instrument's response to these high energy ions. An additional diagnostic peak indicating sputtering was the mass 23 peak due to sodium, also observed at high pressure in laboratory calibrations.

Desorption of gases from the grids and instrument walls is a final source of background counts in neutral gas experiments. These gases are emitted under electron bombardment in the ion source, or can be emitted directly from the hot filament. Desorption signals are not spin modulated or related to ambient atmospheric flux, and may increase in magnitude over the life of the instrument. These signals are often identified during ground testing as

was the fluorine (F) signal in the Pioneer Venus ONMS instrument. Similarly designed instruments with filament ionization sources also show the characteristic mass 19 peak. Other background gases in the ONMS ion source, after the source was opened prior to entry into the ambient atmosphere, were H_2, CH_4, H_2O, CO, and CO_2 at very low count level. Background contaminant gases can also be renewed each orbit from surface reactions as a result of low altitude exposure to ambient atomic oxygen. Carbon and hydrogen desorbing from various metal parts or the filament along with just normal outgassing are the source. The desorbed gases can also react with each other and other surfaces including the hot filament. The desorption backgrounds are identified by comparing the inbound composition and the outbound composition very far away from the atmosphere. The fact that the same species may show up 24 hours later on an inbound pass, albeit at a lower signal level, confirms that they have been entrained on the metal surfaces and are desorbed by the hot filament thermally or by electron bombardment.

4.3.5 Identifying Degradation and Noise in ENA Instruments

The primary elements in the Energetic Neutral Atom (ENA) instruments that suffer in-flight degradation are the CEM or MCP detectors in medium and low energy ENA instruments, and the SSDs in high energy ENA instruments. The methods for tracking degradation in those detectors would generally replicate the techniques described in Sections 4.3.1 and 4.3.3. For ENA instruments that use time-of-flight (TOF), monitoring changes in the start and stop pulse efficiency can be found in section 4.3.2. The primary degradation experienced by ENA instruments that has not been discussed involves low energy ENA detection. These instruments use kinetic secondary electron emission or surface ionization as part of the detection processes. Kinetic secondary electron emission involves an ENA striking a "start surface" where it releases a secondary electron that produces a "start" pulse. The scattered ENA continues until it is absorbed by the "stop" detector. The time difference is used to determine the particle velocity. Surface ionization is where an electron is transferred from a specially selected "conversion surface" to the neutral particle which scatters off the surface under a glancing angle [*Wurz*, 2000]. The negative ion is then analyzed and accelerated to a detector. Degradation of both the "start surface" and "conversion surface" will impact instrument sensitivity.

Degradation of a conversion surface generally means that the chemical composition of the top-most monolayer of the surface changes because of adsorption of gases on the active surface, which reduces the conversion efficiency. However, some instruments rely on an active monolayer to increase efficiency and degradation occurs with the removal of this active layer by sputtering or evaporation. An example of the latter is the LENA instrument on the IMAGE satellite [*Moore et al.*, 2000]. LENA used a highly polished tungsten conversion surface. Like all metals exposed to air, the tungsten was covered with a thin water/oxide layer, which improved the ionization efficiency by a factor of about three. However, that layer was lost when exposed to high vacuum in space. Fortunately, the perigee of the IMAGE satellite carried it low enough that exospheric oxygen replenished the oxide layer and maintained constant ionization efficiency during the mission. Nowadays, conversion surfaces are used that do not degrade by losing their active layer [*Wurz*, 2006]. The only method of degradation of such surfaces is the adsorption of gases and their possible decomposition by UV photons. This can be mitigated by a stringent cleanliness program and low outgassing of the instrument. In particular the instrument

should spend several days in high vacuum to eliminate any surface contaminants before UV light is allowed to illuminate the conversion surface.

Identifying degradation of "start surface" kinetic secondary electron emission yields can be made in a manner similar to other time-of-flight efficiency determinations. By monitoring the ratio of valid start-stop combinations to single event stops, one can determine the start efficiency (see Section 4.3.2). However, this monitoring requires that the single event stops are dominated by actual ENAs and not the result of other singles background such as UV photons or penetrating radiation. Start surfaces that are currently used are very flat high-Z material that often have a multi-layer coating to suppress forward scattering of UV light [*Barabash et al.*, 2004] and thereby facilitate this efficiency calibration. Degradation of the "stop detector" can also be monitored in the same manner at time-of-flight stop detectors by measuring the ratio of valid events to single starts (see Section 4.3.2). Again this monitoring requires that the single's start rate be dominated by ENA and not by other sources of background.

ENA instruments experience similar background from UV photons and penetrating radiation as neutral gas instruments, with the background arising from UV photons typically being the most important source. Both types of instruments have straight entrance systems that eliminate most charged particles through electrostatic deflection, but are susceptible to contamination by UV light. Both have detectors that can register UV photons and penetrating radiation. ENA instruments incorporate UV light absorbing materials on their internal surface to reduce this background. For ENA instruments with CEM or MCP detectors, background due to radioactive decay in the glass may also be important.

Background in ENA instruments is exacerbated by the low intensity fluxes that are measured, where signal to noise may be small. Therefore background subtraction is an important part of the ENA data analysis. UV light from stars can be significant, but can also be used to monitor the instrument's susceptibility to this background since stars generally have constant light output. This UV background signal can also be used to derive the relative start and stop detection efficiencies during the instrument's operation in space. If the single events are dominated by UV and not by ENAs (as is the case for the simpler ENA instruments) and the UV source (stars, backscattered Lyman-α, etc.) stays constant with time, the single event rate will vary only with detector efficiency. Since the absolute detection efficiencies for Lyman-α photons and particles are different, only relative information of the detector efficiency with time is derived. The absolute relationship can be established early in the mission when the detection efficiency for particles is known from the ground calibration. For ENA instruments that use time-of-flight, coincidence timing will eliminate single event background unless this background becomes comparable to the detector cycle time for an event, which may happen in ENA instruments. Background from penetrating radiation will generally introduce a slowly varying, spin-dependent, single event rate that is independent of any analyzer dependent settings.

4.3.6 Identifying Degradation in Faraday Cup Instruments

As pointed out in Section 4.2.7, the long term stability of a Faraday cup instrument depends on the stability of the electronics. The stability of the electronics can be tested by an internal calibration system that can inject known currents at the input of the measurement chain to stimulate the entire system including the analog to digital conversion circuits. The injected currents can be stepped over the entire dynamic range of the instrument

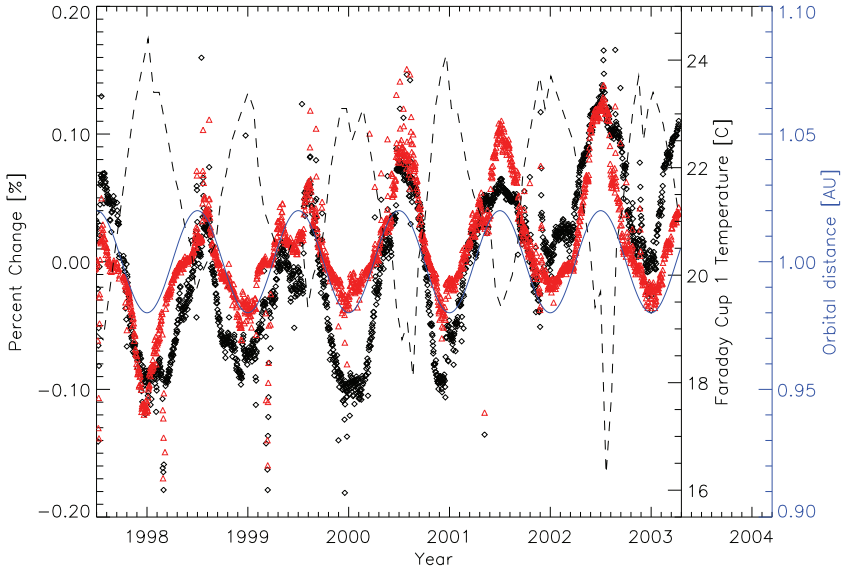

Figure 4.17: The variation in the response of the two Faraday cups on the Wind spacecraft over nearly 6 years as determined by the internal current calibration. The symbols are the percent variation in the instrument responses, and the dashed line is the temperature of the instruments obtained from housekeeping data. The orbital distance of Earth, and hence the spacecraft, from the Sun is shown as the solid line. Adapted from *Kasper et al.* [2006].

and provide complete end-to-end characterization of the electronics. A full description of the internal calibration system used in the Wind Faraday cup experiment is given in Chapter 3.

An internal calibration of the two Faraday cup (FC) instruments on Wind was performed every 92 seconds. Figure 4.17 is a plot of the percent change over time in the response of the two FCs to the nominally-same internal calibration current (each generated independently by that instruments's calibration system.) The symbols in the figure indicate the evolution over time of the response of each instrument to the same calibration signal. Note that there is a $<0.1\,\%$ variation in the reported current with a period of one year which is seen independently by both instruments.

The solid line in Figure 4.17 is the orbital distance of the Earth from the Sun, which suggests that there is a change in the instrument response due to a temperature variation of the instruments as the distance to the Sun changes. Preflight thermal testing of the instrument did indicate that the RC circuit of the log analog-to-digital circuit had a one-part in a thousand per degree C temperature variation. Since this effect appears to be in the RC circuit, the internal calibration system could be used to remove this 0.1 % effect. In addition, there appears to be a 0.04 % overall gradual variation in the instrument response to the internal calibration signal.

4.3.7 Identifying Degradation in Langmuir Probes

4.3.7.1 Current-Measuring Probes

The primary method for identifying degradation or other problems arising in the operation of Langmuir probes in a high-density environment is a simple internal consistency check. The simple exponential relationship (Section 2.3.1) between the electron temperature T_e and the measured current I_e, $I_e(V) \sim \exp(eV/kT_e)$, when the Langmuir probe bias, V, is negative provides a powerful test of the validity of the T_e measurements. If the retarding region is not exponential, that measurement can be assumed to be invalid and should be discarded. *Brace et al.* [1971] showed that the ISIS-1 probes exhibited retarding regions that were exponential over a range of 6 or 7 kT_e.

Surface contamination (the main source of probe degradations) of the collector may introduce T_e errors, as discussed in the implementation section (Section 2.3.5). The accuracy of the electron and ion density, N_e and N_i, measurements can be of the order of 10 % after corrections of N_e for certain systematic errors. Errors can be detected and assessed most readily by comparing the N_e and N_i measurements from the same $I - V$ curve. N_e and N_i are independently measured because they come from different regions of the $I - V$ curve. Since plasma neutrality requires N_e to equal N_i, we are free to use either as a measure of the density. The N_e measurements extend to lower densities because the electron saturation current is about a factor of 50 greater than the ion saturation current for the same density. However, the N_i measurements are more accurate, at least in the F-region of the ionosphere, because the ion saturation current is almost exclusively due to the sweeping up of heavy ions by the known cross sectional area of the probe. In high density plasmas, major departures of the observed $I - V$ curve from the theoretical functional dependence, or significant disagreements between the independent measures of N_e and N_i, are indications of an instrument problem, possibly due to probe contamination.

A final method of assessing Langmuir probe operation is through comparisons between the measurements of two independent Langmuir probes on the same rocket or satellite. This may identify additional measurement errors that do not show up in the internal consistency checks. Systematic differences may arise from mechanical failure, surface contamination of one or both probes, or differences in mounting location.

4.3.7.2 Voltage-Measuring Probes

Radiation damage to the probe's preamplifier is the primary source of degradation and may be ascertained in three ways. First, the current required to balance the apparent photoemission may increase because of increased leakage currents in the damaged circuit. Second, the signal output of an electric field measurement may decrease with time because of the voltage divider effect of the plasma sheath and the decreasing input impedance of the preamplifier. Third, the preamplifier output may be forced to one of its power inputs and become locked rather than track the plasma potential.

A determination of changes in the photoemission current can be made by examining the current-voltage relation of the Langmuir probes. In particular, if the probe is biased very negative (∼tens of volts) with respect to the nearby plasma, all photoelectrons will escape the probe while fewer plasma electrons will be captured. Thus the current to a probe at very negative potentials will provide a measure of the photoemission current, after a small correction due to the thermal plasma. This test can be run occasionally to

monitor photoemission, however care must be taken not to drive the spacecraft to large positive voltages during the test, such that the probe-to-plasma potential becomes small. Generally this means performing the test on one probe at a time, with the other probes monitoring spacecraft potential.

4.3.8 The Use of Artificial Signal Injection for Instrument Performance Verification

Thus far the material in Section 4.3 has dealt primarily with determining the proper performance of the front-end detector portions of various types of instrumentation for observing particles and plasmas in space. However, it is equally important that these instruments are capable of in-flight testing and verification that the down-stream processing of the signals from the sensor heads is done properly. Modern detector systems invariably test the system performance by injecting pulses of varying amplitude, frequency, and phasing at various points in the data processing chain to perform this function.

For example, many instruments designed to observe energetic particles use multi-element solid-state detector assemblies. Pulse height analyzes of the signals produced in coincidence from each of the detectors are used to identify both the energy and the species of the particle that transited the detectors. Artificially injecting pulses of various amplitudes simultaneously at each of the sensor signal inputs will verify that the pulse height analysis required of such detectors is being performed properly and that the requirement for coincidence in signals from multiple sources is satisfied. The MEPED instrument on POES (described above) is one such example. Similar use of pulse stimulation is described by *Fritz and Cessna* [1975] for the ATS-6 instrument, by *Weiss and Wilken* [1987] for the Implanted Ion Spectrometer instrument flown on the Giotto mission, by *Williams et al.* [1994] for the EPIC (Energetic Particles and Ion Composition) instrument on Geotail, and by *Sharber et al.* [1996] for the PEM (Particle Environment Monitor) on the UARS satellite. *Wilken et al.* [1997] have a thorough explanation of the complex and encompassing use of artificial pulse injection to perform in-flight testing of the RAPID instrument for the Cluster mission.

Time-of-Flight instrumentation has similar requirements for testing the processing of signals generated from the sensors (MCPs and solid-state detectors) with the added complexity of accurately determining the time interval between two independent signals. Again, the artificial injection of pulses at selected points in the signal processing chain with, possibly, variable phasing, is the most effective way of verifying proper operation of the on-board analysis of the multiple signals. *Rème et al.* [1993, 1997] describe the use of artificial pulses to verify proper operation of the Cluster CIS instrument while *Klumpar et al.* [2001] describe the use of this method for a similar TOF instrument flown on the FAST satellite.

Amplitude and frequency variable pulse injection was used in the plasma instrument on AMPTE-IRM not only to test threshold discriminators but, by slaving the pulse frequency to the ESA plate voltage, also verified the analyzer sweep voltage profile. In the same instrument other pulse modes were used to check the data gathering logic and the on-board computation of plasma moments [*Paschmann et al.*, 1985].

Even the simplest plasma instruments benefit from injecting artificial pulses into the amplifier-discriminator electronics. This is especially valuable when the threshold discrimination levels can be stepped in order to obtain a PHD from CEMs or MCPs. Among

the numerous space particle instruments that have utilized artificial pulse injection for this purpose are the Helios plasma experiment [*Rosenbauer et al.*, 1981], the Interstellar Neutral-Gas Experiment on Ulysses [*Witte et al.*, 1992], the Solar Wind Ion Composition Spectrometer, also on Ulysses [*Gloeckler et al.*, 1983], the particle analyzers on FAST [*Carlson et al.*, 2001], and the TED sensor in the POES SEM-2 instrument [*Evans and Greer*, 2000].

4.4 Relative and Absolute Calibration of Plasma Instruments

4.4.1 Introduction

The necessity for accurate in-flight calibration of plasma sensors is becoming critical to the solution of many of the space plasma physics problems that require multi-spacecraft missions to resolve gradients in the plasma. The Cluster mission (launched in 2000) and the proposed Magnetospheric Multi-scale Mission (scheduled launch in 2013) both involve four spacecraft flying in close formation in order to resolve small scale (10–1000 km) structures in the plasma. The accuracy of gradient determination, and the new physics that can be learned from these missions, ultimately depends upon the accuracy of in-flight calibrations. For these types of science missions, measurement accuracies to better than 5 % are highly desirable.

Other spacecraft platforms, such as the DMSP and NOAA satellites, require periodic in-flight calibrations in order to provide effective long-term monitoring of Earth's auroral zones. The accuracy required of these calibrations efforts depends upon goals of the mission, with ∼30–50 % accuracy often being adequate. However, even these more relaxed calibration goals still require periodic testing of the sensors. Single spacecraft missions also require careful in-flight calibrations for proper interpretation of the observations. Interpretation of the local physical process and placement of the local observations in a global context typically require in-flight calibrations to better than 30 %.

Before embarking on determining either absolute or relative calibration of plasma sensors, the data set must be thoroughly qualified. As discussed in Sections 4.2 and 4.3, plasma instruments that include MCP or CEM detectors must verify that the detector gains are proper. Any sources of background or spurious responses should have been identified and the data corrected. If those responses are not corrected, those data should not be used in establishing relative or absolute calibrations.

Laboratory calibrations of the instruments may have exposed slight differences in analyzer characteristics, temperature variations of one sort or another, and other peculiarities of individual sensor systems. For example, non-concentric analyzer plates can introduce variations in both energy (a few %) and sensitivity (10–20 %) with look direction. Thermal drifts of resistors and offset drifts in operational (OP) amplifiers may lead to drifts in energy response. All variations in analyzer characteristics, temperature effects, and other factors exposed in laboratory calibrations must be introduced before in-flight calibrations are attempted. This section assumes the plasma data have been fully qualified and all known corrections have been made.

The efficiency of MCPs (or CEMs) may vary across the detector. The magnitude of these variations generally depends upon details of the pulse height distribution and the

preamplifier discriminator threshold, and may depend upon accumulated flux. In addition, efficiency variations are also caused by changing the angle between the particle velocity and MCP pore bias angle [*Gao et al.*, 1984]. For example, the top-hat analyzer RPA-1 on the Giotto spacecraft utilized a 360° annulus MCP chevron pair for detection [*Rème et al.*, 1987]. Because the electrons exited from the analyzer at an angle not perpendicular to the MCP plane, there was an azimuthal dependence of the average electron velocity relative to the individual microchannels. This problem was avoided on later missions (Wind, Mars Surveyor, FAST, Cluster) by splitting the MCPs into 180° C-shaped segments, with the bias angle direction centered on the C. Simulations and ground testing showed this was effective in eliminating the majority of MCP bias angle skewing. Even with this arrangement, pre-acceleration between the analyzer and detectors may introduce additional small efficiency variations due to changes in angle between particle velocity and pore bias.

The energy dependence of the MCP efficiency is also a part of relative calibrations. These variations in response are much more difficult to determine. The efficiency of an MCP varies much more for electrons (∼60 %) than for ions (∼20 %) over the energy range of most plasma instruments (0–30 keV) when nominal pre-accelerations of up to several hundred volts for electrons and 2–3 kV for ions are used. Attempts to determine the energy dependent efficiency based upon in-flight calibrations have been made for instruments on Geotail, Wind and Polar and are described in the following sections.

It is important to understand how errors in the determination of relative efficiencies effect the measurements. The dependence of detector efficiency on incident particle energy is generally noticed in the even moments (density, pressure). For multi-spacecraft missions where density or pressure gradients are important, the use of the same functional dependence on energy and cross-calibration of the sensors on different spacecraft reduces the chance that errors in this dependence will introduce significant errors in the gradients. Errors are more likely to be detected when comparing plasma parameters from different instrument types, such as electron and ion sensors, or by spectral comparisons between different instruments.

Variations in efficiency with look-direction will impact primarily the odd moments (velocity, heat flux). Since much of the physics is often tied to particle or energy flows, determination of the relative efficiency with look direction is often more critical. This relative efficiency can be determined by comparing sensor counting rates during times of isotropic particle distributions, or at similar pitch angles at times when the distributions are anisotropic. If convective flows are present, care must be taken to transform the distribution before pitch angle comparisons are made. Since the transformation to the proper reference frame will often depend upon the uncalibrated data, it is best to minimize these transformations to avoid any feedback in the process. Spacecraft charging must also be properly accounted for, especially if the potentials are large enough to significantly affect particle trajectories. Problems introduced by both flows and spacecraft charging favor performing these calibrations using the more energetic portion of the particle population. When performing such calibrations, care should be taken to avoid regions where pressure gradients can introduce flows or where non-gyrotropic distributions are present.

This section first describes the physical principles governing plasmas in space that are used as a basis for determining relative and absolute calibration of plasma sensors. The limitations in the use of those principles are discussed as well as advice on the proper choice of physical location and conditions that are most conducive to obtaining high quality calibrations. A number of specific examples illustrating the use of these physi-

cal principles for calibration of various types of plasma sensors on a variety of missions is then provided.

The reader will appreciate that similar calibration procedures are used for different instruments and for similar instruments on different science missions, so there may be unavoidable duplication in the following material.

4.4.2 Physical Principles

In this section, we will describe methods for in-flight calibration of plasma instruments that are based on independent determinations of the plasma density, on quasi-neutrality of the plasma, on constraints on the ion and/or electron distributions imposed by gyrotropy and the direction of the magnetic field, and on pressure balance. The examples of in-flight calibrations described in the subsequent sections are largely based on applications of one or more of these methods.

4.4.2.1 Use of Wave-Determined Plasma Densities

One of the most common methods of checking a plasma instrument's response is by comparing the local plasma density inferred from wave measurements to the density determined by integrating the distribution of particles. This method is used to determine the "absolute calibration" or "integral sensitivity" of the instrument. The accuracy of the method depends upon the plasma instrument's relative calibration, the measurement of all significant plasma components, the proper identification and correction for ion mass and spacecraft charging, and the accuracy of the density determined from the data of the wave instrument. Whereas relative calibrations are typically stored as a set of numbers approximately equal to one, representing small variations in instrument response with angle and energy, the absolute calibration is stored as a single number that provides an integral sensitivity (or total geometric factor) for the instrument. The combinations of absolute and relative calibrations are then used to scale count rates to obtain absolute flux values.

The simplest wave determined density calibration involves identification of the plasma frequency,

$$\omega_p = 2\pi f_p = \sqrt{\frac{N_e e^2}{m_e \epsilon_0}} \tag{4.1}$$

from naturally occurring Langmuir waves. For $f_p \gg f_{ce} = eB/(2\pi m_e)$, as is the case in the solar wind and magnetosheath, the Langmuir wave dispersion relation can be approximated as $\omega^2 = \omega_p^2 + \frac{3}{2}k^2 v_e^2$ where v_e is the electron thermal velocity and k the wavenumber. Short-wavelength waves, for example those produced in the electron fore-shock, may have frequencies that deviate from f_p due to finite k effects and/or Doppler shifts. In addition, electromagnetic waves may be present and dominate the spectra. The EM wave field typically has a broad frequency spectrum with cutoff near f_p. Therefore what is commonly used as a proxy for f_p is the sudden drop in wave power near f_p. The accuracy of this method ultimately depends upon the frequency resolution of the measured wave spectrum, the relative sampling between wave spectra and particle density, and the presence of long wavelength waves. The finite k effects can be alleviated by the use of a relaxation sounder as described in Section 2.10.

Recent observations within the Earth's magnetosphere have shown that cold plasma can dominate the local density in the dayside plasmasheet [*Sauvaud et al.*, 2001], nightside plasmasheet [*Seki et al.*, 2003], plasmasheet boundary layer [*Etcheto and Saint-Marc*, 1985], lobes [*Hirahara et al.*, 1996], polar cap [*Su et al.*, 1998] and plasmasphere [*Lemaire and Gringauz*, 1998]. Cold ions in these low density regions are not detected by plasma instruments due to the spacecraft charging (unless flows are large, see *Sauvaud et al.* [2001]), and so care must be taken when selecting times for magnetospheric density calibrations. Note that even in small quantities, such cold ions can affect the wave modes, or in case of oxygen, have a major effect on the mass density of the plasma.

Cold electrons can also be a significant component in the magnetosphere, especially within the plasmasphere, lobes and plasmasheet boundary layer. These electrons are difficult to separate from spacecraft photo-electrons since most instruments tend to mix these populations in the energy channel that corresponds to the spacecraft potential.

Magnetospheric measurements may also have significant concentrations of heavy ions (O^+, He^+) and proper integration of the ion distribution functions requires knowledge of particle mass. For non-mass resolving sensors, care must be taken in the selection of calibration times and locations in order to minimize high-mass components. In the near-Earth environment, relative calibrations are often determined within the magnetosphere where bulk plasma flows are generally lower and particle distributions are both hotter and more isotropic. However, density inter-calibrations are better performed within the magnetosheath or solar wind where cold plasma is not present and the contribution from heavy mass ions (He^{2+}) can be estimated from solar wind spectra.

In comparing wave and particle determined densities, care must be taken to perform the particle integrals correctly. The most common errors involve mistreatment of spacecraft charging, the exclusion of some portion of the plasma, or the failure to properly account for different mass ions. In Section 4.4.2.2 we present a discussion on how to properly integrate a distribution, accounting for spacecraft charging. To minimize the impact of different mass ions, density calibrations within the magnetosphere should avoid magnetic storm periods where ionospheric O^+ and He^+ outflows contribute significantly to the density.

For measurements by non-mass-resolving ion sensors in the solar wind or magnetosheath, the assumption of H^+ introduces a fractional underestimation of the inferred density used for inter-comparison with wave determined density (N_e),

$$\frac{N_{H^+} + N_{He^{2+}}/\sqrt{2}}{N_{H^+} + 2N_{He^{2+}}} \approx 1 - 1.29\frac{N_{He^{2+}}}{N_{H^+}} \tag{4.2}$$

for $N_{He^{2+}} \ll N_{H^+}$. The error results from the estimated number density using the incorrect mass/charge, where calculated density is proportional to $(m/q)^{0.5}$, and including the dual charge on the He^{2+}. If composition data are available, the correction should be made. This error is of similar magnitude to errors in wave-determined density.

4.4.2.2 Calculating Particle Moments and Correcting for Spacecraft Charging

Many of the techniques described in subsequent sections involve the comparison of the particle moments with other measured physical quantities. Discussions of unit conversion from count rate to differential flux or distribution function can be found in Chapter 1, along with an overview of particle moment computation (see also Appendix D.3). However an

aspect of these calculations that is not addressed is the correction for spacecraft charging. Corrections for particle acceleration from the plasma to the spacecraft are often either incorrectly performed or ignored. For most geophysical plasmas, these corrections are essential for accurate moment computations, therefore we provide a brief description of this process.

To understand the correct methodology for correcting plasma moments for spacecraft potential, we recall the basics of plasma instruments. A plasma sensor measures a count rate, R. The instrument's geometric factor, G, sets the open area, energy and angle range accepted by the detector. G has nominal units of (cm^2 sr eV). Dividing R by G gives differential number flux, J',

$$J'(E', \Omega') = \frac{R(E', \Omega')}{G(E', \Omega')} \tag{4.3}$$

with units of $(\mathrm{s\,cm^2\,sr\,eV})^{-1}$. Here we use $'$ to distinguish the internal analyzer energy, solid angle and differential flux, E' and Ω', and J' from the values far from the spacecraft, E and Ω and J.

Since an analyzer's internal relative voltages do not depend upon spacecraft charging, the measured differential fluxes represents the plasma at the entrance aperture after it has undergone any accelerations by the spacecraft potential. This differential flux measurement can then be converted into units of phase space density, which again defines the plasma at the instrument's entrance aperture. It is important that this conversion to distribution function, $f'(E', \Omega')$, use the analyzer energy, E', and not the particle energy far from the spacecraft, E.

$$f'(E', \Omega') = \frac{m^2}{2E'} J'(E', \Omega') \tag{4.4}$$

where m is the particle mass. Since phase space density is conserved in electrostatic accelerations, internal phase space densities are the same as phase space densities far from the spacecraft,

$$f'(E', \Omega') = f(E, \Omega) \tag{4.5}$$

with the plasma being transformed from E, Ω to E', Ω' as it accelerates through the spacecraft potential. Corrections for spacecraft charging are reduced to mapping energy and solid angle. For calculating plasma moments, we recall that Nth order moments involve integrals over $f(v, \Omega)$

$$\mathsf{M}^N_{lmn\ldots} = m \int_\Omega \int_0^\infty (\boldsymbol{s}_l \boldsymbol{s}_m \boldsymbol{s}_n \ldots) v^N f(v, \Omega) v^2 \, \mathrm{d}v \, \mathrm{d}\Omega \tag{4.6}$$

where the number of subscripts $(l, m, n \ldots)$ is N, and each subscript varies over x, y, and z. The $\boldsymbol{s}_l$ are unit vectors: $\boldsymbol{s}_x = \boldsymbol{i} \cos\theta \cos\varphi, \boldsymbol{s}_y = \boldsymbol{j} \cos\theta \sin\varphi, \boldsymbol{s}_z = \boldsymbol{k} \sin\theta$. We transform the dependence of this equation from velocity to energy:

$$\mathsf{M}^N_{lmn\ldots} = m \int_\Omega \int_0^\infty (\boldsymbol{s}_l \boldsymbol{s}_m \boldsymbol{s}_n \ldots) \left(\frac{2}{m}\right)^{(N+1)/2} E^{(N+1)/2} f(E, \Omega) \frac{\mathrm{d}E}{m} \, \mathrm{d}\Omega \tag{4.7}$$

assuming a non-relativistic transformation. We now transform from the unmeasured E, Ω to the measured analyzer values of E', Ω':

$$\begin{aligned} \mathsf{M}^N_{lmn\ldots} = m \int_{\Omega'} \int_{-q\Omega}^{\infty} (\boldsymbol{s'}_l \boldsymbol{s'}_m \boldsymbol{s'}_n \ldots) \left(\frac{2}{m}\right)^{(N+1)/2} (E' + q\Phi)^{(N+1)/2} \\ \cdot f'(E', \Omega') \frac{\mathrm{d}E'}{m} \mathrm{d}\Omega' \end{aligned} \tag{4.8}$$

where q is the particle charge and Φ is the spacecraft potential relative to the plasma. The energy integral is limited to values $> -q\Phi$ to prevent inclusion of spacecraft generated particles. For $q\Phi > 0$, the lower limit of the integral is set to zero and a portion of the distribution is not measured. This may result in significant moment calculation errors if a cold component is not measured by the sensor. Note that angular deflections of particles will result in a functional dependence of $\boldsymbol{s'}_l$ on Φ and E [i.e., $\boldsymbol{s}_l(\theta, \varphi) = \boldsymbol{s'}_l(\theta', \varphi', E', \Phi)$]. If spacecraft charging introduces significant deflection of incident particles and if the distribution function is anisotropic, accurate moment calculations may require a ray tracing effort to determine the $\boldsymbol{s}_l$ to $\boldsymbol{s'}_l$ mapping.

Finally we convert distribution function back to measured count rate,

$$\begin{aligned} \mathsf{M}^N_{lmn\ldots} = m \int_{\Omega'} \int_{-q\Phi}^{\infty} (\boldsymbol{s'}_l \boldsymbol{s'}_m \boldsymbol{s'}_n \ldots) \left(\frac{2}{m}\right)^{(N+1)/2} (E' + q\Phi)^{(N+1)/2} \\ \cdot \left(\frac{m^2}{2E'}\right) \frac{R(E', \Omega')}{G(E', \Omega')} \frac{\mathrm{d}E'}{m} \mathrm{d}\Omega' \end{aligned} \tag{4.9}$$

and rearrange some terms to get:

$$\begin{aligned} \mathsf{M}^N_{lmn\ldots} = 2 \left(\frac{m}{2}\right)^{(3-N)/2} \int_{\Omega'} \int_{-q\Phi}^{\infty} (\boldsymbol{s'}_l \boldsymbol{s'}_m \boldsymbol{s'}_n \ldots)(1 + q\Phi/E')^{(N+1)/2} \\ \cdot (E')^{(N-1)/2} \frac{R(E', \Omega')}{G(E', \Omega')} \mathrm{d}E' \mathrm{d}\Omega' \end{aligned} \tag{4.10}$$

Equation 4.10 provides a general formula that corrects particle moments for a spacecraft potential. When these measurements are made by top-hat electrostatic analyzers with microchannel plate or CEM detectors, the geometric factor can often be approximated as:

$$G_{\mathrm{ESA}}(E', \Omega') = g E' \varepsilon(E') \alpha(\Omega') \tag{4.11}$$

where g is a constant, $\varepsilon(E')$ represents the energy dependence of the detector, and $\alpha(\Omega')$ the angle dependence of the combined analyzer-detector. Both $\varepsilon(E')$ and $\alpha(\Omega')$ are nominally close to unity. $\varepsilon(E')$ is generally a slowly varying function of E' as discussed in Sections 2.2.3 and 2.2.4. $\alpha(\Omega')$ includes the small changes in sensitivity resulting from detector non-uniformity or variations in analyzer open area. Substituting we get:

$$\begin{aligned} \mathsf{M}^N_{lmn\ldots} = \frac{2}{g} \left(\frac{m}{2}\right)^{(3-N)/2} \int_{\Omega'} \int_{-q\Phi}^{\infty} (\boldsymbol{s'}_l \boldsymbol{s'}_m \boldsymbol{s'}_n \ldots)(1 + q\Phi/E')^{(N+1)/2} \\ \cdot (E')^{(N-1)/2} \frac{R(E', \Omega')}{\varepsilon(E')\alpha(\Omega')} \frac{\mathrm{d}E'}{E'} \mathrm{d}\Omega' \end{aligned} \tag{4.12}$$

For most practical computations, the integral is replaced by a sum and becomes:

$$\mathsf{M}^{N}_{lmn\ldots} = \frac{2}{g}\left(\frac{m}{2}\right)^{(3-N)/2} \sum_{E'>-q\Phi} \sum_{\Omega'} \Big[(1+q\Phi/E')^{(N+1)/2}(E')^{(N-1)/2} \cdot \varepsilon(E')^{-1}\frac{\mathrm{d}E'}{E'}\Big] R(E',\Omega')\Big[(\boldsymbol{s}'_l\boldsymbol{s}'_m\boldsymbol{s}'_n\ldots)\alpha(\Omega')^{-1}\mathrm{d}\Omega'\Big] \tag{4.13}$$

where we have explicitly ordered the energy and angle dependence within the sum. If angle deflections can be assumed to be small so that $\Omega' \sim \Omega$ and $\boldsymbol{s}'_l \sim \boldsymbol{s}_l$, then the above sum is rather straight forward and readily calculated. For top-hat style sensors viewing primarily radial rather than tangential to spacecraft surfaces, and especially if the instrument is deployed on a short boom away from spacecraft surfaces, the small deflection approximation ($\Omega' \sim \Omega$) will be valid except for the lowest energy particles. In this case, accurate moments are relatively simple as long as the bulk of the plasma is observed at $E' > -q\Phi$ and as long as accurate measurements of spacecraft potential are available.

When an independent measurement of spacecraft potential is available, as from a Langmuir probe, the energy mapping is relatively simple. A current biased Langmuir probe will float near the plasma potential and measure the spacecraft-to-probe potential difference (see Sections 2.3.7). The energy shift should include an additional potential shift of ~1–2 V that represents the probe-to-plasma potential. When an independent measurement of spacecraft potential is not available, a distinguishing feature in the particle spectra can be used to determine the spacecraft potential. These corrections are generally most important for high-altitude, low-density plasmas where spacecraft charging varies from ~5 V to >40 V. The most easily resolved features in these regions are the spectral inflections that mark the boundary between spacecraft photoelectrons and plasma electrons.

Distribution function corrections are more difficult when angle deflections of the particles approaching the spacecraft are significant. For a sensor that views radially away from the spacecraft, angle deflections should be negligible. However, for fields-of-view that are near tangent to spacecraft surfaces, angle deflections may be significant, especially at energies just above the cutoff energy determined by charging. Detailed ray tracing using the spacecraft and sensor geometries may be required. These deflections cause the largest problems when significant cold populations are present. For electrons these corrections can in principle be made since positively charged spacecraft do not exclude any of the distribution from access to the instrument. For ions the retarding potential may eliminate a significant fraction of the ion population. If cold plasma measurements are important for the science goals, the best solution is to minimize the problem by deploying the sensor on a boom away from the spacecraft and biasing the sensor near the plasma potential.

4.4.2.3 Charge Neutrality

Except on very small spatial scales, space plasmas are neutral. Charge density equality is a powerful tool for establishing instrument relative and absolute calibration. Of course, care must be taken that such comparisons are only made when there is evidence that the distributions of ions and electrons are measured completely, no photoelectrons contaminate the electron measurement, and no cold ion species are being missed.

4.4.2.4 Gyrotropy

For distributions that are gyrotropic (i.e., have cylindrical symmetry around the magnetic field direction in the bulk velocity frame), the 3-D distribution becomes 2-D (pitch-angle and energy). A set of sensors rotating with the spacecraft will observe particles at a range of pitch angles depending on the orientation of the magnetic field relative to the spacecraft spin axis. A large and overlapping range of pitch angles is often sampled by the different sensors. If the data are pitch angle sorted as a function of energy, one can intercompare the measured response for the times when different sensors sample the same pitch angles. If those times are not too far apart, one can assume the input fluxes have not changed and the response should be the same. In this way one can calibrate the relative geometric factors, including detection efficiencies as a function of energy.

The gyrotropy assumption is quite commonly fulfilled for electrons. For electrons one may be able to ignore the velocity transformation into the plasma bulk frame. However if the electron spectrum is steep, even small velocities much less than the electron thermal velocity can cause significant differences in count rate between the flow and anti-flow directions so care should be taken. For ions, it is critical to go into the bulk velocity frame, or more conveniently, to select times where bulk velocities are negligible. For ions, one must also avoid the vicinity of plasma boundaries where finite gyro radius effects introduce non-gyrotropy to the distributions.

For low altitude satellites, plasmasheet population outside the loss cones generally provides the most isotropic fluxes suitable for detector inter-comparisons. The auroral regions should be avoided because there are significant spatial structures that can be crossed in a single spacecraft rotation that give rise to ambiguities in the comparisons. For interplanetary missions, variations in the magnetic field direction and the relatively high electron thermal velocities allow look-direction relative calibrations for electron plasma sensors. In-flight calibrations of ion plasma sensors in the solar wind are more difficult because of the high drift to thermal velocity ratio. If these calibrations are crucial to the mission success, it may warrant performing spacecraft maneuvers that allow the sensor field-of-view to rotate through the solar wind flow direction in order to calibrate its response.

Another approach is based on the effect of gyrotropy on the ion or electron pressure (or temperature) tensors. These tensors can always be diagonalized through a major-axis transformation, with diagonal elements P_{11}, P_{22}, P_{33} and zero off-diagonal terms. For distributions that are gyrotropic, but have a significant anisotropy, one of the major axes should be aligned with the magnetic field. Any misalignment is thus an indicator of imperfect calibration. Similarly, one could use the computed heat flux. As the magnetic field impedes heat flow in the perpendicular direction, the heat flux vector is expected to be aligned with the magnetic field. From a large data base of pressure anisotropies or heat fluxes (and associated magnetic field directions) one could thus derive an improved (relative) calibration.

The gyrotropy principle was used in the in-flight calibration of plasma instruments on Geotail (Section 4.4.3), Polar (Section 4.4.4), and Cluster (Section 4.4.6.2). A similar approach was used for particle sensors on board the AE-D satellite and those results are described by *Lin and Hoffman* [1979].

4.4.2.5 Pressure Balance

For one-dimensional, time-stationary plasma boundaries, momentum conservation implies constancy of the total pressure, plasma plus magnetic, across that boundary. So comparing the total pressure on the two sides of such a boundary provides a check of the (absolute) calibration factors behind the (perpendicular) plasma pressure, provided the magnetic field strengths are significantly different on the two sides. This technique is generally appropriate for ions only, because the electron pressure is usually a small (10 %) fraction of the plasma pressure. However, both electron and ion pressures should be included in the pressure balance calculation. Pressure balance has been used in the calibration of the CIS/CODIF mass spectrometer on Cluster, as described in Section 4.4.6.3.

4.4.2.6 Alfvén Waves

Alfvén waves are characterized by a quantitative relation, $\Delta \boldsymbol{V} = \Delta \boldsymbol{B}/\sqrt{\rho\mu_0}$, between the magnitude and direction of the wave-associated variations, where $\Delta \boldsymbol{V}$ and $\Delta \boldsymbol{B}$ are variations in the plasma bulk velocity and magnetic field, with ρ being the mass density of the plasma and μ_o the permeability constant. This relation is routinely used for identifying Alfvén waves, but to our knowledge has only been applied once for calibration purposes. During the encounter with comet Halley, magnetic field and plasma observations on board the Giotto spacecraft revealed in-phase perturbations that were assumed to be Alfvén waves, produced by the interaction of the comet with the solar wind. The variations in the instantaneous plasma bulk flow velocities, calculated from measurements by the three-dimensional positive ion analyzer on Giotto, displayed a near-linear dependence on the simultaneously measured variations in the wave's magnetic field, as expected [*Johnstone et al.*, 1987]. This result provided confidence that the plasma bulk flow velocity was being properly retrieved from the raw plasma measurements provided by the instrument.

4.4.2.7 Intra-Satellite versus Inter-Satellite Calibrations

While the calibration principles described above involve comparisons between sensors or instruments on the same spacecraft, and most of the mission specific examples in the following sections are in that category, the Cluster multi-spacecraft mission and the NOAA/POES missions described in Sections 4.4.6 and 4.4.7 are exceptions.

Multi-spacecraft missions provide the opportunity for cross-calibrations of identical instruments on different spacecraft that can be a powerful tool for obtaining relative calibrations. Naturally, this can only be done in situations where there is reasonable confidence that the plasma environments (densities, temperatures, etc.) are as nearly identical as possible at the spacecraft locations. The Cluster mission is particularly suited for both intra- and inter-satellite calibrations because its instruments are identical on all four spacecraft and the spacecraft often in close proximity exposing them to the same particle environment. An example of such an inter-satellite calibration for Cluster is presented in Section 4.4.6.4.

4.4.3 Geotail

The constraint for density equality is a powerful tool for establishing instrument relative and absolute calibration since the local density of ions and electrons cannot differ

by more than 1 part in 10^6 in the magnetosphere. This constraint was effectively used to perform the Geotail LEP (low energy plasma) in-flight calibratons. The following discusses the approach used to calibrate the EAi (Energy Analyzer for ions) instrument using ion moments, followed by a more detailed discussion of the EAe (Energy Analyzer for electrons) calibrations using electron moments.

The Geotail LEP instrument obtained angular distributions by using multiple detectors: seven MCPs in the ion instrument and seven CEM's in the electron instrument. There are certain corrections that must first be made to both the ion and electron data. These are for spurious response from penetrating particles (cosmic rays) and for the sensor responses to solar EUV, especially when the Sun is in the sensor field of view. The correction for cosmic ray response follows from the background response in locations where little or no low-energy plasma is present. The correction for EUV is based upon laboratory measurements and modeling. Once these background counts were removed, the ion and electron data were corrected for differences in relative efficiencies among these MCP and CEM detectors. Comparing detector responses when different detectors viewed the same particle energy and pitch angle (Section 4.4.2.4) established this correction.

Once these corrections were applied to the data from the EAi instrument, the computation of the moments was a straightforward integration of the 3-D distribution obtained from the instrument. The ion sensor's MCP efficiency was assumed to be independent of incident ion energy. The absolute calibration of the LEP ion instrument was then determined by comparing the density moment thus obtained with the plasma density obtained from the cutoff frequency of the continuum radiation as described also in Section 4.4.2.1. This comparison was made in regions of varying plasma densities and temperatures including the plasmasheet, the lobe, and the magnetosheath.

Implementing a similar procedure for electron moments is considerably more complex because of the influence of spacecraft potential and the photoelectron cloud produced at the spacecraft. For this reason, a more comprehensive discussion of the procedures for obtaining the electron moments is warranted.

The LEP electron data are significantly contaminated by instrumental photoelectrons and secondary electrons, especially at low energies (<60 eV) and when viewing in the sunward direction. Figure 4.18 shows omni-directional electron and ion energy-time spectrograms obtained on 14 October, 1993 when the Geotail spacecraft was in the distant tail lobe region ($X_{GSE} = -140\,R_E$.) The upper panel shows the spectrogram for electrons. Before 0946 UT significant fluxes of spacecraft photoelectrons were observed below 40 eV. According to a simultaneous Langmuir probe measurement, the spacecraft potential was +36 V at this time. Geotail has the capability to control the spacecraft potential using an Ion Emitter (IE) [*Tsuruda et al.*, 1994]. When the IE was turned on at 0946 UT, the spacecraft potential changed to about +2 V relative to the probe, or about +3 V to +4 V relative to the plasma. At the same time the energy where the photoelectrons were detected decreased to below 10 eV.

When the spacecraft potential was +36V, spacecraft photoelectrons were detected at almost all directions although the flux was most intense when the analyzer was viewing the Sun. When the spacecraft potential decreased to ∼+2 V, relative to the Langmuir probes, intense photoelectron fluxes were observed only in the Sun viewing sector. These latter photoelectrons are produced internal to the analyzer. Figure 4.19 shows detailed distribution functions observed when the LEP EAe sensor was viewing anti-sunward (left panels)

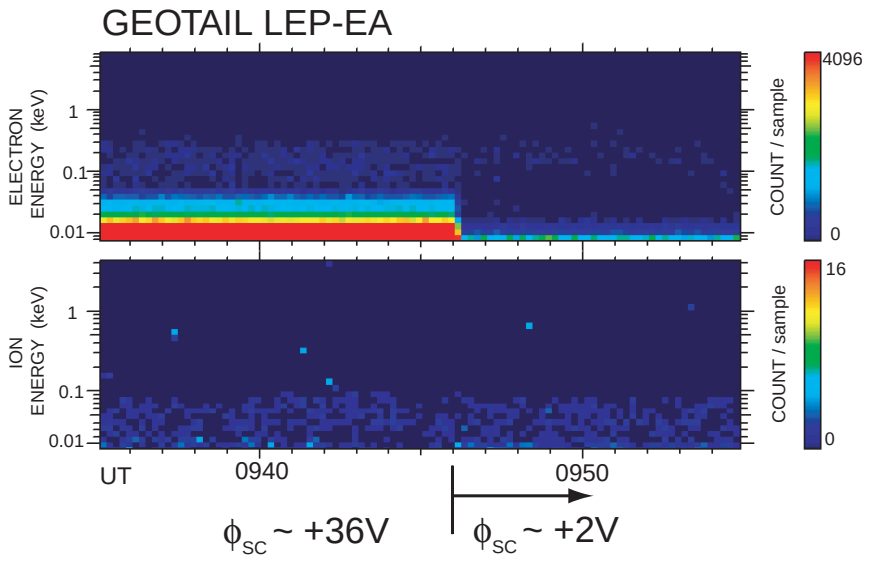

Figure 4.18: Electron and ion energy spectrograms spanning the time when the Ion Emitter was turned on and changed the spacecraft potential from ∼36 V to ∼2 V.

and toward the Sun (right panels.) All four data sets were taken when the spacecraft potential was ∼+2 V relative to the Langmuir probes.

Photoelectrons detected by the EAe instrument will greatly affect the computation of the electron velocity moments, especially the absolute value of the electron density. For this reason the contribution of photoelectrons generated at the spacecraft surface and within the analyzer were removed from the instrument response before such calculations were attempted. This was done by extrapolating the 50–100 eV plasma electron distribution back to lower energies assuming a thermal distribution. The dashed green curves in Figure 4.19 illustrate this extrapolation (straight line on a $\log(f)$ versus energy).

Once the EAe CEM responses were corrected for background, photoelectrons, and relative efficiencies, the computation of velocity moments up to third order proceeded in much the same fashion as for the ion data from the EAi instrument. The electron energies were corrected for the spacecraft potential as measured by the Langmuir probes. A large number of simultaneous electron and ion densities were obtained during measurement intervals in the plasmasheet and the averages of those densities $\langle n_e \rangle$ and $\langle n_i \rangle$ were calculated. Since electron and ion densities are equal, and since ion data were already calibrated, the ratio $\langle n_e \rangle / \langle n_i \rangle$ must represent the average efficiency of the EAe's CEMs for detecting electrons. To correct for the average CEM efficiency, each computed electron density was multiplied by $\langle n_i \rangle / \langle n_e \rangle$ to obtain a final value of electron density. Figure 4.20 shows the ratio between n_e (corrected in this manner) and n_i as a function of electron temperature T_e for a data set obtained in the plasmasheet when T_e was >300 eV. If there were no energy dependence in the CEM electron counting efficiency, the n_e/n_i ratios would cluster about 1.0 with the scatter being a measure of the overall experimental uncertainties in computing plasma densities. However, Figure 4.20 shows that the n_e/n_i ratio decreases

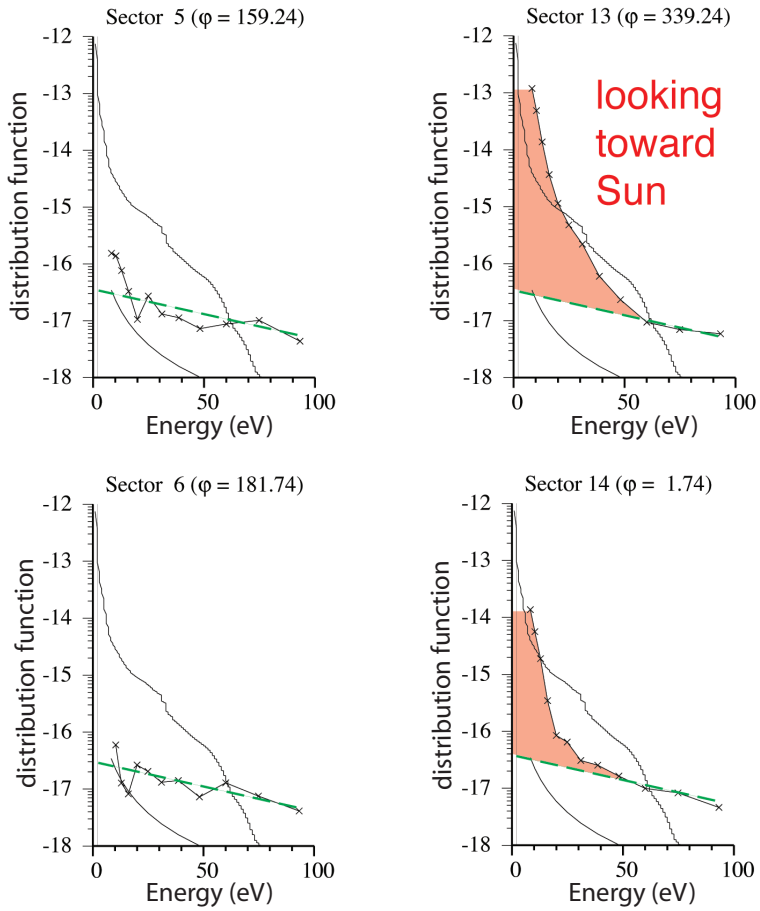

Figure 4.19: The sub-panels display details of the electron distribution functions in terms of phase space densities for four selected viewing sectors in the plane normal to the Geotail spin axis when the spacecraft potential was +2 V relative to the Langmuir probes. The sub-panels on the left are from sectors when the EAe instrument was viewing anti-sunward and in the shadow of the spacecraft while the sub-panels on the right are from sectors when the instrument was viewing toward the Sun and on the sunlit side of the satellite. The cross symbols in each panel are the electron distribution function obtained directly from the LEP EAe observations while solid line in the lower left of each panel marks the one count level of the detector system response. The second solid line in each panel, extending to very high value at low electron energy, is the modeled distribution of spacecraft generated electrons. The green dashed line in each panel is the extrapolation to lower energy of the electron distribution function observed at higher energies where photoelectrons would not contribute to the sensor response.

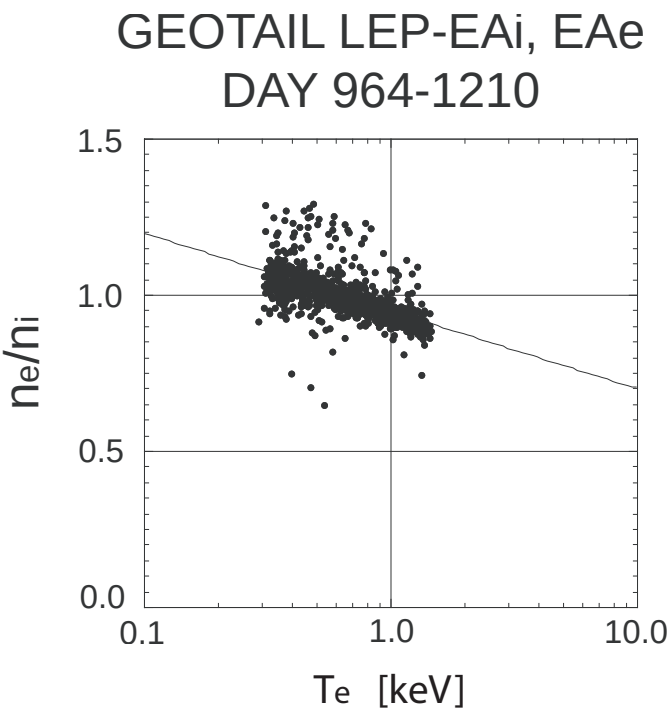

Figure 4.20: The ratio n_e/n_i as a function of electron temperature (in keV) obtained from many observations in the plasmasheet. The data have been corrected for photoelectrons and for differences among analyzers. While the data points cluster about 1.0, there is a clear dependence of the ratio upon electron temperature that demonstrates the need to account for the energy dependence of the CEM for detecting electrons.

with increasing electron temperature. This decrease is caused by the energy dependence in the efficiency of electron detection by the CEMs that had not yet been applied.

Figure 4.21 shows the energy dependence of CEM electron counting efficiency applied to the electron instrument EAe to remove the slope in Figure 4.20. This energy dependence is similar to the measured efficiency reported by *Archuleta and DeForest* [1971]. The energy dependent efficiency was applied only for electrons above 300 eV since a 250 V accelerating voltage is applied to the input of the EAe CEMs and the counting efficiency of a CEM is reported to be a maximum for a 300 eV, $\pm$200 eV, electron. The curve was derived by an iterative procedure of varying the energy dependent efficiency curve, recalculating electron velocity moments and reevaluating the dependence of n_e/n_i upon T_e until the n_e/n_i ratio was no longer dependent on electron temperature in the plasmasheet.

As described in Section 4.4.2.4, the relative efficiencies of the seven CEMs in the EAe instrument were established under the assumption of the angular distribution of electrons being gyrotropic. However, a careful analysis of the electron bulk velocity parallel to the Geotail spin axis (which was nearly perpendicular to the ecliptic plane) and its dependence upon electron temperature revealed the necessity for an additional, but very minor, correction to those relative efficiencies. Figure 4.22 displays scatter plots of the simultaneous measurements of that component of electron bulk velocity, V_{ez}, and electron temperature

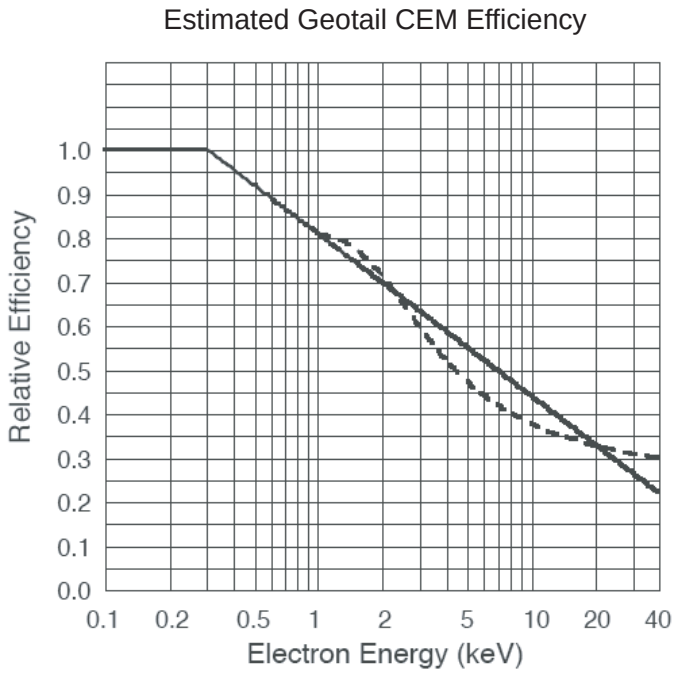

Figure 4.21: The solid line is the energy dependence of the CEM efficiency used to correct the Geotail LEP electron observations and eliminate the energy dependence in the n_e/n_i ratio in Figure 4.20. For comparison, the dashed line shows a fit of the energy dependence between 1 keV and 50 keV, normalized to 0.8 at 1 keV, reported by *Archuleta and DeForest* [1971].

T_{ezz}. The red points are for the case where the original CEM relative efficiencies were used in the analysis and show an unphysical dependence of bulk velocity upon electron temperature. If there remained a slight difference in relative efficiency between different CEMs, the averaged V_{ez} will deviate from zero, especially when the electron energies are high. Slight modifications to the relative CEM efficiencies were then assumed to remove the energy dependence of V_{ez} upon T_{ezz}. These final corrections were as small as a few percent. The different colors of the data points in Figure 4.22 correspond to the results that were obtained for different final corrections, the green points showing the most favorable result.

In conclusion, excellent in-flight calibrations were obtained for the Geotail LEP instrument using the described procedures to obtain consistent electron and ion velocity moments. It was more difficult to calibrate the electron sensor than the ion sensor because of contamination by photoelectrons and the effects of spacecraft potential. The final electron densities agree to within 10 % in most cases as illustrated by the scatter in the n_e to n_i ratios in Figure 4.20.

4.4.4 Polar-Hydra

The Hydra plasma investigation has been described by *Scudder et al.* [1995]. The following discussion describes the intracalibration work performed to balance the responses

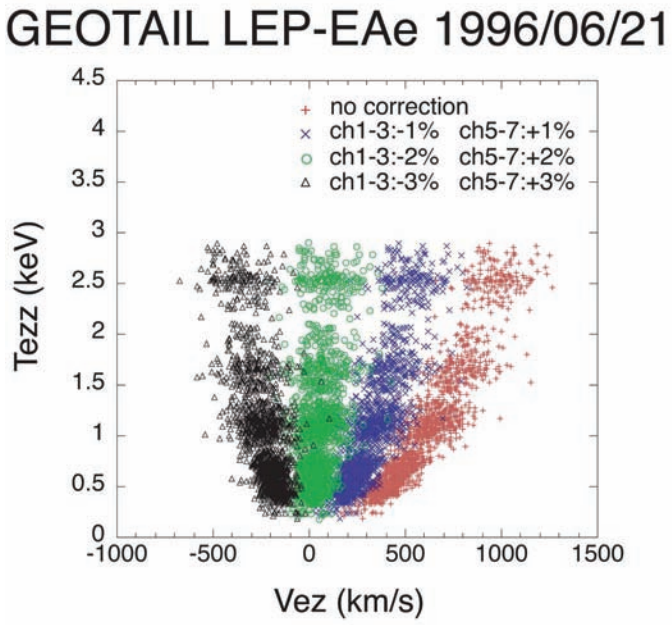

Figure 4.22: A scatter plot of the electron flow speed normal to the ecliptic plane as a function of electron temperature. The red points are the results obtained after introducing all the prior instrument corrections. The dependence of the flow speed on temperature indicated the need for small additional corrections to the analyzer responses. Corrections of only a few percent to some analyzers removed that dependence and the final results are shown in green.

of the separate sensors that make up this instrument. Hydra contains 12 cylindrical electrostatic analyzers mounted with anti-collinear fields of view in two separate boxes on opposite faces of the spacecraft. Six analyzers are in each box with their own stepping and detector bias supplies. Each analyzer has two, permanently biased channeltrons of the Sjuts type at its exit aperture, one for electrons and one for ions. The polarity of voltage sweeps on the spectrometer deflection plates are alternately reversed to transmit ions or electrons through the optics. All analyzers measure one complete energy sweep of electrons followed by a complete energy sweep of ions.

The Hydra calibration required that these analyzers measure a statistically significant, cylindrically symmetric distribution function when in hot plasmas and during periods when convection was not important. Thus the intracalibration involves making the data set statistically consistent with gyrotropy of the particle distribution function. Accordingly, convenient periods of time (1 week's data) were searched for intervals when different spectrometers measured particles of the same energy and pitch angle and when convection signatures were weak. All such matched measurements, regardless of counting rates should fall on a common line through the origin, where the slope determines the relative counting efficiency. By insisting that the different detectors measure the same energy and pitch angle (but in general different gyrophase) different pairs of measurements can be compared. Measurements are considered to have the same pitch angle so long as both

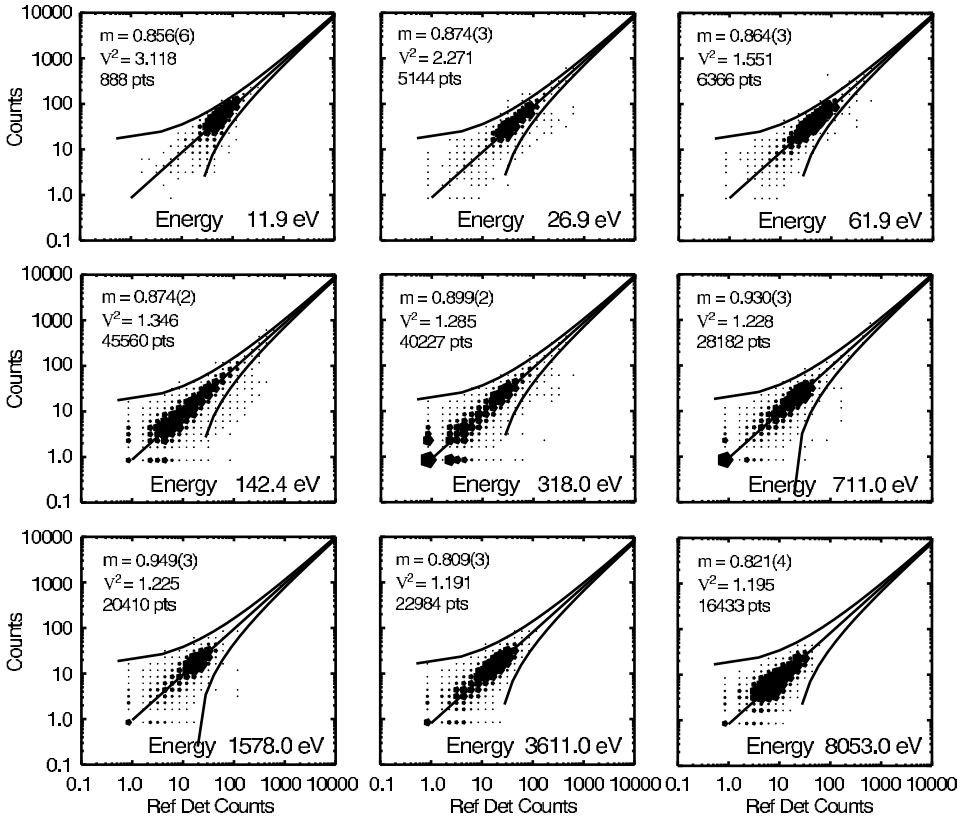

Figure 4.23: Scatter plots of the simultaneous response between Hydra Analyzer 7 and Hydra Reference Analyzer 12 after all intra-analyzer corrections have been made. The 9 panels correspond to 9 different electron energies.

elements in any given pair agree within the half-angle of the aperture acceptance, which is 5°. Measurement pairs by the j'th and k'th sensors are consolidated and sorted by energy to allow calculations of relative efficiency variation as a function of energy.

Appropriate attention must be given to the Poisson statistics involved for each counting rate in the pairwise comparisons of detectors. The least squares problem involves finding the appropriate proportionality constant $\mu_{j,k}$ between the k'th and j'th measurements. This determination reduces to finding the minimum chi-square dispersion from the prediction of the product of two Poisson probabilities of the observed rates. This procedure is a non-linear least-squares problem. In short, we desire a set of proportionality constants $\mu_{k,j}$ such that the probabilities $P(C_k)P(\mu_{k,j}C_j)$, $j \neq k$ as a theoretical distribution predicts in a least squares sense the occurrence distribution of the count pairs $(C_k(t_l), C_j(t_l))$, where both measurements are at the same time interval, the same energy, and same pitch angle.

A sample page of the results of such a calibration is shown in Figure 4.23. Each subpanel illustrates the correlation at a particular energy between Analyzer 7 and the reference analyzer numbered 12. All the correlations were acquired during one week's observations. Data from the radiation belt were excluded because of high background. The best

fit parameter of the joint probability above determines the slope of the line of proportionality through the origin with slope $\langle \mu_{7,12} \rangle$, where $\mu_{7,12}$ depends on particle energy, E_q. The size of the dots reflects the relative number of individual readings in that location for that panel. The high degree of organization seen in these examples is common across all possible combinations of the 12 sensors. Such a statistical and over-determined approach also affords an estimate for the uncertainties involved. Variations in these slopes were used over the life of the mission to motivate changes in the post acceleration voltages.

The above procedure implemented between all possible analyzer pairs yields $\langle \mu_{k,12}(E_q) \rangle$ so that all analyzers have calibration factors relative to one reference analyzer's measurement efficiency as a function of energy. The next step in the calibration procedure was to adopt a form for the relative efficiency versus energy of the reference analyzer's measurement. For electrons, the energy dependent efficiency given by the manufacturer (Sjuts) was used. Since the Hydra preacceleration of electrons was small (20–40 V), including the low energy variation of the CEM efficiency was crucial for obtaining accurate densities. For ions, the CEM efficiency was assumed to have no energy dependence above the post acceleration energy.

The final step in the calibration was the determination of the absolute quantum efficiency of the entire reference measurement. The absolute calibration requires cross checks with geophysical occurrences using measurement from other instruments. Examples are the Walén test [*Scudder et al.*, 1999] at Alfvénic structures where the absolute proportionality constant depends on the absolute density. Comparisons with solar wind Faraday cup measurements when Polar is in the solar wind have also been used to corroborate these determinations. Statistical cross checks have been made between electron and ion measurements to verify that the densities are tracking one another. Cross checks are also made with other more absolute measures such as plasma line or spacecraft floating potential predictions. Finally, the spacecraft return current, calculated from electron measurements, were organized against determinations of the floating potential to illustrate that the data are well organized and that the prediction of the photoemission properties of the spacecraft are reasonable. These comparisons have been summarized in *Scudder et al.* [1999].

The Hydra instrument was launched in 1996 and after 11 years is still operational. The degradation in efficiency has been carefully monitored by comparing Hydra predicted densities, after all intracalibrations have been completed, with the predictions of the local plasma density from a floating potential density relation. That relationship was determined early in flight in regions like the magnetosheath where the return currents conditions and calibration curves were well documented. The degradation in photoemission is much less severe than the channeltron gain degradation, and very satisfactory renormalizations have been made by referencing the overall efficiency of each analyzer to that of the reference analyzer (12). Selecting the absolute detection efficiency usually brings the overall variation of the Hydra-determined plasma density into good agreement with that predicted from the spacecraft potential. For a recent example of this see *Scudder et al.* [2000].

4.4.5 Wind 3D Plasma

The Wind 3D Plasma experiment contained two electron (EESA-L, EESA-H) and two ion (PESA-L, PESA-H) plasma sensors covering the energy range from a few eV to 30 keV, and a set of solid-state detectors that extended the supra-thermal energy range to 400 keV for electrons and ~11 MeV for ions [*Lin et al.*, 1995]. The -L and -H refers to low

and high sensitivity analyzers, with both high sensitivity sensors having anti-coincidence scintillators to reduce background from penetrating radiation. Three of the ESAs used the same basic spherical top-hat design with $\Delta R/R = 0.075$ and inner hemisphere radius of R=3.75 cm. The fourth, EESA-H, had R=8 cm but the same $\Delta R/R = 0.075$ so that all sensors had the same basic energy resolution, analyzer energy constant, and angular resolution perpendicular to the planar FOV. The PESA-L sensor had a pinhole attenuator, which reduced the incident flux by a factor of 50, but maintained the same energy-angle response. Sensors had anode angular resolution that varied from 5.6° near the spin plane, to 11.2° at ∼45° from the spin plane, to 22.5° near the spin axis. Both low sensitivity sensors were half-analyzers with 180° FOVs whose center look direction direction was perpendicular to the spin axis. The high sensitivity sensors had 360° FOVs whose planes were rotated 90° from the low sensitivity FOVs. Electron and ion sensor pairs were mounted on short (0.5 m) booms on opposite sides of the spacecraft to reduce FOV obstructions and particle deflections due to spacecraft charging. All ESA sensors used MCP detectors.

The in-flight calibration effort for the Wind 3D Plasma experiment offered several challenges. The Wind spacecraft spends the majority of its orbit in the solar wind, which generally restricts the type of in-flight calibrations that are possible. The high solar wind flows ($\sim$400 km s^{-1}) result in both an extremely narrow ion beam distribution and anisotropy in the relatively cool (T_e ∼10 eV) electron distribution. Typical ion beam widths are near the analyzer resolution, have high count rates that require dead-time corrections, and have enough alpha content to require an algorithm that does not assume moments are dominated by protons. Although an occasional burst mode provides some 3-D data at the spin period (3s), generally data rate restrictions only allow moments calculated on board to be transmitted at this rate, limiting the ability to make ground based corrections to the data. Electrons are the most difficult to measure quantitatively since the combination of photo-electrons and variable spacecraft potential result in on-board moment calculations that are qualitative at best. 3-D count rate distributions are available at a lower cadence, typically once every 8, 16 or 32 spins. It is the 3-D data that allow the most accurate data corrections using in-flight calibration techniques described below. Generally only those calibrations that were required for science goals were attempted. Below we outline the various calibration efforts for each plasma sensor head.

One of the primary tasks of in-flight calibrations is to maintain an optimal bias voltage to the MCP detectors. The AMPTEK A111 preamplifiers had a fixed charge threshold level and precluded cycling the threshold level to determine the MCP's pulse height distributions. Instead the MCPs were stepped through a series of bias voltages with ∼50 V increments while the instrument count rate was monitored. The set of voltages started ∼100 V below the current MCP bias voltage and extended to ∼100 V above the current value. The sensor remained in its nominal energy sweep mode and a plateau in the average count rate was used to determine the optimal bias voltage. MCP bias changes were made a few times during the first four years as the MCPs were scrubbed. They have remained at these voltages for the remaining ∼10 years.

PESA-L is a solar wind sensor that uses a set of eight 5.625° anodes near the spin plane to measure the core H^+ and He^{2+} angular distributions. 64 energy sweeps per spin provide 5.625° spin plane resolution, which is about the analyzer intrinsic resolution. A 14 energy step sweep with dynamic range, $E_{\max}/E_{\min}$, of ∼10 is adjusted every spin so E_{min} is about 2/5 of the peak count rate in order to track the solar wind velocity to provide a high-energy-resolution measurement. Tracking is performed with software using computed moments.

A core 8×8 solid angles × 14 energies are used for moment calculations each spin period and a 5×5 solid angle × 14 energy snapshot (one spin) distribution is transmitted every eight spins. On-board moment calculations use the relative energy shift between H^+ and He^{2+} to separate the different particle moments. PESA-L complements the Wind SWE Faraday cup measurements (see Section 4.4.9) by providing much higher time resolution measurements of the solar wind core. Since SWE does not include detectors that change with age, and since it was carefully cross-calibrated with measurements of the plasma frequency, f_p, by the WAVES experiment (see Section 4.4.11), PESA-L used the SWE data to perform its in-flight absolute calibration. This allowed cross-calibration of plasma density over long periods, during times when dead-time corrections were negligible, and when f_p was not well measured. In-flight calibration checks of the analyzer energy constant showed a 2 % systematic difference in solar wind flow velocity between SWE and PESA-L. With no way of determining the absolute flow velocity and source of the error, PESA-L data analysis software used the laboratory determined analyzer energy constant. Without an isotropic particle distribution available for in-flight relative sensitivity calibrations, the PESA-L 5.625° anodes were assumed to have the identical response determined by laboratory calibrations. MCP energy efficiency was assumed flat, which is reasonable for a limited energy sweep range (typically 0.4–4.0 keV) and ∼2.3 kV pre-acceleration.

The primary in-flight calibration effort for PESA-L was the determination of electronic dead time. Due to the high solar wind fluxes, dead-time corrections are critical for quantitative measurements particularly during cold or dense solar wind conditions. The Wind 3D Plasma sensors used AMPTEK A111 preamplifiers that do not have well defined dead times. The A111 dead time depends upon the amplitude of both the initial and trailing charge pulse, with larger initial pulses requiring longer recovery times before a second pulse can be registered. Dead time correction therefore requires a complex average that depends upon the MCP pulse height distribution. Since the MCP pulse height distribution can droop during high count rates as microchannels recover, the dead time is also a function of count rate history. For corrections to 3-D arrays of count rate data, the average dead time was determined from density comparison with SWE and incorporated in the ground calculation programs that converted rate data to physical units. Such corrections are not possible for on-board moment computations, so a method was developed to correct the on-board ion moments for dead time effects. Since the peak ion count rate in an ideal analyzer in response to a drifting Maxwellian is proportional to $N_i v_d^4/v_{th}^3$, this quantity was used as a proxy for the rate in the dead time corrections, $N_{i,\mathrm{corr}} = (EFF \cdot N_i)/(1 - DT \cdot N_i v_d^4/v_{th}^3)$, where the ion number density, N_i, the solar wind velocity, v_d, and the ion thermal speed, v_{th}, are the moments calculated on board, and the *EFF* and *DT* are the absolute counting efficiency and dead time, respectively. *EFF* and *DT* are determined from fits between PESA-L and SWE densities. Variations in both *EFF* and *DT* are observed over the mission as MCPs aged or as bias voltages were changed indicating that the dead time was not exclusively a preamplifier dead time effect. Figure 4.24 shows a comparison of the uncorrected and corrected solar wind densities from PESA-L and the SWE density during a period where dead time corrections were important. The third panel shows the uncorrected temperature from 3DP and SWE. Note that dead time corrections can be most important during periods where the ions are cold, and not necessarily where the density is high, due to the $1/v_{th}^3$ in the peak count rate of a drifting Maxwellian.

PESA-H is a high sensitivity ion sensor for measuring the solar wind suprathermal tail and ions reflected at the Earth's bow shock. PESA-H has a 30 energy step sweep covering

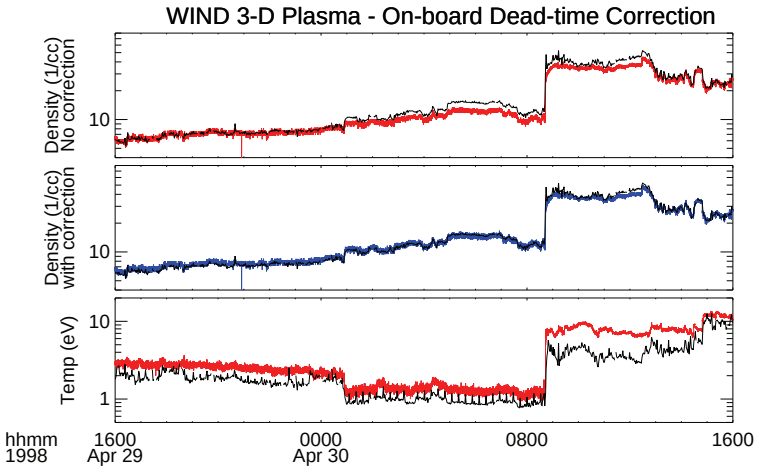

Figure 4.24: The figure demonstrates an effective method for dead-time correcting the on-board calculated density moments from the Wind 3D Plasma PESA-L sensor. The top panel shows uncorrected PESA-L density (red) and SWE determined density (black). The second panel illustrates that the dead-time corrected PESA-L density (blue) and SWE density (black) have good agreement. The bottom panel shows the ion temperature from PESA-L (red) and SWE (black). Since the peak count rate of a drifting Maxwellian is proportional to $N_i\, v_d^4/v_{th}^3$, this formula was used as a proxy for count rate in a dead-time correction algorithm that operated on the on-board calculated density moments. Note that the dead-time corrections are not the largest where the density is highest, but rather where the temperature is lowest.

$\sim$80 eV to $\sim$30 keV, 16 times a spin. 3-D distributions (typically 96 solid angles by 15 energies) averaged over 16 or 32 spins are its primary data product. The PESA-H sensor calibrations were primarily restricted to cross checks of the analyzer energy constant with PESA-L. Since PESA-H saturates in the solar wind, and since PESA-L only makes limited measurements in the solar wind direction, no in-flight cross-calibrations of sensitivity were made between them. PESA-H relies on laboratory calibration determinations. It may be possible to find periods during Wind perigee passes in the magnetosphere where PESA-H relative and absolute in-flight calibrations could be made, however no science objectives have driven this requirement. In-flight testing did drive one operational change in PESA-H. As discussed in Section 4.2.9, the sensor experienced high background counts in the equatorial anodes due to problems with "after-emission" caused by the high solar wind flux. To avoid this problem in the measured distribution, the sensor's energy sweep was limited to a 3 keV to 30 keV range when the sensor looked in the solar wind direction. Since the sensor had a 360° FOV, the truncated sweep was required twice a spin. However, this avoidance meant the sensor would not be able to cover the entire energy range when looking Earthward. To retain full energy coverage when looking Earthward, the energy sweep truncation was only applied once a spin and data taken from the sensor half-with after-emission were discarded.

The EESA-L sensor provides the solar wind electron plasma measurement on Wind. Its energy sweep from $\sim$6 eV to 1.3 keV covers the primary solar wind core and suprathermal

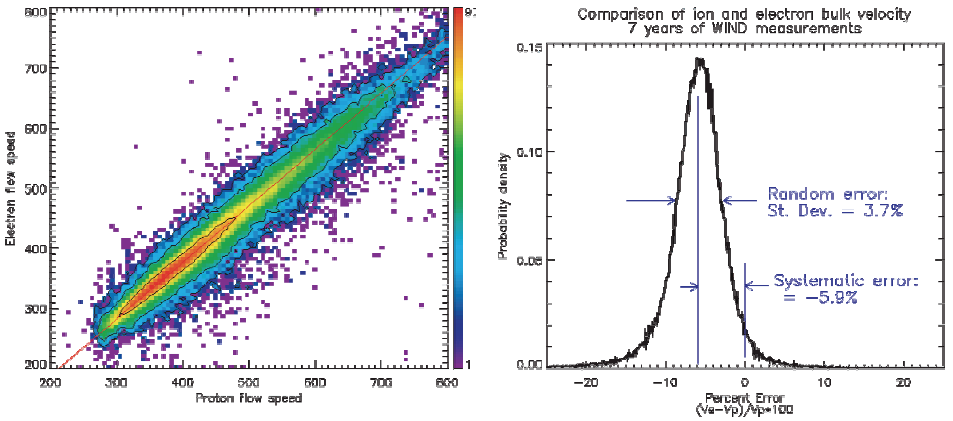

Figure 4.25: *Left:* a histogram of the Wind 3D Plasma electron velocity versus ion velocity; *Right:* a histogram of electron velocity errors. A ∼6 % systematic error was present that is likely due to errors in analyzer energy constants determined on the ground. Random errors had a standard deviation of only 3.7 %.

tails, as well as photo-electrons under typical conditions. On-board moment calculations provide spin period data, however, since these algorithms do not allow corrections for spacecraft potential, spin period data are qualitative at best. Relative anode sensitivity uses laboratory determined values to account for variations that are not geometrical. These are due primarily to double counting at the anode edges which makes the smaller anodes have a larger effective sensitivity. (Double counting occurs when the MCP charge cloud is split between two anodes, resulting in both preamplifiers registering counts.) The laboratory determined value of the analyzer energy constant was used. Comparison of EESA-L and PESA-L solar wind velocity (Figure 4.25) shows that a small (∼6 %) systematic shift is observed between these two measurements. Possible sources for this difference are errors in the analyzer energy constants, offset errors in the EESA sweep, particle deflections associated with spacecraft charging, or a systematic error introduced by the fitting routine described below. Neglecting this systematic error, the figure demonstrates that anisotropy in the measured electron distribution caused by the bulk flow is adequate to allow accurate velocity measurements even though the drift velocity of the solar wind is a small fraction of the electron thermal velocity. The MCP efficiency is assumed to be independent of electron energy, which is a reasonable approximation for a ∼0.4 kV pre-acceleration and electron energies of 0.4–1.7 keV at the front of the MCP. The absolute MCP efficiency was determined via cross-calibration with PESA-L and required a complex ground-based calculation algorithm to correct for spacecraft potential and eliminate photo-electrons.

The primary EESA-L in-flight calibration effort involved determining the spacecraft potential and any temperature-produced offsets in the HV sweep. A sweep mode was operated several times that allowed the inner hemisphere voltage to be driven negative. A dropout in the photo-electron flux signaled the value where inner hemisphere voltage crossed through zero, and therefore determined the sweep HV offset. Since the Wind spacecraft rarely experiences eclipse, its temperature is stable and the HV offset was assumed constant. Spacecraft potential determination on Wind was difficult given no direct

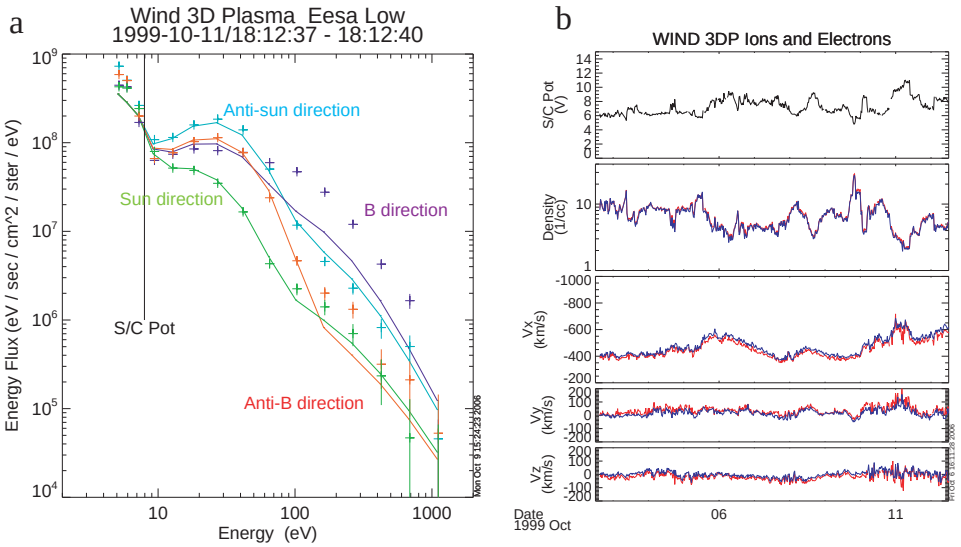

Figure 4.26: (a) The figure shows sample electron spectra (+ symbols) at four pitch angles along with the results of a fitting algorithm (solid curves) that determined the spacecraft potential from the break in the spectra between photo-electrons and plasma electrons. For details of the algorithm, see the text. The algorithm does not contain terms for solar wind strahl and therefore does not fit the field aligned suprathermal tail. (b) Figure is a time series comparison between the fitted electron moments (blue) and ion moments (red) indicating an accurate determination of spacecraft potential using this technique. The top panel shows the spacecraft potential determined from the fitting algorithm.

measurement from DC electric field probes. Since the electron density and temperature both impact the spacecraft potential, a fitting algorithm was developed that assumed the measured electrons could be fit to a combination of a drifting bi-Maxwellian core and suprathermal tail, plus a fixed photo-electron spectrum. For primarily radial electron trajectories, the spacecraft potential marks the boundary between photo-electrons generated from the spacecraft and the ambient plasma electrons. The photo-electron spectra were determined from measurements in the low density magnetotail lobe regions that extended out to ~60 eV. The fitting assumes the actual finite energy width of measurement bins as determined from folding the analyzer response with the change in sweep energy during a counter accumulation. Using the actual energy response was critical since the energy resolution was relatively coarse across the boundary between photo-electrons and plasma electrons. The fitting algorithm is primarily a minimization of the difference between the measured counts and functional fit with several parameters: spacecraft potential, N_e, v_d, $T_{e\parallel}$, $T_{e\perp}$, and optionally a suprathermal drifting Kappa or bi-Maxwellian. The fit is limited to energies below $\sim 3T_e$ and does not rely on any other sensor measurements. Excellent agreement between calculated electron and ion densities and flow velocities have provided confidence in the technique. Figure 4.26a shows an example spectra (+ symbols) along with results of the fitting algorithm (solid curves). The algorithm does not include terms to fit the solar wind strahl, and therefore has poor agreement at higher energies along the magnetic field (purple). In principle, additional parameters could be included to fit the strahl, but they are not required for accurate determination of the spacecraft potential and

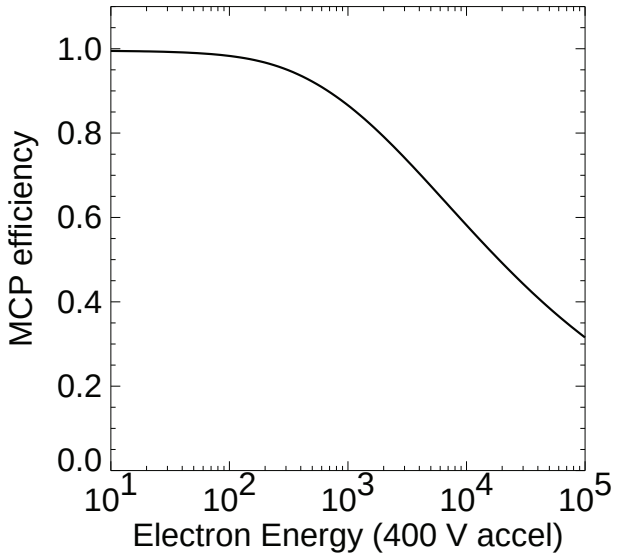

Figure 4.27: MCP energy dependent efficiency used to correct the Wind 3D Plasma electron measurements. The curve is based on published results by *Goruganthu and Wilson* [1984].

core moments. Figure 4.26b shows a time series comparison between the fitted electron moments and ion moments indicating an accurate determination of spacecraft potential using this technique. Without an accurate spacecraft potential, electron moments would be qualitative at best.

EESA-H is used to provide a higher sensitivity monitor of the solar wind electrons' suprathermal tail. Because of saturation problems at low energies, the EESA-H energy sweep extended from ∼100 eV to 30 keV. Its primary data product is a 3-D count array (88 solid angles × 30 energies). Ground calibration determined values of relative sensitivity and analyzer energy constant were used. The absolute sensitivity was determined by intercomparison with EESA-L over their common energy range. To reduce background noise problems, several of the anodes were not used in 3-D array accumulations due to noise from the edges of the MCPs. The primary in-flight calibration came from observations that the high energy EESA-H spectra did not align with the electron spectra determined from the solid-state detectors (SSDs). This was due to the assumption that the MCP counting efficiency was independent of electron energy. Since a determination of the actual energy dependent efficiency was not possible, an efficiency dependence was developed based on the published equations in *Goruganthu and Wilson* [1984]. Figure 4.27 shows the energy dependent efficiency curve used which assumed the 0.4 kV pre-acceleration. The estimated efficiency at 30 keV is about 45 % of the maximum at low energy resulting in a significant spectral shift. This correction reduced the spectral mismatch between EESA-H and the SSDs to about the measurement error as shown in Figure 4.28.

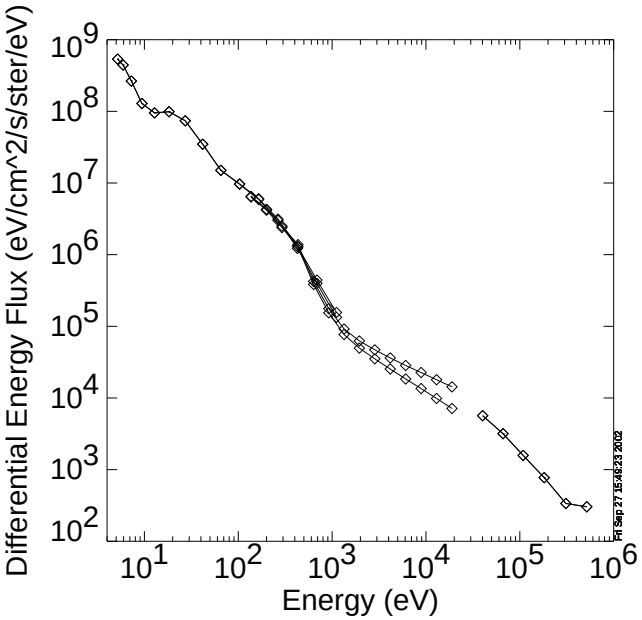

Figure 4.28: Wind 3D Plasma electron spectra determined by the EESA-L (6 eV to 1.3 keV), EESA-H (0.2 to 20 keV) and SSD (>40 keV) sensors. The two curves between 1 and 20 keV represent electron spectra assuming no MCP energy dependent efficiency (lower) and the energy dependent efficiency in Figure 4.27 (upper). Although at a given time spectral features could be present that would result in a break in the slope, it was found that the spectra were more continuous across this measurement boundary for the assumed efficiency in Figure 4.27.

4.4.6 Cluster CIS

In this section, various in-flight calibration techniques for the CIS/CODIF mass spectrometer instrument on Cluster are described. CODIF consists of a toroidal top-hat electrostatic analyzer combined with a carbon-foil time-of-flight velocity analyzer (Section 2.6.4). Ions and carbon foil electrons are detected with microchannel plates.

4.4.6.1 Absolute Efficiencies

The raw counters used for these measurements count any ion that enters the instrument. There is no a priori way to know the ion species. Thus the only way to determine the efficiencies for different ion species in-flight is to use time periods when a particular ion species dominates. Since the dominant ion in the magnetosphere is H^+, it is relatively easy to find time periods to use to determine the efficiencies for H^+. Over the polar cap there are time periods when the dominant population is a beam of O^+ ions. These time periods can be used to determine the O^+ efficiencies. Similarly, there are times during magnetic storms when O^+ dominates in some energy ranges.

As described in Section 4.3.2, the count rates of individual signals and coincidence signals are used to give an absolute measurement of the efficiencies of each signal. The individual count rates and coincidence rates are determined for time periods when one

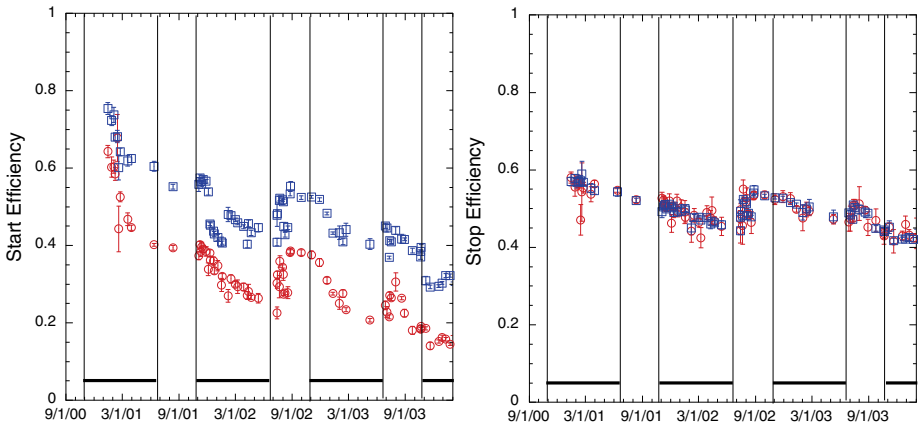

Figure 4.29: The CODIF event start and event stop identification efficiencies on Cluster spacecraft 1 as a function of time. Circles (red) are for protons at 1 keV and squares (blue) for protons at 11 keV. Most of the degradation occurred in the magnetosheath whose crossings are indicated by the bars on the bottom. Increases in efficiency are due to changes in MCP bias voltage.

ion species dominates and the distribution is relatively isotropic, so that the efficiency is representative of all positions in the instrument.

Figure 4.29 shows the change in the start and stop efficiencies for H^+ on spacecraft 1 (SC1). The circles are for ions at 1 keV, and the squares for ions at 11 keV. The overall change is about the same, independent of energy. Clearly, the start efficiency degraded significantly more than the stop efficiency. On the figure the vertical lines connected by the solid bars mark the time periods when the spacecraft is routinely entering the magnetosheath. The most significant degradation occurred during these times. The increases that are observed after these time periods are due to increases in the MCP voltage. The intense magnetosheath flux contributed significantly to the MCP degradation over time.

To determine the efficiency changes for O^+, we identified time periods when O^+ dominated. These were mainly periods when the spacecraft was over the polar cap and observed O^+ beams. The ions normally are observed in one energy step and one position on the MCP. Thus the rate data for that time period is used to give the O^+ efficiency for that energy and position. Then, using the relative efficiencies (as described in the next section), we can determine the O^+ efficiency for all the positions.

4.4.6.2 Relative Efficiencies

To determine the relative efficiencies of individual detector positions within an instrument, we identified time periods when the ion pitch angle distribution was expected to be gyrotropic (see Section 4.4.2.4). Since this was done using data that had been classified by composition, it was performed independently for each ion species, even when that species was not dominant. The only requirement was to have sufficient count rate for the particular ion species to get a statistically valid pitch angle distribution.

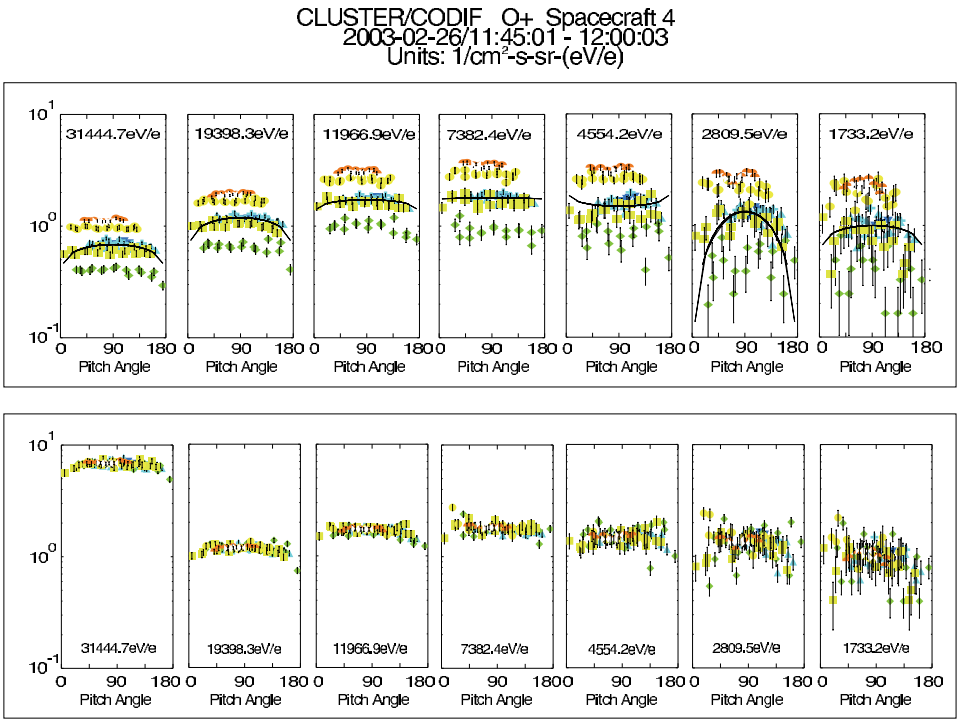

Figure 4.30: Relative efficiency determination for CODIF on Cluster 4. The panels in the top half show the pitch angle distribution for a range of energies before the new normalization factors were determined. The different colors and symbols indicate different anodes within the instrument. Also shown, with the black line, is the fit which was used for the normalization. The panels in the bottom half show the pitch angle distribution after the normalization for the same time period.

For Cluster we chose time periods in the inner magnetosphere, as close to perigee (4 R_E) as possible while avoiding regions where radiation belt contamination was a problem. For each identified time period, we calculated a fit to the pitch angle distribution for one detection position in the analyzer, which has good statistics and covered a range of pitch angles. The distribution was fit to the function: $f = A \sin^n \Theta$, where Θ is the pitch angle. Then, the same fit function was used to normalize the other detection positions, so that each position had the same value at 90° pitch angle as the original position. The resulting normalized distributions are visually inspected to assure that all positions now agree over the full pitch angle range. This method is similar to that used for the HIA anode calibrations and, like that method, works well when there is good overlap between the pitch angles measured at different detection positions in the analyzer.

Figure 4.30 shows this technique applied to O^+ for a time period in February 2003, when the relative efficiencies for S/C 4 had degraded at different rates. As the figure shows, there is good agreement between the different detection positions after the normalization.

4.4.6.3 Pressure Balance

Checking for pressure balance allows a final verification on the efficiencies and geometric factor. This was performed using observations in the magnetotail (when the spacecraft moves frequently from the magnetic field dominated lobe to the plasma dominated plasmasheet), in the cusp, and at the magnetopause. Checking pressure balance from year to year and during different phases of the mission validated the efficiency changes with time that we found from the other methods and identified an overall factor by which the flux needed be adjusted.

Figure 4.31 shows an example of a pressure balance check during a plasmasheet pass in July, 2001. In all cases, the increases and decreases in the plasma pressure were offset by decreases and increases in the magnetic pressure, so that the total pressure profile was relatively smooth throughout the time period, confirming the calibration of the CODIF instrument. In addition, the total pressures measured on three spacecraft were compared and found to be in good agreement.

4.4.6.4 Three-Spacecraft Check of Calibrations

To test the inter-calibration of the three Cluster spacecraft, we calculated and compared average ion moments from the 3-D distributions for time periods in the magnetotail. Figure 4.32 shows the comparison of daily averages of the proton density and velocity in the plasmasheet for the 2001 tail season. SC3 had one MCP on the high sensitivity side (4 out of 8 positions) with very low efficiencies, a factor of $\sim$100 less than the other 4 positions. As a result, the calibration for SC3, particularly for the velocity in the z direction, was difficult, and there were larger differences between the velocities measured on SC3 and the other spacecraft. The average densities agreed on the three spacecraft within 4 %. The mean velocity values in the x direction were 23.8, 31.4, and 27.8 km s^{-1}, for SC1, SC3, and SC4, respectively. The standard deviations of the differences in the daily values from SC1 were 21.5 km s^{-1} for SC3 and 8 km s^{-1} for SC4. The mean velocity values in y were 6.2, 3.7 and 6.7 km s^{-1}, with the standard deviation of the differences in the daily values of 14.5 km s^{-1} and 4 km s^{-1} for SC3 and SC4. The velocity in the z direction is the most difficult parameter, because it relies on having a very good calculation of the relative efficiencies of the different positions. It had the biggest offset between the three spacecraft, with average mean values of -21.7, -58.2, and 1.0 km s^{-1} for the three spacecraft. The standard deviation of the differences in the daily values (km s^{-1}) from SC1 was 20.5 for SC3 and 8.0 for SC4.

4.4.7 NOAA-POES

The Total Energy Detector system in the Space Environment Monitor on board the 3-axis stabilized NOAA POES operational satellites is designed to monitor the energy flux carried into the atmosphere by electrons and ions below 20 keV energy. The instrument set contains ESA plasma detectors of conventional design that view at 0° and 30° to the spacecraft vertical. There are locations along the orbit of these satellites where these two view directions are at the same angle with respect to the local magnetic field vector and permit an inter-comparison to be made between the instrument responses (providing the local particle fluxes are sufficiently large). The top panel in Figure 4.33 summarizes the

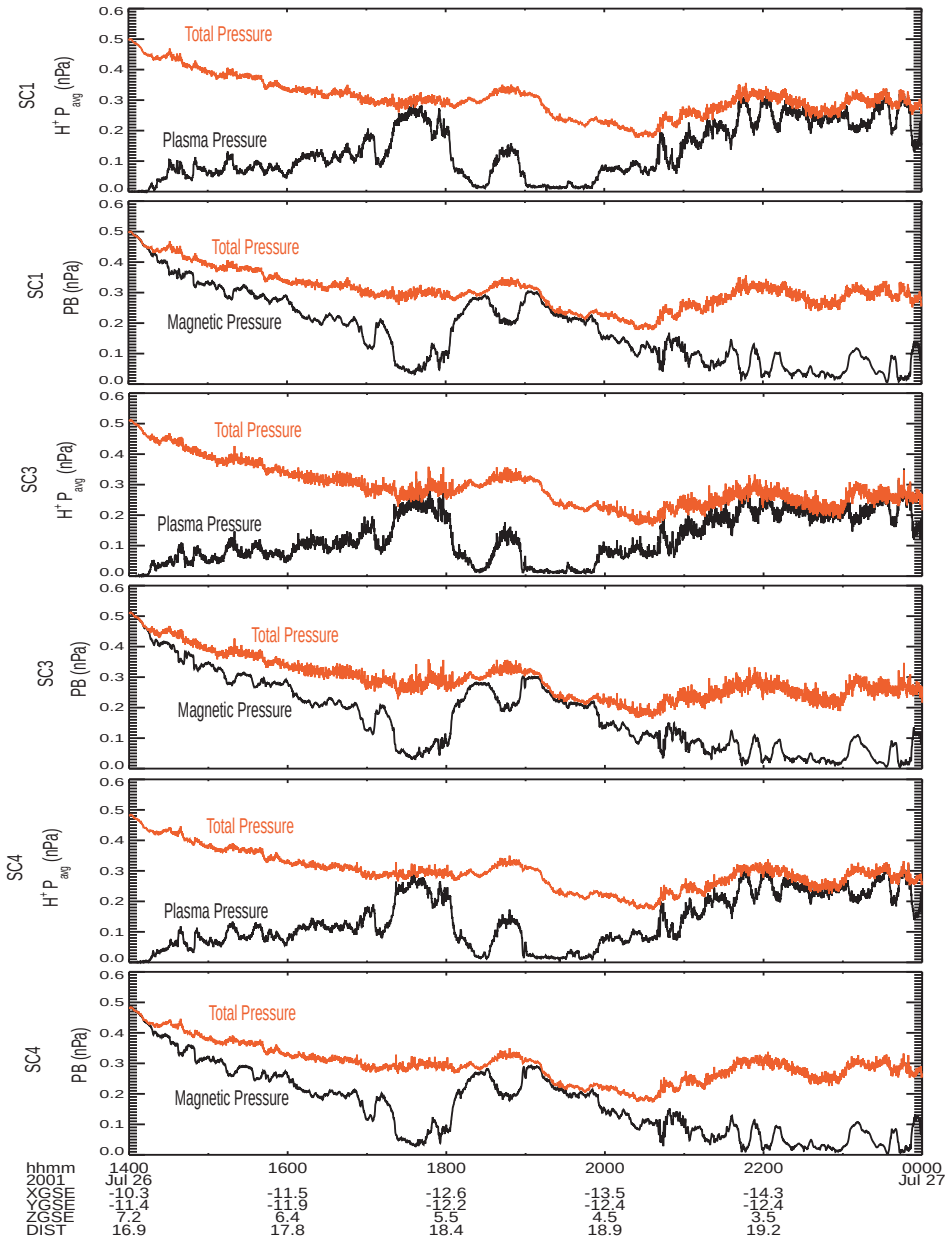

Figure 4.31: Pressure balance check for CODIF on Cluster 1, 3, and 4. The top panel shows (in red) the total pressure (magnetic plus plasma) and the plasma pressure (black), the second panel the total pressure (red) and the magnetic field pressure (black), both for spacecraft 1. The third and fourth panels show the same parameters for spacecraft 3, and the fifth and sixth show the same parameters for spacecraft 4.

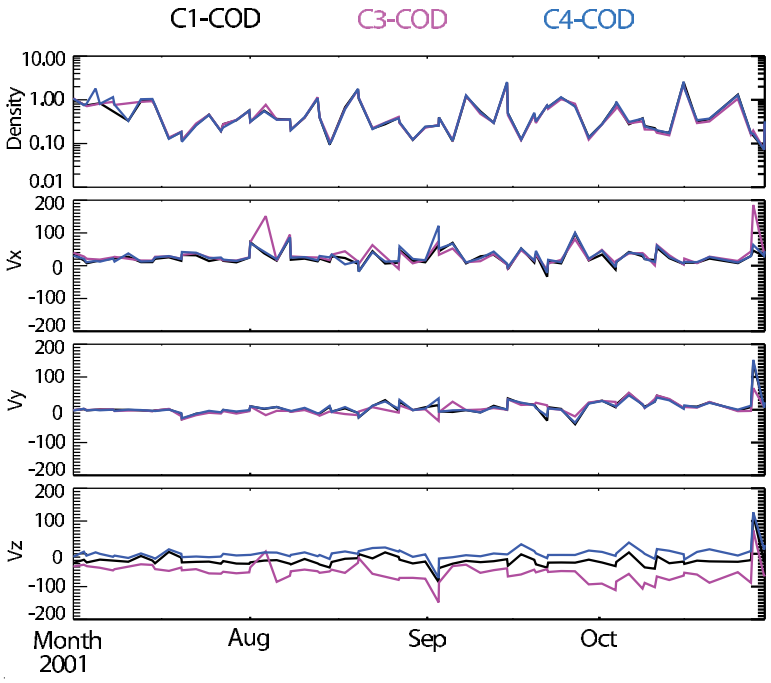

Figure 4.32: Comparison of daily averages of the proton density and velocity from CODIF on Cluster 1, 3, and 4 in the plasmasheet for the 2001 tail season.

results of numerous such comparisons between sensors on the NOAA-15 spacecraft. The integrated energy fluxes (both electrons and protons) over the energy range 1000–20000 eV agree to within 10 % between the sensor systems. The comparisons of electron energy fluxes integrated between 50–1000 eV agree less well between the 0° and 30° instruments (proton energy fluxes integrated over the low-energy range were too small to permit a comparison.) The lower panel in Figure 4.33 is a similar comparison between TED instruments on NOAA-16. Here the comparisons between the two sets of electron sensor systems is poorer, especially in the case of the two low-energy electron sensors where the zenith viewing instrument typically reports an integrated energy flux of less than 50 % of the off-zenith instrument in spite of observing identical electron populations. The exact reason for the disagreement is not known although the likely cause is too low a CEM bias voltage for the zenith-viewing instrument resulting in inadequate gain.

The fact that several NOAA POES satellites are in operation simultaneously provides the opportunity to obtain relative inter-calibrations between TED instruments on different spacecraft. The orbits of the NOAA polar orbiting satellites intersect at high latitudes and seemingly would provide many opportunities. However, it is rare that the intersection occurs both at the same time and in a region where auroral particle fluxes are large enough that a comparison between instruments on the two satellites is possible. Nevertheless, such occasions do occur and present the opportunity to perform direct comparisons between TED instruments. Figure 4.34 shows one such case where the NOAA-15 and NOAA-16 satellites intersected at nearly the same location (in invariant magnetic latitude

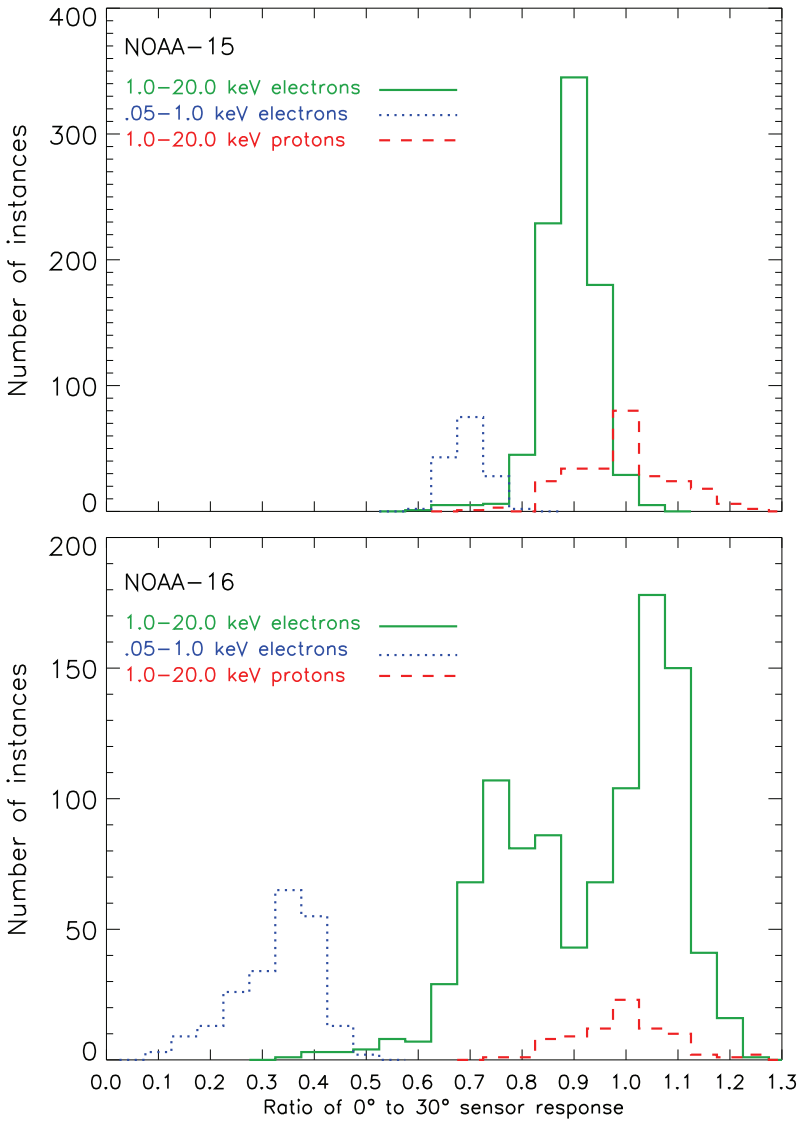

Figure 4.33: The distribution in the ratio of integrated particle energy flux as measured by the 0° and 30° TED detectors when both view particles at the same pitch angle. The data in the top panel (a) are for NOAA-15 while the bottom panel (b) are for NOAA-16. If the relative calibration of the detector systems were well known, the ratio should always be close to 1.0. Any departure of the mean ratio from 1.0 is a measure of the uncertainty in absolute calibration while a distribution of ratios around a mean value may reflect variations in Channeltron gain with time. The very low value of 0.35 for the NOAA-16, 0.5–1.0 keV electron sensor comparison is almost certainly because of inadequate Channeltron gain on the part of the 0° detector.

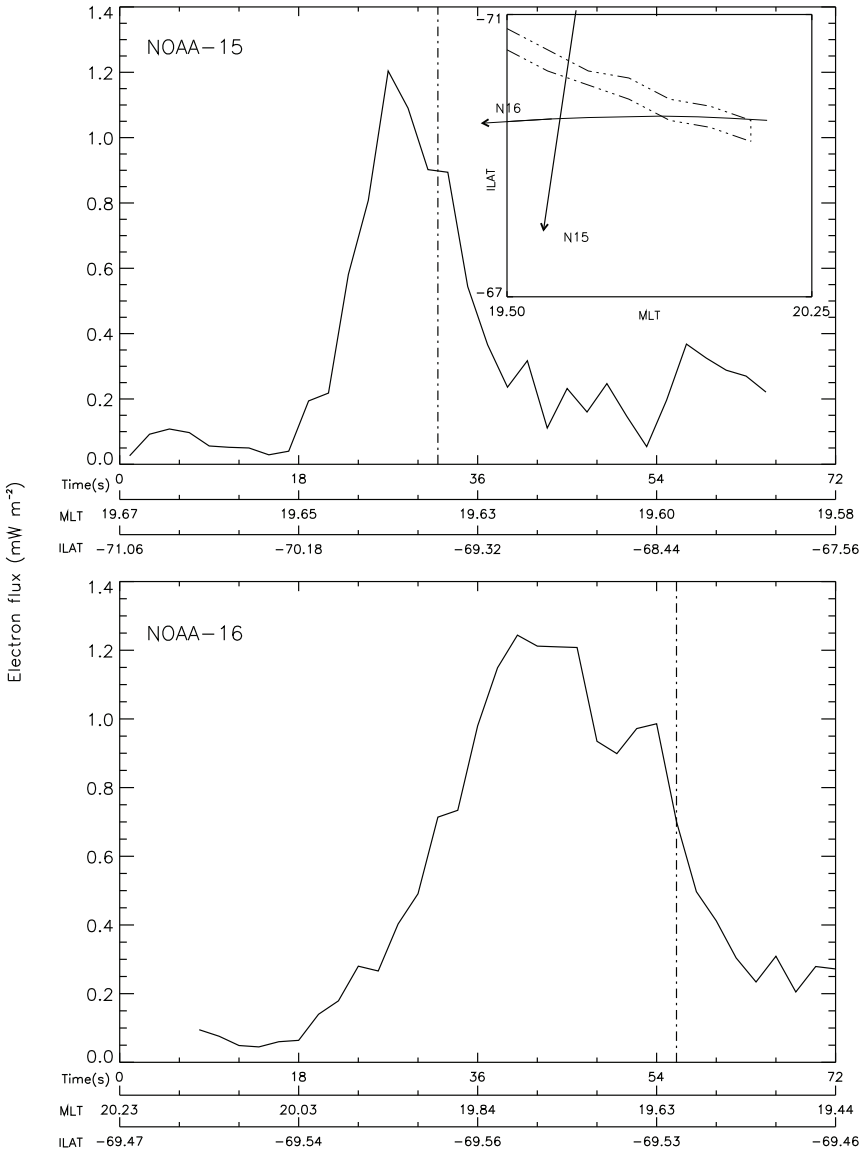

Figure 4.34: The integrated (50–20000 eV) electron energy fluxes observed by the NOAA-15 and NOAA-16 TED instruments plotted against time and location in magnetic coordinates for an inter-satellite conjunction near an auroral arc. The insert displays the tracks of the two satellites (solid lines) and the suspected orientation of the auroral precipitation feature. The two vertical dashed lines in each main panel mark the point in space where the two satellites intersected about 22 s apart in time. The agreement between the two TED sensor responses to this common auroral feature appears to be satisfactory.

and magnetic local time) within a few tens of km and within a few tens of seconds. In this case there was satisfactory agreement between the energy flux observations made on one satellite and those on the other.

However, because auroral phenomena are very dynamic in time and structured in space, comparisons of this sort are of marginal value in verifying the performance of one TED instrument against another. Cases of good agreement can be found but, equally often, are cases of poorer agreement. Those cases of poor agreement can easily be accounted for by the highly structured, in space and time, auroral particle precipitation together with the 2.0-second cadence of the TED energy flux measurements that translates to about 10 km motion across the magnetic field (referenced to 120 km.) The validity of such comparisons is further compromised because the satellite orbits at the intersection point are oblique to one another and do not perform identical transits through the auroral energy flux region.

In the case of the TED instrument, inter-satellite comparisons are also done using the estimated hemispheric power inputs that are calculated for each satellite's complete transit across the polar regions [*Fuller-Rowell and Evans*, 1987]. The history of such power estimates is available on the Internet (URL address `http://www.sec.noaa.gov/ftpdir/list/hpi/`.) The estimates of hemispheric power input rely on the TED energy flux measurements obtained during the transit through the polar region together with a set of global statistical patterns of auroral particle energy fluxes. The hemispheric power estimates are compromised during dynamic times when the actual global pattern of auroral energy input may depart significantly from any statistical pattern. However, the estimates have been shown to be, on the average, a reasonable indicator of the level of polar auroral activity.

The inter-satellite comparisons of hemispheric power use daily averages of the individual estimates obtained from each satellite's pass over the polar regions (about 30 estimates per satellite per day) rather than comparing individual estimates. Moreover, by combining daily averages over a period of months the influences introduced by the time varying and spatially structured aurora might be averaged out and a lowest order estimate of the overall sensitivity of one TED instrument compared to another is obtained. When this procedure was applied to TED observations from NOAA-15, NOAA-16, and NOAA-17, the results showed the overall NOAA-16 TED sensitivity to be 1.38 times that of NOAA-15 and the overall NOAA-17 TED sensitivity to be 1.04 that of NOAA-15. These values are in addition to the laboratory calibrated TED instrument sensitivities but are consistent with the variability in instrument sensitivities and rough estimates of the absolute uncertainties in instrument calibration.

Modest attempts have been made to obtain an in-flight absolute sensitivity calibration for the TED sensor systems. This is fraught with difficulty because there are no independent and accurate measurements of auroral particle energy fluxes that would represent a standard for comparison.

Comparisons between TED energy flux observations and ground-based observations of auroral forms have been made in the course of scientific studies. However, these comparisons yielded little more than confirmation that TED observations replicated the location and spatial extent of the aurora observed from the ground. It was not possible to make the quantitative comparison between auroral brightness and the energy fluxes observed from the satellite that might have constituted an independent verification of the TED energy flux calibrations.

Incoherent scatter radar measurements of ionospheric electron density profiles in the aurora can, in principle, be converted to altitude dependent ion production rates and thence to the parent auroral particle energy spectrum and integrated energy fluxes. Those results can be compared to the energy flux measurements made by the TED instrument during overflights of the radar facility. One such comparison [*Basu et al.*, 1987] between observations from Chatanika and observations made by an earlier TED instrument on the NOAA-6 satellite showed reasonable agreement. However, given uncertainties both in treating the radar data and in the TED observations, this comparison did not constitute an absolute verification of the TED calibration.

Finally, comparisons have been made between TED observations of auroral electron and proton energy flux into the atmosphere and observations from the IMAGE satellite of the resulting ultraviolet and far ultraviolet emissions from the atmosphere [*Hubert et al.*, 2002]. The TED auroral particle observations were used as input to model the intensity of emissions from the atmosphere and the modeled intensities compared to the IMAGE observations. The modeled emissions were in good agreement with those observed indicating that the TED energy flux observations were valid to within a factor of two. It should be pointed out, however, that this study was as much directed toward verifying the IMAGE calibrations as the TED calibration and was not a verification of either calibration against an absolute standard.

In summary, analysis of post-launch data from the TED instrument can verify that the analyzer systems are responding in the expected manner to auroral particle energy fluxes and not responding to spurious effects. Comparisons between sensor systems viewing different directions can be performed, and differences in sensor responses identified and corrected. Inter-satellite comparisons of TED observations are difficult to make on a case-by-case basis, but simultaneous data taken over long periods can be used to obtain comparisons between sensitivities of different instruments that are valid on a statistical basis. Currently, it is not possible to obtain an independent verification of the absolute sensitivity calibrations of the TED sensor systems because there is no absolute standard available for comparison.

4.4.8 FAST

In-flight calibrations of plasma detectors on low altitude satellites often pose a problem because the dominant plasma components are cold and therefore poorly resolved. For electrons, this problem is exacerbated by spacecraft photo-electrons and secondary electrons which appear at 90° pitch angles because of deflection by the strong geomagnetic field. Intense auroral electron fluxes also produce low-energy secondary electrons within the analyzers. If the satellite altitude is high enough to pass into the auroral acceleration region (generally $>$3000 km), comparisons can be made between plasma densities estimated from separate ion, electron and wave observations. This is possible because the auroral acceleration region accelerates the cold ionospheric ions to create beams that are easily resolved, and excludes cold ionospheric electrons leaving only the energized precipitating and trapped populations, with the admixture of spacecraft-produced photo and secondary electrons.

McFadden et al. [1999] made comparisons between ion and electron densities in the auroral acceleration region on 11 passes of the FAST satellite. FAST contains top-hat electrostatic analyzers that are oriented to continuously measure the 2-D pitch angle

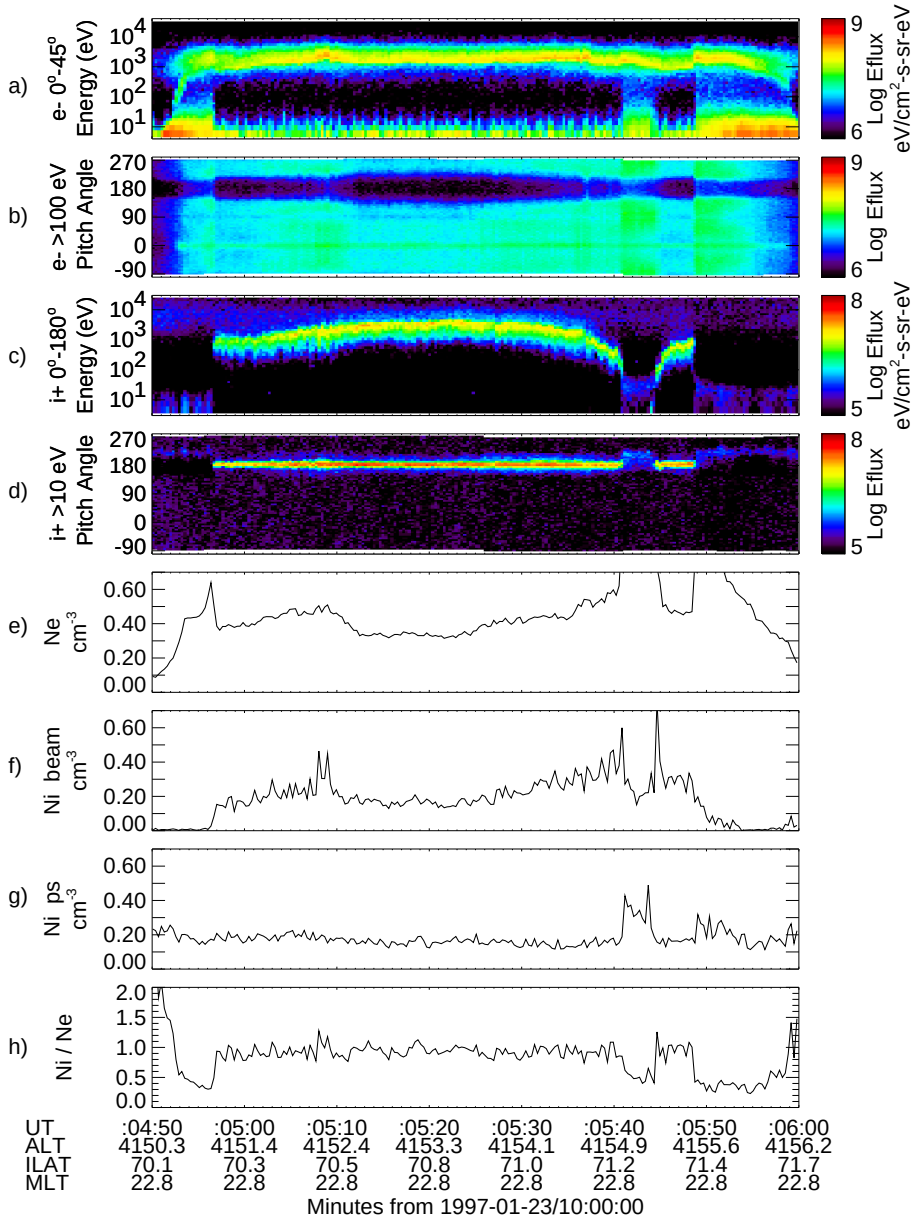

Figure 4.35: FAST ion and electron density comparison. Panels from top to bottom show: (a-d) energy and pitch angle spectrograms for electrons and ions; (e-g) density of electrons, beam ions, plasmasheet ions; (h) ion-electron density ratio. This last panel illustrates that the electron and ion densities agree to within ∼20 % inside the auroral acceleration region where no cold plasma is present. These comparisons provide a test of the relative calibrations between ion and electron sensors. From *McFadden et al.* [1999].

distributions. Particles are detected with microchannel plates. After an initial correction for relative efficiencies between ion and electron sensors determined on a single orbit, they were able to obtain N_e/N_i density ratios of $\sim 1.0 \pm 0.2$ for ten additional orbits. The calculations included corrections for composition and only included hot (>100 eV) electrons. Figure 4.35 shows an example of this density comparison. The measurements allowed them to conclude that a significant (>20 %) cold electron population was not present. The primary source of error in this analysis stems from a combination of 2-D measurements and large $\boldsymbol{E} \times \boldsymbol{B}$ drifts within electrostatic shocks. These drifts were large enough to shift the field-aligned ion beams off the magnetic field direction resulting in errors in the calculated ion beam density. A 3-D measurement could have avoided drift problems in ion density calculations, however, auroral ion beams often change faster than the spacecraft spin period so 3-D measurements would likely have been plagued by time aliasing.

In-flight cross-calibrations between wave inferred plasma density and measured plasma density can also be attempted in the auroral acceleration region. *Strangeway et al.* [1998] used fits of the parallel to perpendicular electric field ratio, $E_\parallel/E_\perp$, to determine the resonance cone angle of the Langmuir/whistler dispersion, assuming a cold fluid dispersion with a thermal correction. Density estimates using this wave technique were estimated to be not much better than a factor of 2. This is less accurate than preflight calculations of the plasma instrument sensitivity and therefore not adequate for calibration purposes but perhaps adequate for determining significant sensitivity losses due to degradation. Higher altitude satellites may be able to employ this or other wave techniques with more accuracy depending on the wave environment. However any plasma instruments observing particle fluxes on magnetic field lines that connect to the Earth are likely to encounter significant cold plasma that must be carefully accounted for.

Another cross-calibration test that can be performed on auroral data is a comparison between the inferred current from magnetic field deflections, and direct current measurements from auroral electron fluxes. Integral comparisons are found in *Carlson et al.* [1998, Figure 2] and *McFadden et al.* [1998a, Figure 1] and *McFadden et al.* [1998b, Figure 1]. Such comparisons are sensitive to many factors; for example, the orientation of the arc, the presence of electrons below the spectral peak, the low-energy electron cutoff of the sensor, and asymmetries in the spacecraft photo-electrons into the sensor. Since auroral arc orientation can vary dramatically during active periods, these comparisons are best made during quieter periods, when the spacecraft crosses normal to the oval, and within broad arc structures. The particle measurements in the upward current region can generally be improved by introducing a cutoff energy slightly below the spectral peak. This is because field-aligned electron fluxes below the spectral peak generally do not participate in the overall current. These electrons result from upwelling ionospheric electrons that are subsequently trapped and accelerated downward by EMIC waves [*McFadden et al.*, 1998b, and references therein], with no contribution to the net current. If electrons below the spectral peak are included in the accounting, the upgoing ionospheric electrons are often missed due to their low-energy while the energized downgoing ionospheric electrons are counted leading to an overestimate of the upward current. Introduction of this energy cutoff also avoids problems associated with asymmetries in the photoelectron and secondary electron populations measured by the spacecraft.

Good plasma sensor calibrations are also important for comparisons between precipitating electron and/or proton fluxes and the light detected by auroral imagers. Several

studies estimated the mean energy and flux of precipitating auroral particles from space using Polar-UVI and IMAGE-FUV [*Lummerzheim et al.*, 1997; *Chua et al.*, 2001; *Frey et al.*, 2001; *Gérard et al.*, 2001]. The comparison with simultaneous plasma measurements showed agreement within 20–50 %. This agreement is reasonably good given the many simplifications and assumptions of quantitative estimates from UV images. All optical inversion methods depend on models of the atmospheric composition, assumptions about the pitch angle distributions, energy spectra, and temporal stability of the precipitation. Furthermore, plasma measurements are always very localized investigations while the size of an image pixel can easily reach 100×100 km^2. As in the case of wave comparisons, comparisons between imager estimates and measured precipitating flux suggest that remote sensing is not adequate for plasma sensor calibrations but may be adequate for detecting significant plasma sensor degradation. Since stars easily can be used to provide continuous in-flight monitoring of imager sensitivity [*Frey et al.*, 2003], any significant deviation between inversion results from an imager and a plasma sensor would then point to changes in the plasma sensor sensitivity.

Techniques, similar to the IMAGE-FAST comparisons described above, were utilized by the UARS satellite but with the advantage that the remote sensing and local observations involved in the comparison were on the same satellite. The Particle Environment Monitor instrument suite on the UARS satellite included an electron spectrometer and an X-ray imager designed to observe bremsstrahlung X-rays produced from the atmosphere by precipitating auroral electrons [*Sharber et al.*, 1996]. The combination of these two instruments provided the opportunity to cross check one instrument's performance against the other. The energy spectrum of auroral electrons incident on the atmosphere could be constructed from the measurement of the X-ray energy spectrum. The imaging capability of the X-ray imager permitted the close connection between the *in situ* observations of precipitating auroral electrons and the location where the resultant X-ray production occurred, thus allowing a comparison to be made between the directly measured and reconstructed electron spectra. While this procedure did not provide for the absolute in-flight calibration of either of the two instruments, the general good agreement between measured and inferred energy spectra did provide confidence in the quality of both the particle and X-ray observations.

4.4.9 Wind Faraday Cups

The long-term stability of the electronic portion of the Faraday cups (FC) on the Wind satellites has been described earlier. There are two independent FC instruments on the Wind spacecraft, so a comparison of the solar wind ion parameters deduced separately by the two instruments is a possible way to detect an end-to-end variation in the relative calibration of either instrument over the course of the mission. Figure 4.36 shows histograms of the ratio of the proton number densities determined through a moment analysis of the observations by each FC. The red curves are a best fit of a Gaussian distribution to the histograms. Each panel has the year, the number of spectra that went into the histogram, the center of the best-fit Gaussian, and the width of the distribution. On average, the two instruments agree to one part in a thousand, with only very minor variations of the center of the distribution around a ratio of 1.0, or in the width of the distributions over a period of six years.

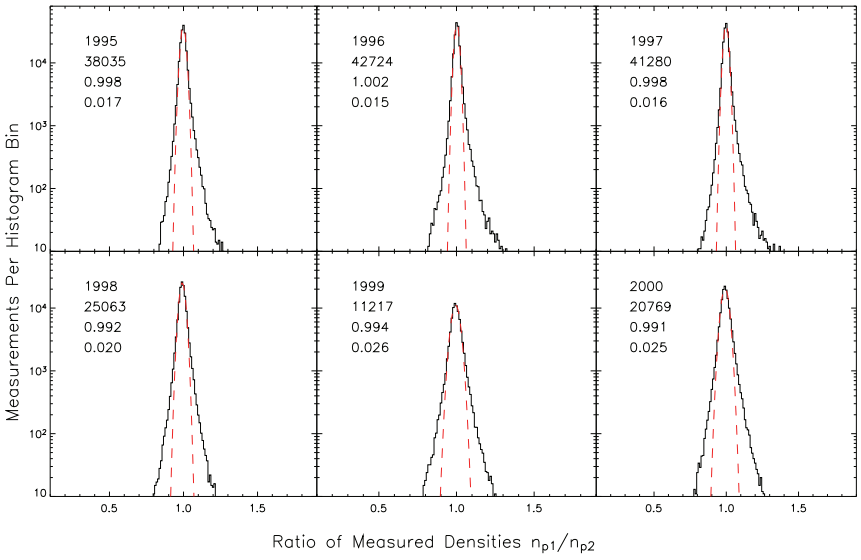

Figure 4.36: Histograms of the ratios of the proton number densities determined independently by the two Faraday cup instruments on the Wind spacecraft over a six-year period from 1995–2000. Each of the six panels is the data for one year. The dashed red lines are the best-fit Gaussian distributions to each year of data. The column of numbers in each panel are: the year, the number of measurements in the histogram, the center of the Gaussian, and the standard deviation.

4.4.9.1 SWE/FC and Waves

Absolute calibrations of the FCs on Wind have also been performed through comparisons with wave measurements. This study uses another instrument on the Wind spacecraft that measures the total electron number density in a completely independent manner. The Thermal Noise Receiver (TNR) instrument portion of the WAVES experiment measures the power spectra of electromagnetic fluctuations at a high cadence of 0.2–4.5 seconds in the frequency range from $4-300$ kHz [*Bougeret et al.*, 1995]. The solar wind plasma fluctuates at and above the electron plasma frequency $\omega_p^2 = n_e q^2/m_e\epsilon_o$, a quantity which is only a function of the total electron number density n_e and which varies from $50-300$ kHz in typical solar wind conditions. A neural network identifies the plasma frequency from a single TNR power spectrum and determines the electron number density. An extensive comparison of Ulysses/SWOOPS plasma data and Ulysses/URAP wave data using this technique has been presented by *Issautier et al.* [2001] for in-ecliptic and polar solar wind conditions.

In this section we compare a predicted value for the electron number density n_e based on the FC observed proton n_p and alpha n_α number densities with the TNR measurements. Since hydrogen and helium are fully ionized in the solar wind, the total electron number density due to protons and alphas is $n_p + 2n_\alpha$. However, we need to take into account the contribution of other ion species in the solar wind. Approximately 0.1–0.2 % of the

solar wind by number density is composed of heavy ions like oxygen and iron. While these heavy ions are rare, the typical charge states observed are large, for example O^{+7} and Fe^{+10}, so a small heavy ion abundance results in a contribution to n_e of ∼1 %. A detailed study by *Kasper et al.* [2006] showed heavy ion contributions to n_e ranged from 0.8 to 1.5 % depending upon the source (inter-stream or coronal hole). If n_e is the total electron number density measured by TNR, and all of the measurements were exact, then the fraction F_m of n_e due to heavy ions would be,

$$F_m \equiv 1 - \frac{n_p + 2n_\alpha}{n_e} \tag{4.14}$$

However, even after taking into account the heavy ions, *Kasper et al.* [2006] found that systematic errors resulted in errors to F_m of ∼4.7 %.

The mean value of F_m over the entire selected data set was 5.9 %, with a standard deviation of 5.1 %. The standard deviation is in agreement with the observations of *Maksimovic et al.* [1995], although $F_m = 5.9$ % is larger than was reported in that same study. That difference can be attributed to a refined analysis of the TNR data [Maksimovic, private communication, 2002] and to the use of proton number densities derived from a bi-Maxwellian analysis which yields results about 1 % smaller than the key-parameter number densities which were used in the 1995 study.

The width of the distribution of F_m over the mission was identified in part as being due to dependencies on time and on solar wind speed. The determination of the average value of F_m as a function of speed and year, and the estimate of the natural variation of the heavy ion component, are detailed in Figure 4.37. The center of the F_m distribution is plotted as a function of speed for each of the years from 1995–2000. Measurements in the same speed window have been offset horizontally by several km s^{-1} to avoid confusion. The two dashed lines indicate the estimated range of F_m. There are variations in F_m with speed which should be compared with more detailed predictions.

In summary, a combination of the estimates of F_m, the TNR electron measurements, and the SWE/FC proton and alpha number densities agree to within ∼4.7 %. Similar agreements were reported for Ulysses for the velocity and the electron core temperature [*Issautier et al.*, 2001]. The widths of the F_m distributions are consistent with the derived uncertainties in the proton and alpha number densities being less that 1 %. Furthermore the agreement between F_m and theory is consistent with the Wind Faraday cups having correct and stable density calibrations within a few percent of the absolute values.

4.4.9.2 SWE/FC and MFI

To identify the uncertainty in proton and alpha velocity measurements, we compare the alpha-proton differential flow vector, $\Delta \boldsymbol{V}_{\alpha p}$,

$$\Delta \boldsymbol{V}_{\alpha p} \equiv \boldsymbol{V}_\alpha - \boldsymbol{V}_p \tag{4.15}$$

with the direction of the ambient magnetic field $\boldsymbol{B}$ measured by the Magnetic Field Investigation (MFI) on Wind. The FC on Wind is able to separately determine the proton and alpha velocities using the procedures outlined in *Aellig et al.* [2001]. In order for a differential flow between the two species to be stable, the flow must be parallel or anti-

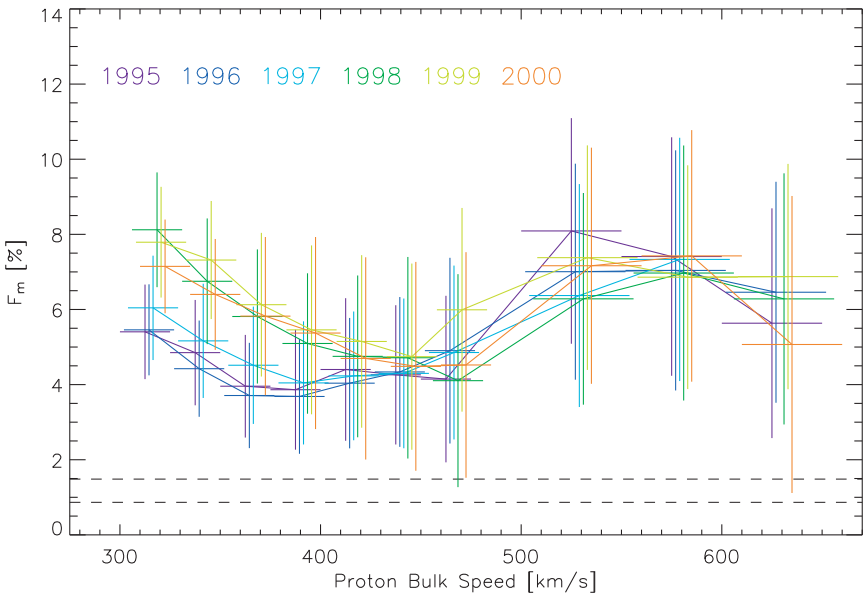

Figure 4.37: Center of F_m distributions and best-fit Gaussian widths (the vertical error bars) as a function of speed and year. Dashed lines indicate estimates of the expected contribution of heavy ions to the total electron number density. Modified from *Kasper et al.* [2006].

parallel to the field. Defining the angle between the differential flow and the magnetic field as,

$$\Delta\theta \equiv \arccos\left(\frac{\Delta \boldsymbol{V}_{\alpha p} \cdot \boldsymbol{B}}{|\Delta \boldsymbol{V}_{\alpha p}||\boldsymbol{B}|}\right) \tag{4.16}$$

we look at the range in θ seen as a function of the magnitude of the differential flow. As long as the individual measurements of $\boldsymbol{V}_\alpha$ and $\boldsymbol{V}_p$ are sufficiently accurate, $\Delta\theta$ will be close to either 0° or 180°. We expect that for sufficiently small values of $\Delta \boldsymbol{V}_{\alpha p}$ the direction of the differential flow will become uncertain and the range of $\Delta\theta$ will grow.

The results of this study are shown in Figure 4.38, which is a two-dimensional histogram of the measured values of cos $\Delta\theta$ as a function of the ratio of the differential flow to proton bulk speed, $|\Delta \boldsymbol{V}_{\alpha p}|/V_p$. For large values of $|\Delta \boldsymbol{V}_{\alpha p}|/V_p$, the flow vector is aligned to within 2° of the magnetic field. For $|\Delta \boldsymbol{V}_{\alpha p}|/V_p \lesssim 1.5\,\%$, the spread in $\Delta\theta$ begins to increase as expected, and in the range of $0.5 - 1.4\,\%$ the distribution in $\Delta\theta$ becomes isotropic. If the uncertainty in $\Delta \boldsymbol{V}_{\alpha p}$ arises equally from the hydrogen and the helium velocity measurement, then this result implies that the uncertainty in the ion velocities is between 0.5 and 0.7 %.

4.4.9.3 CELIAS/MTOF Proton Monitor with SWE/FC

The proton monitor, (PM), a small subsensor of the CELIAS instrument on SOHO was designed to measure solar wind plasma parameters to assist the data analysis of the

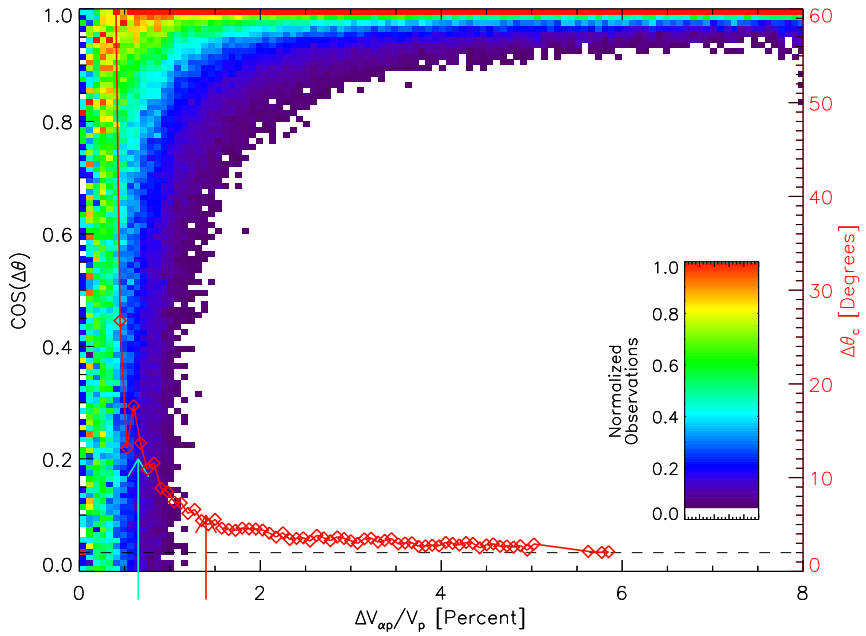

Figure 4.38: Determination of the uncertainty in hydrogen and helium velocity measurements by comparing the direction of the differential flow vector and the magnetic field. The colored squares are a two-dimensional histogram of the distribution of the measured values of cos $\Delta\theta$ as a function of the ratio of differential flow to proton bulk speed, $|\Delta \boldsymbol{V}_{\alpha p}|/V_p$. The diamonds are the average value of $\Delta\theta$ as a function of $|\Delta \boldsymbol{V}_{\alpha p}|/V_p$. Since the differential flow should only be parallel to the magnetic field, and therefore cos $\delta\theta$ should equal 1, the plot demonstrates accurate determination of both proton and alpha flow velocities. However, when the differential flow is less than $\sim$1 % of V_p, accurate comparisons are not possible.

other CELIAS sensors [*Ipavich et al.*, 1998]. Two methods have been used to derive solar wind speed, kinetic temperature, density, and out-of-ecliptic angle from the PM measurements. One method involved the calculation of many synthetic spectra. From the spectra that agreed best with a measurement the four solar wind parameters that determined the spectra were taken. The other method used was a moment analysis to derive the solar wind parameters. To decide which method was best, the solar wind parameters were compared to Wind/SWE measurements, considering the different locations of the two spacecraft [*Ipavich et al.*, 1998]. It turned out that both methods had advantages, depending on investigated parameter, thus in the final analysis of PM data a mixture of both methods was employed. Furthermore, the SWE data were used to refine the PM data analysis so that data derived from the PM sensor are calibrated to give absolute values with modest error bars. In a later study comparing many more measurements from PM and SWE, the same conclusion was derived [*Coplan et al.*, 2001].

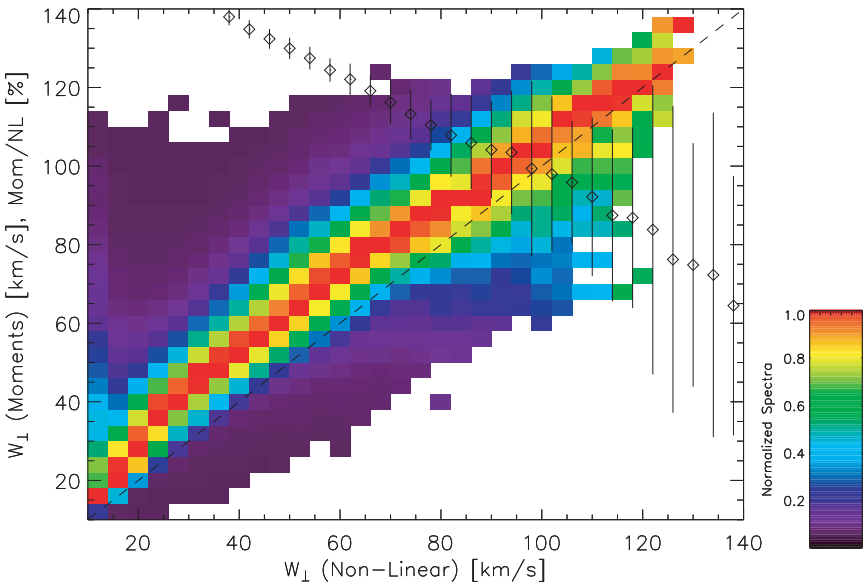

Figure 4.39: Comparison of moment and non-linear calculations of the perpendicular thermal speeds using Wind Faraday cup observations. Colored bins indicate the normalized distribution of the observations; compare with the dashed line indicating equality. Diamonds indicate 100 times the average ratio as a function of speed.

4.4.9.4 Moment versus Non-Linear Analysis Methods

Each of the more than two million ion spectra measured by the Faraday cup instruments on the Wind spacecraft up to 2003 has been analyzed using both a preferred non-linear fitting method and the method of moments. Velocities and number densities agreed to within one percent. The largest differences are in the thermal speeds. Two-dimensional histograms of the distribution of temperatures determined from moments versus non-linear methods are shown in Figure 4.39.

Although it was found that the two methods generally agree, the moment-thermal-speeds are generally slightly larger. In addition, a speed-dependent trend was identified in the average ratio of the two thermal speeds. This trend was investigated further through the use of a series of Monte Carlo simulations of solar wind spectra and Faraday cup measurements. Simulations of solar wind ions were made and the resulting moment-thermal-speeds and non-linear-thermal-speeds compared. The initial simulation was based solely on the contribution of protons to the total signal produced in the Faraday cup instruments. At large thermal speeds the moment-thermal-speeds were smaller than the non-linear-thermal-speeds, as observed in the data. It is thought that this is because at large thermal speeds the instrument would not see the entire distribution, and as a result the second moment would be underestimated.

In a more complex simulation of FC ion spectra, alpha particles were allowed to stream along field lines, as is commonly observed at 1 AU. This result, shown by the curves in Figure 4.40, is in good agreement with the observed ratios. The diamonds are the observed

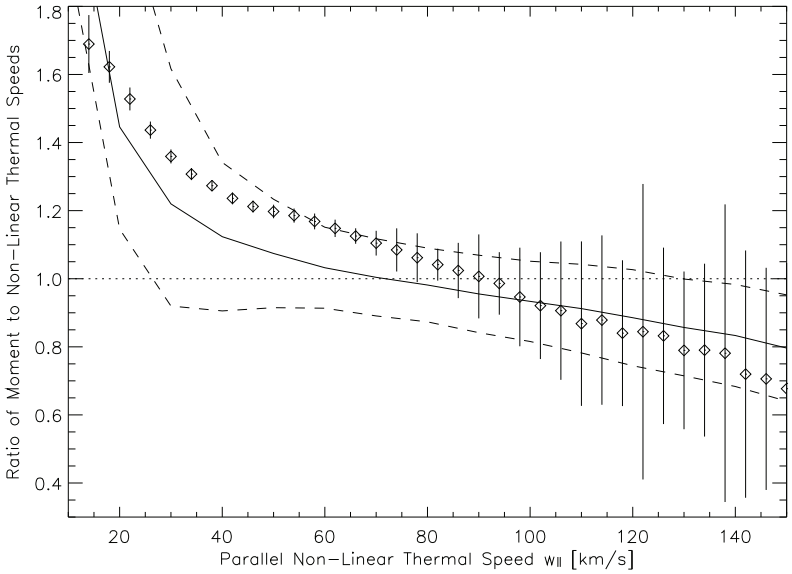

Figure 4.40: Comparison of the observed variation (diamonds) of the ratio of moment-thermal-speed to non-linear-thermal-speed calculations with a Monte Carlo simulation of that ratio, as a function of thermal speed. The center line is the average value of the ratio determined from the Monte Carlo simulation, and the upper and lower dashed lines indicate the one-sigma width to the distribution of simulated ratios.

variation of the ratio of moment to non-linear thermal speeds. We can conclude for the Faraday cups that the two major sources of discrepancies are 1) not measuring the entire distribution at large thermal speeds and 2) contamination from alpha particles at small thermal speeds.

4.4.10 In-Flight Testing in Special Circumstances

There are several cases where an instrument team took advantage of special circumstances that arose during a mission to conduct additional testing and verification of the instrument performance. One of the prime objectives of the Deep Space 1 mission was to test the ion propulsion technology. The spacecraft included a comprehensive plasma instrument, PEPE (Plasma Experiment for Planetary Exploration) to monitor the local plasma environment during the mission. Resource limitations prevented a complete ground calibration of PEPE and analysis of in-flight data was required to establish instrument performance [*Young et al.*, 2000]. However, after launch solar wind bulk velocities, densities, and temperatures computed from the PEPE observations were compared to similar parameters obtained from the well-calibrated SWE on Wind when the two spacecraft were within 10^6 km of one another. The comparisons between the two agreed to within 10 %. The time-of-flight portion of the PEPE instrument also responded as expected to the ion propulsion

system (IPS) propellant Xe^+ and to Mo^+ that sputtered from the IPS grid structures during IPS operation.

In order to provide gravity assist to the orbit, the Cassini spacecraft performed an Earth swing-by in August 1999. This provided the opportunity to compare plasma observations by the Cassini Plasma Spectrometer (CAPS) and energetic particle observations by the Low-Energy Magnetospheric Measurement System (LEMMS) with the relatively well characterized plasma and particle environment in Earth's magnetosphere [*Rymer et al.*, 2001; *Lagg et al.*, 2001]. Unfortunately, the encounter occurred at a time of high magnetospheric activity with Earth's magnetosphere in a dynamic state that precluded detailed comparisons between the instrument observations and models based upon a quiescent magnetosphere. However, the Cassini instrumentation did respond as expected to crossing various regions of Earth's magnetosphere (e.g. the bow shock, the magnetopause, low latitude boundary layer, tail lobe, plasmapause, and radiation belts) that qualitatively confirmed a proper instrument performance.

The Galileo spacecraft performed Earth swing-byes in December 1990 and in December 1992. On both occasions energetic proton observations by a LEMMS instrument as the satellite rapidly transited through Earth's radiation belts were converted to phase space densities as a function of the particle's magnetic moment and L-value [*Alinejad and Armstrong*, 1997]. Those results were compared to the AP8 radiation belt model with good agreement and so verified the performance of the LEMMS instrument and of the analysis procedures that yielded the phase space densities.

4.4.11 Langmuir Probes

In-flight relative and absolute calibrations of Langmuir probes (LPs) operated at high plasma densities may be established either by inter-comparisons with other instruments on the same spacecraft or by comparisons with simultaneous ground based observations. As mentioned earlier, comparisons between Langmuir probes on the same spacecraft not only expose degradation or problems, but those comparisons can also provide confidence in the measurements. In the late 1960s, multiple long-wire probes were flown on the same rocket to determine if the type of metal coating on the collector had any affect upon the T_e measurements [*Brace et al.*, 1971]. They found good agreement in the T_e measurements made by long-wire probes made of different metals or having different surface coatings. Comparisons among the measurements by different types of plasma instruments on the same satellites offered other insights into the validity of the various techniques. *Donley et al.* [1969] found good agreement among the measurements made by the cylindrical and planar LPs and the planar retarding potential analyzers on the Explorer 31 satellite. *Brace and Findley* [1969] found excellent agreement when comparing measurements from identical Langmuir probes on satellites with distinctly different physical configurations (Explorer-31 and Alouette-2) while they were orbiting in close proximity. *Miller et al.* [1984] also found very good agreement between the measurements of N_e, N_i, and T_e made by the Langmuir probe and the retarding potential analyzer on the PVO spacecraft.

Comparisons between space-borne and ground observations provide another method of establishing probe calibration. In 1968, two rockets were launched near the Arecibo radar facility in Puerto Rico to allow comparisons of LP and incoherent scatter measurements. *Brace et al.* [1969] reported that the daytime T_e measurements were in excellent agreement with the radar measurements, but the probe temperatures were slightly higher on the

nighttime flight. The T_e measurements by a platinum and a stainless steel probe on the nighttime flight disagreed by 10 %; a difference that was not present in the daytime measurements. The inherently large surface patchiness of the stainless steel probe may have led to the slightly higher values of T_e from that probe. More extensive incoherent radar and LP comparisons were reported by *McClure et al.* [1973] based on overflights of OGO-6. The long-wire LP measurements from OGO-6 yielded T_e values about 15 % higher than the radar measurements [*McClure et al.*, 1973]. Much better agreement was reported by *Benson et al.* [1977], who compared AE-C short probe measurements with those made simultaneously by the Millstone Hill, Chatanika, St. Santin, and Arecibo radars. The single disagreement was at Millstone Hill where the radar T_e measurements were lower than the probe measurements by an average of 11 %. These comparisons were valuable because they uncovered a systematic difference between the radar measurements from Millstone and the other locations. The generally better T_e agreement between the radars and the short probes suggests that the accuracy of the earlier long probe measurements may have suffered from a combination of surface patchiness and geomagnetically induced potentials, both of which cause energy smearing of the electron retardation regions at very low T_e. These effects are described in Section 2.3. While these comparisons among *in situ* and remote measurements have demonstrated the validity of the LP technique in a wide variety of space applications, they do not obviate the need to avoid implementation errors in any new mission.

4.5 In-Flight Relative and Absolute Calibration for Energetic Particles

Instruments designed to measure energetic particles encompass a number of different designs. Among these are simple solid-state detectors directly exposed to space or located under an energy degrader or absorber, multiple element solid-state detector systems capable of identifying both particle energy and mass, Cherenkov detector systems for detecting very high-energy particles and scintillation detector systems. A combination of detector techniques may be used in the same instrument to suppress background (anti-coincidence guard scintillators, Cherenkov detectors together with solid-state detector telescopes for particle species separations, etc.). In all cases both relative and absolute calibration of such detector systems must utilize either known properties of the natural radiation environment or radioactive sources in the instrument. This section describes several such techniques that can be used to perform such in-flight calibrations.

Cosmic rays provide an opportunity to perform an absolute flux calibration for instruments sensitive to high-energy protons. At high altitudes, geosynchronous and above, the cosmic ray flux is isotropic. Thus it is possible to calibrate both dosimeters, with a 4π sr field of view, or telescopes with a narrow field of view using natural cosmic rays.

Cosmic rays consist of 83 % protons, 13 % α-particles, 1 % heavy nuclei and 3 % electrons. At geosynchronous altitude, the Earth's magnetic field is sufficiently weak that it no longer provides an effective barrier to cosmic rays with energies above 87 MeV [*Stassinoupoulos*, 1989]. Thus the incident proton spectrum ranges in energy from about 100 MeV to tens of GeV.

Energy loss of high-energy protons varies slowly with kinetic energy. At 100 MeV the energy loss is 5.8 MeV g^{-1} cm^{-2} and it decreases slowly to the minimum ionizing value

of 2 MeV g^{-1} cm^{-2} at 1 GeV and stays at this value at higher energies. Consequently any high-energy proton detector will respond to cosmic rays. In addition, some high-energy electron detectors that depend on energy loss measurements will also respond to very high-energy protons because their energy loss is also at the minimum ionizing value of 2 MeV g^{-1} cm^{-2}.

Cosmic ray intensity varies inversely with solar activity reaching 4 protons cm^{-2} s^{-1} at solar minimum and decreasing to 2 protons cm^{-2} s^{-1} at solar maximum. Since the solar cycle variation can be modeled [*Smart and Shea*, 1985], the actual, isotropic flux can be determined to about 10–20 %. Even without the solar cycle correction, the flux value may be set to an intermediate value of 3 protons cm^{-2} s^{-1}, with an error of not more than 33 %.

Proton instruments on high altitude spacecraft can make measurements of cosmic ray count rate and, using the known cosmic ray flux, convert the count rates to absolute flux response. This procedure can be used to perform an end-to-end check of the instrument response as well as to track that response with time. This technique can only be used when the high-energy proton population from sources other than cosmic rays is low, a condition met at geosynchronous altitudes except during solar proton events. This technique may also be used at low Earth orbits with data collected when the spacecraft is out of the inner belt, including the South Atlantic Anomaly, and not in the horns of the outer belt. Be aware that the effect of the Earth shielding the spacecraft must be considered for spacecraft in low-Earth orbits.

Lastly we point out that in-flight determination of energy degradation due to changes in dead layer and lattice defects, as described in Section 4.3.3, is rather difficult. This is primarily a problem for ion detectors whose energy range may extend down to <30 keV. The simplest solution may be to include a separate calibration detector which remains shielded from exposure during most of the mission and whose aperture can be opened periodically to cross-calibrate the primary sensor. When resources are available, this will provide the most reliable in-flight absolute and relative calibration for the primary sensor.

4.5.1 Absolute Energy Response Calibration

The measurement of energy response of a detector provides an end-to-end measurement of the gain of the system (detector and electronics). In some cases, the absolute energy response of a detector can be measured in-flight by a radiation source. The source can be either mounted in fixed position, so as to illuminate the sensor at all times, or be placed on a movable arm so that its radiation strikes the detector only during calibration periods. The disadvantage of the first method is that the signal due to the source may be a significant and continuous background. The disadvantage of the second method is that it requires a motion mechanism, which adds significant complexity to the instrument design.

In spite of additional complexity, some space instruments have included radioactive sources to monitor instrument performance. The Particle Environment Monitor (PEM) experiment on the UARS satellite included an ^{241}Am α-source to track the in-flight performance of the solid-state detectors in that instrument [*Sharber et al.*, 1996]. The Medium Energy Particle Analyzer (MEPA) on the AMPTE CCE satellite included an alpha source to monitor both MCP and solid-state detector performance in that time-of-flight instrument [*McEntire et al.*, 1985]. Both the Energetic Particle Detector on the Galileo mission [*Williams et al.*, 1992] and the EPIC instrument on Geotail [*Williams et al.*, 1994] included Am alpha emitting sources to monitor performance. The use of the alpha source proved

Table 4.1: List of β sources

Isotope	Source Type	E(keV)
^{3}He	Endpoint	18.6
^{14}C	Endpoint	156
^{36}Cl	Endpoint	714
^{63}Ni	Endpoint	67
^{90}Sr/^{90}Y	Endpoint	546/2270
^{99}Tc	Endpoint	292
^{137}Cs	Line	624, 656
^{207}Bi	Line	482, 554, 976, 1048

particularly helpful in monitoring the performance of the MCP that was used to detect the secondary electrons created when an ion transited the "start" foil in the TOF component of these instruments [McEntire, private communication]. In locations where natural background was low and the alpha source dominated the response of the TOF instrument, the rate of "start" signals produced when the alpha transited the foil should be equal to the rate of "stop" signals produced when the alpha was absorbed by the solid-state detector. A ratio of significantly less than 1.0 indicates insufficient gain in the MCP and the requirement for an adjustment of the MCP bias voltage. The Electron, Proton, and Alpha Monitor (EPAM) on ACE [*Gold et al.*, 1998] used a variety of radioactive sources mounted on the reclosable telescope covers for in-flight calibration.

Sources that emit mono-energetic α-particles can be used to calibrate a single Si solid-state detector or a scintillator detector. The reason why only a single detector may be calibrated is that a typical 6 MeV α-particle has a range of 21 μm in silicon and will be stopped in the first detector it hits. Although radiation sources provide α-particles only in the energy range of 4 to 6 MeV, a lower energy may be obtained by placing a thin foil over the source. The energy of the emitted α-particles will be reduced at a cost of increased spread of the energy distribution. For a list of available α-particle sources see *Knoll* [2000].

Most β-particle sources provide electrons with a continuum of energies up to an end-point value. This is due to the physics of the process that produces them. Weak decay β-particles are produced in three-body process that also produces a neutrino, which carries away some of the available energy. The result is that the β-particle can have any energy from 0 to the end point value, which is unique to each β emitting isotope. Due to this property, the detector being calibrated with a β source will be exposed to β-particles with a continuum of energies. However, since the shape of the energy spectrum is constant in time, it may be possible to get some information about the gain of the system by monitoring ratios of count rates from key channels. There are a few electron conversion sources that produce mono-energetic electron lines, accompanied by γ-rays. A list of useful line and continuum β-particle sources is shown in Table 4.1

Sources that emit γ-rays can be used to calibrate Si solid-state detectors, particularly the ones with thicknesses range of hundreds of microns (see Section 3.5). The difficulty of this type of calibration is that solid-state detectors have low probability of interacting with a γ-ray and are not efficient in capturing its full energy. However, γ-ray sources are

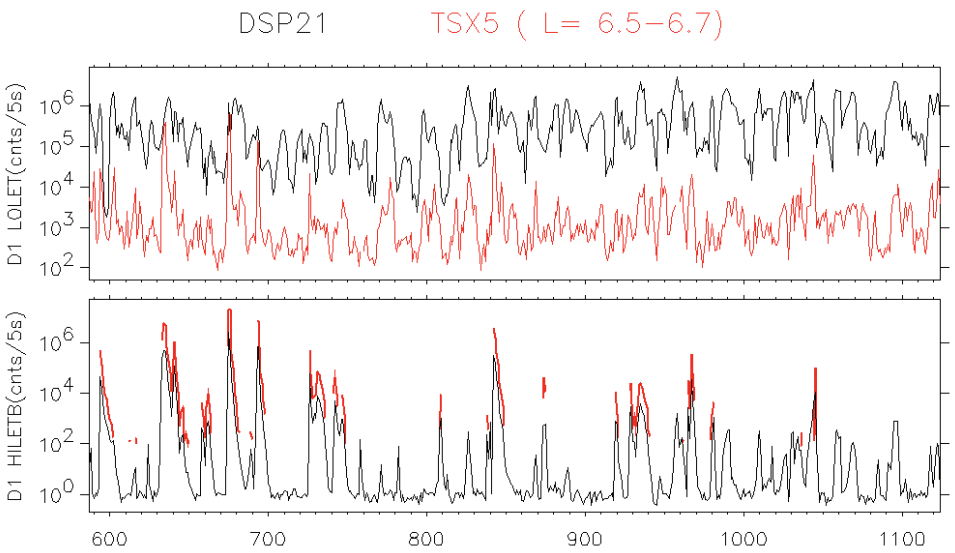

Figure 4.41: Daily averages of proton and electron dosimeter data, for L-Shells 6.6 to 6.7, for DSP and TSX-5 missions. HILETB is the proton dose and LOLET the electron dose. TSX-5 data are multiplied by 10 for clarity. Proton data (lower plot) show good correlation between the low altitude TSX-5 and geosynchronous DSP satellite. Energetic electron data do not correlate well due to different dynamics of the trapping process.

extremely useful in checking the calibration of scintillators. The relatively large size and the high density of scintillator sensors results in a high probability of an interaction with the γ-ray and a good probability of total absorption of the γ-ray energy. This results in a well defined peak at the γ-ray energy. The measured position of the peak can be used to track the end-to-end gain of the system. A list of useful γ-ray sources is shown in Table 3.1.

While, for the reasons given above, γ-ray sources are rarely included in space experiments, the cosmic ray electron experiment on Pioneer-10 made use of 2.6 MeV γ-rays originating from the RTG power source on that satellite to assess and correct for detector degradation that had occurred during the encounter with Jupiter's radiation belts [*Eraker*, 1982].

4.5.2 Relative Flux Response (Multi-Spacecraft)

Solar proton events generate high fluxes of very energetic protons. Near Earth, these protons appear both at high altitudes and in low-Earth orbit at high L values. As long as there are no high-energy electrons associated with the event, these protons provide a means of cross calibrating detectors on more than one spacecraft. Presence of high-energy electrons can be determined using real-time data from the POES electron sensor, available from the NOAA web site: `www.sel.noa.gov/data/`. An example of data from such cross-calibration is shown in Figure 4.41. Data plotted in the figure demonstrate a comparison between responses of identical Si solid-state detector dosimeters [*Dichter et al.*, 1998] in low-Earth (TSX-5 mission) and geosynchronous (DSP mission) orbits for the

same L values of 6.5 to 6.7. It is evident that the proton data for both detectors are in good agreement, while the electron data are not well correlated. This is as expected since the dynamics of trapped electrons are very different at the two altitudes. It is clear that solar event protons can provide a means to cross calibrate proton-sensing instruments.

The TSX-5 spacecraft spends very little time in the L-shell region of the geosynchronous DSP, thus accounting for the proton data gaps. Therefore, the comparison should be made by binning the data in multiple orbit bins, such as daily averages. The process of cross-calibration is easier with identical sensors, however, it is still possible to perform the task with different sensors. The daily averages may not have the same values but the timing and relative height of the observed structures should be in good agreement. Furthermore, the relative height of the structure should not vary with time, providing a method for long term calibration.

4.6 In-flight Relative and Absolute Calibration for Neutral Gas Sensors

One of the problems with calibration of neutral gas mass spectrometers is that once the process is finished, the instrument is bundled up in final flight configuration, exposed to thermal vacuum and vibration testing, launched and then left sealed for an extended period of time, sometimes in very hostile environments. The question then becomes: how relevant is the pre-launch calibration to the current flight operation of the instrument? Questions of interest for the pre-launch versus post-launch flight instrument include:

- What is the gas sensitivity?
- If mass peak jumping is used to increase the sample rate rather than more detailed mass spectral scanning, is the jump point on the top of the peak or on its side?
- What is the mass peak resolution?
- Are the focusing lenses in the ion beam path at their optimum transmission values?

Most, if not all, neutral gas mass spectrometers are sealed off in a vacuum prior to final delivery and testing. The advantage of a sealed mass spectrometer is that there is usually some background gas which can be used for full spectrometer sensor testing with the ion source filaments operating and with either vacuum or atmospheric pressure on the flight electronics. Some sensors even carry a low pressure atmosphere deliberately introduced to enhance the testing procedure [*Mahaffy et al.*, 2002; *Boies et al.*, 1994]. The other advantage of a sealed sensor is that it can be kept clean during maneuvers such as orbit insertion and thruster firings. The sensors can also be actively pumped by an ion pump or a getter material requiring no electrical power from the spacecraft.

Having arrived at its destination, the sensor is opened to its environment using a variety of different methods. For example, the Open Source Spectrometer instruments [*Nier et al.*, 1973] for the Atmosphere Explorer satellites were maintained under vacuum by an ion pump and opened by a cutter-wheel device [*Thorness and Nier*, 1962]. The Pioneer Venus Orbiter Neutral Mass Spectrometer [*Niemann et al.*, 1980a] vacuum was maintained by a small getter pump and the metal-ceramic break-off cap removed by a pyrotechnic

actuator which cracks the ceramic band, allowing the cap to be ejected. The ROSINA Double Focusing Mass Spectrometer [*Balsiger et al.*, 2007, 1998] and Reflectron Time-of-Flight sensors are evacuated through pump-out valves that are closed prior to launch. The system maintained a low level vacuum ($< 10^{-5}$ mbar) until it was opened pyrotechnically. After opening the cover can be closed by a motor. While sealed, this internal gas provides a means of evaluating the optimum operational voltages of many of the electrostatics lens systems, the integrated pulse height distribution of secondary multipliers, and the mass peak tuning. Repeated use of the same test script tracks instrument performance from initial sealing, through vibration and thermal vacuum tests, and into the post-launch period until the cover is ejected. This type of testing checks instrument performance but does not necessarily track its absolute sensitivity.

One example of a problem is described in *Kasprzak et al.* [1993] where the neutral mass spectrometer made measurements in the upper atmosphere of Venus from Dec. 1978 to Aug. 1980. After that period the periapsis of the orbit was not actively controlled and neutral density measurements were not possible until June 1992 to October 1992. It was discovered that the instrument had a different mass peak tuning for masses near 44 u/charge (CO_2) than that of the earlier period. The only gas available for mass tuning was ambient CO_2 that is abundant on the night side only at very low altitudes. The desire to sample all gas species at high time resolution (i.e., mass peak jumping) was in conflict with the desire to determine the proper instrument tuning due to the low telemetry data rate, the limited instrument modes available, the low neutral density, a spinning spacecraft and the short time period (several minutes) available per periapsis pass for diagnostics. If an independent gas source were available for checking mass tuning at places other than at periapsis, the process would have been much easier. Since the instrument was retuned, there was also the possibility that the individual mass peak sensitivities could have changed as a result.

Chereji et al. [1978] describe a device to supply a constant reproducible amount of deuterium into an entrance of a mass spectrometer open to space using a palladium valve that is temperature controlled. The flow rate is 3×10^{-4} to $3\times10^{-3}\mu$l s^{-1}. *Outlaw et al.* [1971] describe a metal-gas binary system that uses hydrogen dissolved in erbium. The temperature of the system determines the equilibrium hydrogen pressure.

The Pioneer Venus Bus Neutral Gas Mass Spectrometer (BNMS) [*Hoffman et al.*, 1980b] carried a small glass vial of a calibration gas (He). With the instrument still sealed in launch configuration and four days before entry into the Venus atmosphere, a pyrotechnic device was fired crushing the vial, expanding a known quantity of gas into the mass spectrometer with closely estimated volume. This was done to check the gain of the low mass continuous channel multiplier which could not be checked with a direct current measurement as could the high mass channel. The Pioneer Venus Sounder Probe Neutral Gas Mass Spectrometer [*Hoffman et al.*, 1980a] carried a calibration gas mixture of methane and ^{136}Xe to provide mass peaks at 15 u/charge (CH_3^+), 68 u/charge ($^{136}Xe^{2+}$) and 136 u/charge ($^{136}Xe^+$).

The BUGATTI experiments [*von Zahn et al.*, 1990] used instruments with a double-focusing Mattauch-Herzog electric and magnetic deflection mass spectrometer with an in-flight calibration system (Figure 4.42). To protect the stability of the mass spectrometer calibration, an ion source cover is attached to the instrument while it is still under vacuum inside the calibration system. Shortly before the ion source cover is ejected after launch, an in-flight calibration for N_2, O_2 and Ar is performed with gases stored in a glass vial

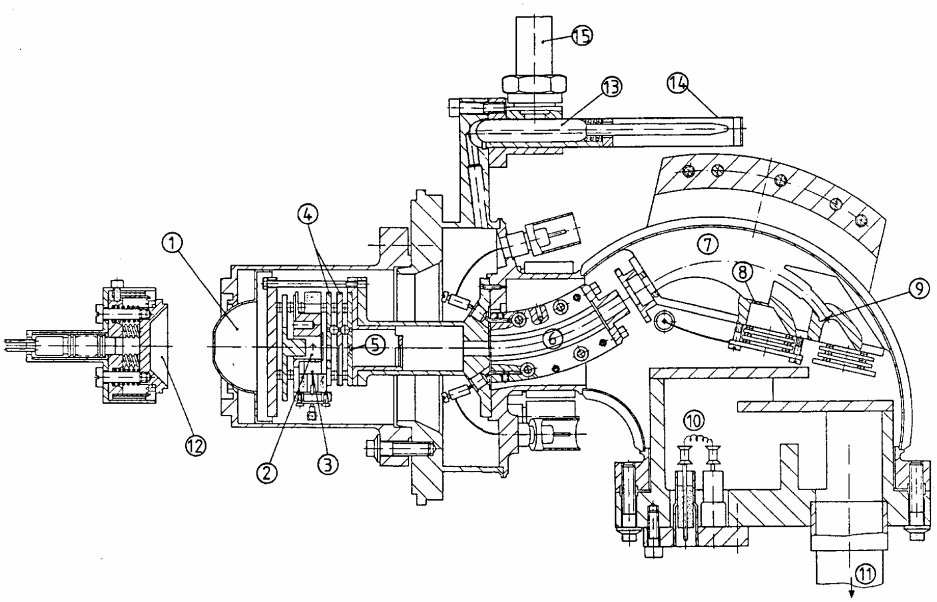

Figure 4.42: The BUGATTI mass spectrometer. The In-Flight Calibration cell (IFC) consists of a glass vial (13) attached to a metal tube (14) that is broken by a squib (15) releasing gas into the ion source (2, 3, 4) and antechamber (1) that has an ejectable cover (12). From *von Zahn et al.* [1990].

that is broken. An ion getter pump slowly removes the released gas. Two volumes were used for each instrument (0.14 mbar and 1.44 mbar of 79.1 % N_2, 19.8 % O_2, and 1.08 % Ar to match the assumed gas composition at 100 km on Earth). The lower pressure vial is broken first and the higher pressure vial 15 seconds later. The curves (Figure 4.43) are extrapolated back to zero time in order to establish the absolute pressure based on the initial filling pressure and the vial to ion source volume ratio.

The Midcourse Space Experiment (MSX) contamination mass spectrometer [*Boies et al.*, 1994] was backfilled with trace amounts of He, Ar, Kr, and Xe. The gas mix was used as a means of tracking the instrument sensitivity and mass linearity from instrument integration and testing through launch until cover break off. After break off, a comparison was made with a total pressure sensor measuring similar contamination gases. For orbital instruments, comparison with orbital drag measurement of the total density can also be used [*Hedin et al.*, 1983].

The NGIMS [*Mahaffy et al.*, 2002] instrument aboard the CONTOUR spacecraft has a gas reservoir with two valves: 1) a rupture valve that maintains the gas in the volume until it is pierced by a lance; and 2) a standard valve that can be commanded open or closed (Figure 4.44). Both valve types are used in the GCMS instrument aboard Huygens Probe [*Niemann et al.*, 1997, 2002]. A Kulite pressure sensor monitors the volume pressure. The gas mixture is 9.2 % of ^{129}Xe, 18.6 % of Ar and 72.2 % of Ne contained in a volume of 5.6 cm^3 at an initial pressure of 466.6 mbar. Isotopic ^{129}Xe is used in order to prevent confusion with possible comet Xe at other isotopes. The same mixture was used to backfill the sensor at very low pressure before final sealing. The mixture in the gas reservoir is

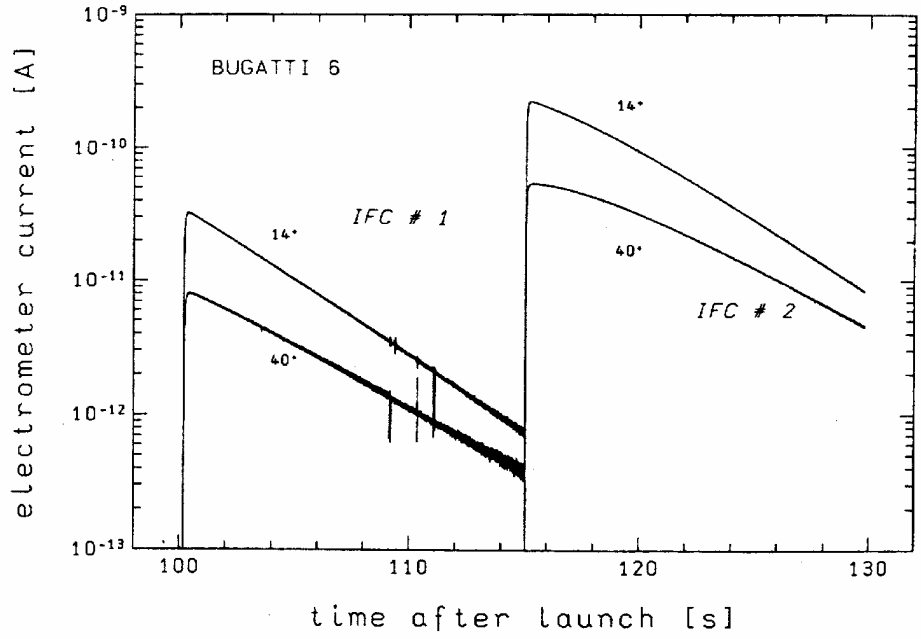

Figure 4.43: The In-Flight Calibration volume pressure decays for IFC #1 (volume 1) and IFC #2 (volume 2). From *von Zahn et al.* [1990].

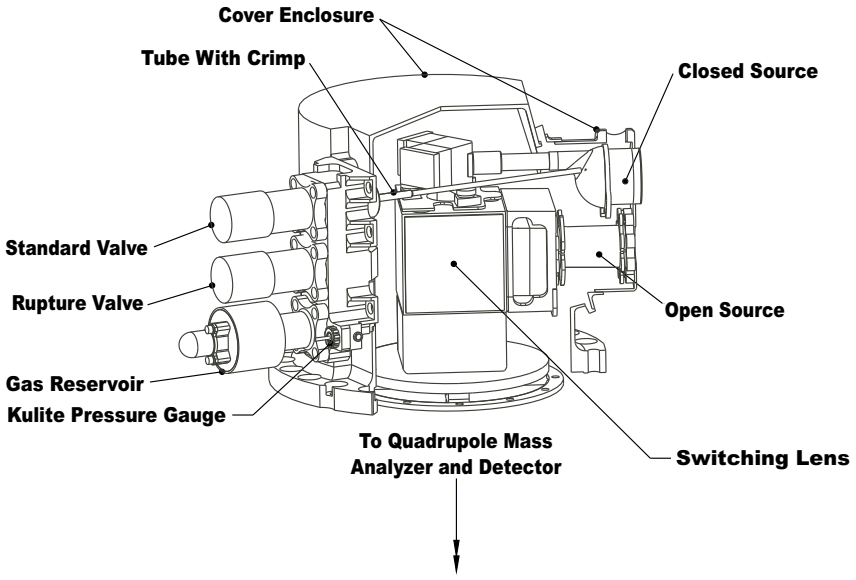

Figure 4.44: The CONTOUR NGIMS ion source with in-flight gas calibration volume. From *Mahaffy et al.* [2002].

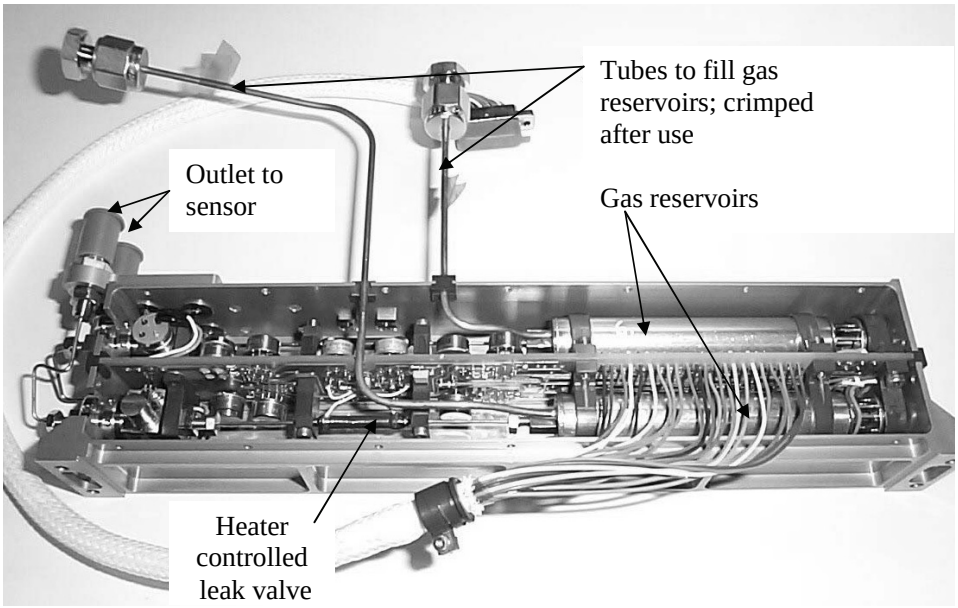

Figure 4.45: The ROSINA DFMS in-flight gas calibration unit (GCU) [*Balsiger et al.*, 2007, 1998].

admitted to the ion source volume by a small tube with a crimp in it for gas flow restriction. A dome covers the volume containing the open source and closed source. A small hole in the antechamber wall allows gas into the closed source. The purpose of the gas mixture is to allow a check of mass peak tuning for middle and low frequencies of the three frequency quadrupole system. It also allows scans of the electric potentials on the programmable ion focusing elements to confirm optimum transmission settings after a comet encounter. Relative sensitivity changes before and after comet encounters can also be detected. The noble gases were chosen since they are chemically inert, with no surface adsorption. The disadvantage for NGIMS is that the isotopic mass of Xe only goes up to 129 u/charge, while the instrument mass range is up to 300 u/charge.

The ROSINA instrument package for the Rosetta Mission [*Balsiger et al.*, 2007, 1998] has both a double focusing mass spectrometer (DFMS), mass range 12–100 u/charge, and a time-of-flight mass spectrometer (RTOF), mass range 1–300 u/charge. The DFMS has one ion source and the RTOF two ion sources (an orthogonal source and an ion storage source). Each instrument has two in-flight gas calibration units (GCU) with a connecting tube to each ion source (Figure 4.45). The reservoir volume is about about 10 cm^3 and contains a gas mixture at about 5 bars pressure. The mixture for DFMS consists of 4.5 % Ne, 93 % CO_2 and 2.5 % Xe while that for the RTOF consists of 33.3 % He, 33.4 % CO_2 and 33.3 % Kr by weight. There is a high pressure gauge for the gas reservoir and a mini-Pirani low pressure gauge (range 0.2–0.04 mbar). The valve is a non-commercial design with a flow rate that is temperature controlled and operates below 60 °C. The gas flow into the ion source is dependent on the conductivity and the flow system in the capillary and

tube to the ion source. The ion source pressure with the calibration gases should be below 3×10^{-6} mbar.

No problems, such as premature gas leaks or chemical changes in the test gases, have been encountered with the use of trace gas releases to check post-launch calibrations of neutral gas spectrometers.

4.7 In-Flight Relative and Absolute Calibration for ENA Instruments

In-flight calibration of Energetic Neutral Atom (ENA) instruments is difficult for two reasons. First, there are no "well-calibrated" neutral particle sources in space that can be used to establish an absolute in-flight calibration. Second, since ENAs are neutral particles, a Faraday cup detector, which is a very reliable detector for cross-calibrating charged particle detectors, can not be used. The ENA instrument in-flight calibration generally relies on comparisons with plasma measurements. ENA instruments have a charged particle rejection system at their entrance and their detectors generally react to charged particles in a manner similar to neutrals. Therefore when the rejection system is switched off, ions can enter the ENA instrument and be detected in the same way as neutral particles. This generally requires the ion spectra to have relatively low fluxes in the energy range of the ENA instrument to prevent the ENA instrument's saturation. This often limits the periods where cross-calibration can be performed to those when the plasma sensor, which has much smaller geometric factor, has a count rate slightly above its background rate. By using ion distributions established through cross-calibration with a plasma instrument on the same spacecraft, one can establish an absolute in-flight calibration for the ENA instrument. This method also assumes that the plasma instrument's absolute calibration has been determined, which usually requires cross-calibration with a third instrument.

For a relative calibration of an ENA instrument with look direction, one can often make use of the detector's sensitivity to UV photons. For mass resolving sensors that incorporate microchannel plates (MCPs) in their time-of-flight detectors, a UV photon entering the instrument can trigger either the start or the stop detector with a certain probability (in the range of 10^{-3} to 10^{-2}). Since many UV sources, e.g. stars, are sufficiently constant with time, monitoring these UV-induced background rates over the mission allows assessment of sensor degradation. Corrections for that degradation can be made by increasing the MCP bias voltages. Furthermore, stars are point sources and thus they can be used to establish the imaging quality of the ENA instrument and to derive the minimum point spread function. This provides only an estimate of the point spread function because registered ENAs suffer a degradation of their energy and flight direction in the course of their detection in the instrument [*Wurz*, 2000; *Henderson et al.*, 2005]. Lastly, the absolute pointing of the ENA instrument can be established using the UV signal from stars, as was performed with the GAS instrument on Ulysses [*Witte et al.*, 2004].

An additional method of testing ENA instrument calibration is through a comparison of the model determined source distribution of plasma with *in situ* plasma data from a spacecraft located in the source region. ENA imaging instruments record a 2-D image of a three-dimensional plasma population, where the third dimension is collapsed into a line-of-sight integral [*Wurz*, 2000]. To interpret ENA images, one needs an inversion model to establish the three dimensional structure of the plasma population. This evaluation has

been performed for the terrestrial ring current where *in situ* plasma measurements by the CIS instruments on Cluster have been compared with ENA images recorded with HENA on IMAGE. *Vallat et al.* [2004] found mixed agreement between these two measurements, with three of the four high flux ($> 10^5$ cm^{-2} sr^{-1} s^{-1} keV^{-1}) measurements within the HENA error bars, and two low flux measurements outside the HENA error bars. The study also identified several limitations to using the inversion technique including finite angular resolution of the camera, limited precision of the exospheric hydrogen and magnetic field models, and averaging caused by the line-of-sight integral response. All of these contributed to a scatter of the calculated fluxes with respect to the measured fluxes.

4.8 Conclusion

As the material in this chapter has made abundantly clear, unexpected spurious responses and post-launch changes in performance on the part of space plasma instrumentation are very much the rule and only rarely the exception. It is important to anticipate at the earliest stage of an experiment program that this will happen and devise instrument design features and post-launch operating procedures that will mitigate, identify, and correct for instrument changes and spurious responses.

Proper instrument shielding, aperture and analyzer structure design, and choice of materials and surface coatings are important factors in minimizing spurious instrument responses. Even then, situations may occur in space when the physical parameter that is to be measured is of such low intensity relative to sources of spurious response, that the spurious instrument response dominates. Thought must be given as early as possible to procedures that would serve to identify such situations so that those data would be excluded from analysis.

Detector variations and degradation with time appears to be an unavoidable feature of space plasma instrumentation. It is very important that instrument design and operating procedures include features that serve to identify and correct for these effects. While not an inclusive list, at the very least instruments using CEMs or MCPs should be designed with ground commandable pulse counting threshold setting that permit detector pulse height distributions to be determined and commandable bias voltage settings that compensate for detector gain losses. The ability to command a plasma instrument to measure, for example, a fixed particle energy or limited energy range can also be valuable in identifying instrument performance anomalies. For energetic particle detectors, having a radioactive source or flying a calibration detector that experiences minimal exposure to degradation, can greatly simplify the in-flight calibration process. Similarly, including a mechanism for releasing calibration gases into neutral gas detectors can reduce uncertainties in the in-flight calibration effort.

In closing, addressing the problems described in this chapter at the instrument design stage and developing procedures to handle post-launch instrument performance at the earliest possible time in the program is vital to a successful experiment.

Acknowledgements

The authors would like to thank Sue Greer for creating the figures displaying data from the SEM on the POES satellites, Joseph Fennell for supplying and explaining the SCATHA

figure and Walter Lennartsson and Edward Shelley for supplying and explaining the ISEE-1 ion mass spectrometer figure.

Bibliography

Aellig, M., A. Lazarus, and J. Steinberg, The solar wind helium abundance: Variation with wind speed and the solar cycle, *Geophys. Res. Lett.*, **28**, 2767–2770, 2001.

Alinejad, N. and T.P. Armstrong, Galileo energetic particle detector observations of geomagnetically trapped protons, *J. Geophys. Res.*, **102**, 27053–27068, 1997.

Archuleta. R. J. and S.E. DeForest, Efficiency of channel electron mulipliers for electrons 1–50 keV, *Rev. Sci. Instrum.*, **42**, No. 1, 89–91, 1971.

Balsiger, H., K. Altwegg, E. Arijs, J.-L. Bertaux, J.-J. Berthelier, B. Block, P. Bochsler, G.R. Carignan, L. Duvet, P. Eberhardt, B. Fiethe, J. Fischer, L.A. Fisk, S.A. Fuselier, A.G. Ghielmetti, F. Gliem, T.I. Gombosi, M. Illiano, T. Koch, E. Kopp, A. Korth, K. Lange, H. Lauche, S. Livi, A. Loose, T. Magoncelli, C. Mazelle, M. Mildner, E. Neefs, D. Nevejans, H. Rème, J.A. Sauvaud, S. Scherer, A. Schoenemann, E.G. Shelley, J.H. Waite, C. Westermann, B. Wilken, J. Woch, H. Wollnik, P. Wurz, and D.T. Young, Rosetta Orbiter Spectrometer for Ion and Neutral Analysis-ROSINA, *Adv. Space Res.*, **21**, 1527–1535, 1998.

Balsiger, H., K. Altwegg, E. Arijs, J.-L. Bertaux, J.-J. Berthelier, B. Block, P. Bochsler, G.R. Carignan, L. Duvet, P. Eberhardt, B. Fiethe, J. Fischer, L.A. Fisk, S.A. Fuselier, A.G. Ghielmetti, F. Gliem, T.I. Gombosi, M. Illiano, T. Koch, E. Kopp, A. Korth, K. Lange, H. Lauche, S. Livi, A. Loose, T. Magoncelli, C. Mazelle, M. Mildner, E. Neefs, D. Nevejans, H. Rème, J.A. Sauvaud, S. Scherer, A. Schoenemann, E.G. Shelley, J.H. Waite, C. Westermann, B. Wilken, J. Woch, H. Wollnik, P. Wurz, and D.T. Young, Rosetta Orbiter Spectrometer for Ion and Neutral Analysis-ROSINA, *Space Sci. Rev.*, 128, 745–801, doi:10.1007/s11214-006-8335-3, 2007.

Bamert, K., Suprathermal particles associated with coronal mass ejections, Ph.D. thesis, University of Bern, 2004.

Barabash, S., R. Lundin, H. Andersson, J. Gimholt, M. Holström, O. Norberg, M. Yamauchi, K. Asamura, A.J. Coates, D.R. Linder, D.O. Kataria, C.C. Curtis, K.C. Hsieh, B.R. Sandel, A. Fedorov, A. Grigoriev, E. Budnik, M. Grande, M. Carter, D.H. Reading, H. Koskinen, E. Kallio, P. Riihela, T. Saeles, J. Kozyra, N. Krupp, S. Livi, J. Woch, J. Luhmann, S. McKenna-Lawlor, S. Orsini, R. Cerrulli-Irelli, A. Mura, A. Milillo, E. Roelof, D. Williams, J.-A. Sauvaud, J.-J. Thocaven, D. Winningham, R. Frahm, J. Scherer, J. Sharber, P. Wurz, and P. Bochsler, The Analyzer of Space Plasmas and Energetic Atoms (ASPERA-3) for the Mars Express Mission, *ESA Special Publication*, **SP-1240**, ESA Publications Division, Noordwijk, 121–139, 2004.

Basu, B., J.R. Jasperse, R.M. Robinson, R.R. Vondrak, and D.S. Evans, Linear transport theory of auroral proton precipitation: a comparison with observations, *J. Geophys. Res.*, **92**, 5920–5932, 1987.

Benson, R.F., P. Bauer, L.H. Brace, H.C. Carlson, J. Hagen, W.B. Hanson, W.R. Hoegy, M.R. Torr, R.H. Wand, and V.B. Wickwar, Electron and ion temperatures - A comparison of ground based incoherent scatter and AE-C measurements, *J. Geophys. Res.*, **82**, 36–42, 1977.

Boies, M.T., R.C. Benson, J.D. Kinnison, J.S. Morgan, T.E. Phillips, O.M. Uy, and W. Wilkinson, Comparative sensor calibration: Mid-course Space Experiment (MSX) neutral mass spectrometer and total pressure sensor, *Proc. SPIE*, **2261**, 208–217, 1994.

Bougeret, J.-L., M.L. Kaiser, P.J. Kellogg, R. Manning, K. Goetz, S.J. Monson, N. Monge, L. Friel, C.A. Meetre, C. Perche, L. Sitruk, and S. Hoang, Waves: The radio and plasma wave investigation on the Wind spacecraft, *Space Sci. Rev.*, **71**, 231–263, 1995.

Brace, L.H., W.R. Hoegy, and R.F. Theis, Solar EUV measurements at Venus based on photoelectron emission from the Pioneer Venus Langmuir probe., *J. Geophys. Res.*, **93**, 7282–7296, 1988.

Brace, L.H., H.C. Carlson, and K.K. Mahajan, Radar backscatter and rocket probe measurements of electron temperature over Arecibo, *J. Geophys. Res.*, **74**, 1883–1885, 1969.

Brace, L.H. and J.A. Findlay, Comparison of cylindrical electrostatic probe measurements on Alouette II and Explorer 31 satellites, *Proc. IEEE*, **57**, 1057–1060, 1969.

Brace, L.H., G.R. Carignan, and J.A. Findlay, Evaluation of ionospheric electron temperature measurements by cylindrical probes, *Space Res.*, **11**, 1079–11051, 1971.

Brace, L.H., Langmuir probe measurements in the ionosphere, in *Measurement Techniques for Space Plasmas: Particles*, R. Pfaff, J. Borovsky, and D.T. Young, Eds., Geophys. Monogr. Ser., **103**, American Geophysical Union, Washington, D.C., 23–35, 1998.

Carlson, C.W., J.P. McFadden, R.E. Ergun, M. Temerin, W. Peria, F.S. Mozer, D.M. Klumpar, E.G. Shelley, W.K. Peterson, E. Möbius, R. Elphic, R. Strangeway, C.A. Cattell, and R. Pfaff, FAST observations in the downward auroral current region: Energetic upgoing electron beams, parallel potential drops, and ion heating, *Geophys. Res. Lett.*, **25**, 2017–2020, 1998.

Carlson, C.W. and J.P. McFadden, Design and applications of imaging plasma instruments, in *Measurement Techniques in Space Plasmas: Particles*, R.-Pfaff, J.-Borovsky, and D.T.-Young, Eds., Geophys. Monogr. Ser., **102**, American Geophysical Union, Washington, D.C., 125–140, 1998.

Carlson, C.W., J.P. McFadden, P. Turin, D.W. Curtis, and A. Magoncelli, The electron and ion plasma experiment for FAST, *Space Sci. Rev.*, **98**, 33–66, 2001.

Chereji, I., G. Toderean, V. Mercea, and V. Istomin, Device for in-flight calibration of mass spectrometer, *Space Sci., Instrum.*, **4**, 107–110, 1978.

Chua D., G. Parks, M. Brittnacher, W. Peria, G. Germany, J. Spann, and C. Carlson, Energy characteristics of auroral electron precipitation: A comparison of substorms and pressure pulse related auroral activity, *J. Geophys. Res.*, **106**, 5945–5956, 2001.

Coplan M.A., F. Ipavich, J. King, K.W. Ogilvie, D.A. Roberts, and A.J. Lazarus, Correlation of solar wind parameters between SOHO and Wind, *J. Geophys. Res.*, **106**, 18615–18624, 2001.

Dichter, B.K., J.O. McGarity, M.R. Oberhardt, V.T. Jordanov, D.J. Sperry, A.C. Huber, J.A. Pantazis, E.G. Mullen, G. Ginet, and S.G. Gussenhoven, Compact Environmental Anomaly Sensor (CEASE): A novel spacecraft instrument for in situ measurements of environmental conditions, *IEEE Trans. Nucl. Sci.*, **45**, 2758–2764, 1998.

Dichter, B.K. and S. Woolf, Grazing angle proton scattering: effects on Chandra and XMM-Newton X-ray telescopes, *IEEE Trans. Nucl. Sci.*, **50**, 2292–2295, 2003.

Donley, J.L., L.H. Brace, J.A. Findlay, J.H. Hoffman, and G.L. Wrenn, Comparison of results of Explorer XXXI direct measurement probes, *Proc. IEEE*, **57**, 1078–1084, 1969.

Eraker, J.H., Origins of the low-energy relativistic interplanetary electrons, *Astrophys. J.*, **257**, 862–880, 1982.

Escoubet, C.P., A. Pedersen, R. Schmidt, and P.A. Lindqvist, Density in the magnetosphere inferred from ISEE 1 spacecraft potential, *J. Geophys. Res.*, **102**, 17595–17609, 1997.

Etcheto, J. and A. Saint-Marc, Anomalously high plasma densities in the plasma sheet boundary layer, *J. Geophys. Res.*, **90**, 5338–5344, 1985.

Evans, D.S. and M.S. Greer, Polar Orbiting Environmental Satellite Space Environment Monitor-2: Instrument descriptions and archive data documentation, NOAA Technical Memorandum, **OAR SEC-93**, 2000.

Fennell, J.F., Description of P78-2/SCATHA/ satellite and experiments, *The IMS Source Book: Guide to the International Magnetospheric Study Data Analysis*, C.T. Russell and D.J. Southwood, Eds., American Geophysical Union, Washington, D. C., 65–81, 1982.

Frey, H.U., S.B. Mende, C.W. Carlson, J.C. Gérard, B. Hubert, J. Spann, R. Gladstone, and T.J. Immel, The electron and proton aurora as seen by IMAGE-FUV and FAST, *Geophys. Res. Lett*, **28**, 1135–1138, 2001.

Frey, H.U., S.B. Mende, T.J. Immel, J.-C. Gérard, B. Hubert, S. Habraken, J. Spann, G.R. Gladstone, D.V. Bisikalo, and V.I. Shematovich, Summary of quantitative interpretation of IMAGE far ultraviolet auroral data, *Space Sci. Rev.*, **109**, 255–283, 2003.

Fritz, T.A. and J.R. Cessna, ATS-6 NOAA low energy proton experiment, *IEEE Trans. Aerospace and Electronic Sys.*, **AES-11**, No. 6, 1145–1154, 1975.

Fuller-Rowell, T.J. and D.S. Evans, Height-integrated Pedersen and Hall conductivity patterns inferred from the TIROS-NOAA satellite data, *J. Geophys. Res.*, **92**, 7606–7618, 1987.

Galli, A., P. Wurz, H. Lammer, H.I.M. Lichtenegger, R. Lundin, S. Barabash, A. Grigoriev, M. Holmström, and H. Gunell, The hydrogen exospheric density profile measured with ASPERA-3/NPD, *Space Sci. Rev.*, **126**, 447–467, 2006.

Gao, R.S., P.S. Gibner, J.H. Newman, K.A. Smith, and R.F. Stebbings: Absolute and angular efficiencies of a microchannel-plate position-sensitive detector, *Rev. Sci Instrum.*, **55**, 1756–1759, 1984.

Gérard, J.-C., B. Hubert, M. Meurant, V.I. Shematovich, D.V. Bisikalo, H. Frey, S. Mende, G.R. Gladstone, and C.W. Carlson, Observation of the proton aurora with IMAGE FUV imager and simultaneous ion flux in-situ measurements, *J. Geophys. Res.*, **106**, 28939–28948, 2001.

Gloeckler, G., J. Geiss, H. Balsiger, L.A. Fisk, F. Gliem, F.M. Ipavich, K.W. Ogilvie, W. Stüdemann, and B. Wilken, The ISPM Solar-Wind Ion Composition Spectrometer, *ESA Special Publication*, **SP-1050**, ESA Publications Division, Noordwijk, 77–103, 1983.

Gold, R.E., S.M. Krimigis, S.E. Hawkins III, D.K. Haggerty, D.A. Lohr, E. Fiore, T.P. Armstrong, G. Holland, and L.J. Lanzerotti, Electron, proton, and alpha monitor on the Advanced Composition Explorer spacecraft, *Space Sci. Rev.*, **86**, 541–562, 1998.

Goruganthu, R.R. and W.G. Wilson, Relative electron detection efficiency of microchannel plates from 0-3 keV, *Rev. Sci. Instrum.*, **55**, 2030–2033, 1984.

Hedin, A.E., H.B. Niemann, W.T. Kasprzak, and A. Seiff, Global Empirical Model of the Venus Thermosphere, *J. Geophys. Res.*, **88**, 73–83, 1983.

M.G. Henderson, M.F. Thomsen, R. Skoug, M.H. Denton, R. Harper, H.O. Funsten, and C.J. Pollock, Calculation of IMAGE/MENA geometric factors and conversion of images to units of integral and differential flux, *Rev. Sci. Instrum.*, **76**, 043303-1–043303-24, 2005.

Hirahara, M., T. Mukai, T. Terasawa, S. Machida, Y. Saito, T. Yamamoto, and S. Kokubun, Cold dense ion flows with multiple components observed in the distant tail lobe by Geotail, *J. Geophys. Res.*, **101**, 7769–7784, 1996.

Hoffman, J.H., R.R. Hodges, W.W. Wright, V.A. Blevins, K.D. Duerksen, and L.D. Brooks, Pioneer Venus Sounder Probe Neutral Gas Mass Spectrometer, *IEEE Trans. Geosci. Remote Sens.*, **GE-18**, 80–84, 1980a.

Hoffman, J.H., K. Pelka, U. von Zahn, D. Krankowsky, and D. Linkert, The Pioneer Venus Bus Neutral Gas Mass Spectrometer, *IEEE Trans. Geosci. Remote Sens.*, **GE-18**, 122–126, 1980b.

Hubert, B., J.C. Gérard, D.S. Evans, M. Meurant, S.B. Mende, H.U. Frey, and T.J. Immel, Total electron and proton energy input during auroral substorms: remote sensing with IMAGE-FUV, *J. Geophys. Res.*, **107**, SMP 15-1 to SMP 15-12, 2002.

Ipavich, F.M., A.B. Galvin, S.E. Lasley, J.A. Paquette, S. Hefti, K.-U. Reiche, M.A. Coplan, G. Gloeckler, P. Bochsler, D. Hovestadt, H. Grünwaldt, M. Hilchenbach, F. Gliem, W.I. Axford, H. Balsiger, A. Bürgi, J. Geiss, K.C. Hsieh, R. Kallenbach, B. Klecker, M.A. Lee, G.G. Managadze, E. Marsch, E. M"obius, M. Neugebauer, M. Scholer, M.I. Verigin, B. Wilken, and P. Wurz, Solar wind measurements with SOHO: The CELLAS/MTOF proton monitor, *J. Geophys. Res.*, **103**, 17205–17214, 1998.

Issautier, K., R.M. Skoug, J.T. Gosling, S.P. Gary, and D.J. McComas, Detailed comparison between the URAP and SWOOPS experiments, *J. Geophys. Res.*, **106**, 15665–15675, 2001.

Johnstone, A.D., A.J. Coates, B. Wilken, W. Studemann, W. Weiss, R.C. Ireli, V. Formisano, H. Borg, S. Olsen, J.D. Winningham, D.A. Bryant, and S.J. Kellock, The Giotto three-dimensional positive-ion analyzer, *J. Phys. E*, **20**, 795–805, 1987.

Johnstone, A.D., C. Alsop, S. Burge, P.J. Carter, A.J. Coates, A.J. Coker, A.N. Fazakerley, M. Grande, R.A. Gowen, C. Gurgiolo, B.K. Hancock, B. Narheim, A. Preece, P.H. Sheather, J.D. Winningham, and R.D. Woodliffe, Peace: a Plasma Electron and Current Experiment, *Space Sci. Rev.*, **79**, 351–398, 1997.

Kasper, J.C., A.J. Lazarus, J.T. Steinberg, K.W. Ogilvie, and A. Szabo, Physics-based test to identify the accuracy of solar wind ion measurements: A case study with the Wind Faraday cup, *J. Geophys. Res.*, **111**, doi:10.1029/2005JA011442, 2006.

Kasprzak, W.T., A.E. Hedin, H.B. Niemann, and N.W. Spencer, Atomic nitrogen in the upper atmosphere of Venus, *Geophys. Res. Lett.*, **7**, 106–108, 1980.

Kasprzak, W.T., H.B. Niemann, A.E. Hedin, S.W. Bougher, and D.M. Hunten, Neutral composition measurements by the Pioneer Venus neutral mass spectrometer during Orbiter re-entry, *Geophys. Res. Lett.*, **20**, 2747–2750, 1993.

Kasprzak, W.T., H. Niemann, D. Harpold, J. Richards, H. Manning, E. Patrick, and P. Mahaffy, Cassini Orbiter ion and neutral mass spectrometer instrument, *Proc. SPIE*, **2803**, 129–140, 1996.

Keller, C.A. and B.H. Cooper, Quantitative detection of low energy positive and negative ions with a channel electron multiplier, *Rev. Sci. Instrum.*, **67**, 2760–2764, 1996.

Klumpar, D.M., E. Möbius, L.M. Kistler, M. Popecki, E. Hertzberg, K. Crocker, M. Granoff, Li Tang, C.W. Carlson, J. McFadden, B. Klecker, F. Eberl, E. Künneth, H. Kästle, M. Ertl, W.K. Peterson, E.G. Shelley, and D. Hovestadt, The Time-of-flight Energy, Angle, Mass Spectrograph (TEAMS) experiment for FAST, *Space Sci. Rev.*, **98**, 197–219, 2001.

Knoll, G.F., *Radiation Detection and Measurement*, John Wiley & Sons, New York, 2000.

Krehbiel, J.P., L.H. Brace, R.F. Theis, W.H. Pinkus, and R.B. Kaplan, The Dynamics Explorer Langmuir probe instrument, *Space Sci. Instr.*, **5**, 493–502, 1981.

Lagg, A., N. Krupp, S. Livi, J. Woch, S.M. Kirmigis, and M.K. Dougherty, Energetic particle measurements during the Earth swing-by of the Cassini spacecraft in August 1999, *J. Geophys. Res.*, **106**, 30209–30222, 2001.

Larson, D.E., R.P. Lin, and J. Steinberg, Extremely cold electrons within the January 1997 magnetic cloud, *Geophys. Res. Lett.*, **27**, 157–160, 2000.

Lees, J.E., G.W. Fraser, and J.F. Pearson: 1990, After emission in Microchannel Plate detectors, in *EUV, X-Ray, and Gamma-Ray Instrumentation for Astronomy*, O.H. Siegmund, H.S. Hudson, Eds., *Proc. SPIE*, **1344**, 333–339, 1990.

Lemaire, J.E. and K.I. Gringauz, with contributions from D.L. Carpenter and V. Bassolo, *The Earth's Plasmasphere*, Cambridge Atmospheric and Space Science Series, Cambridge University Press, 1998.

Lin, R.P., K.A. Anderson, S. Ashford, C. Carlson, D. Curtis, R. Ergun, D. Larson, J. McFadden, M. McCarthy, G.K. Parks, H. Rème, J.M. Bosqued, J. Coutelier, F. Cotin, C. d'Uston, K.-P. Wenzel, T.R. Sanderson, J. Henrion, J.C. Ronnet, and G. Paschmann: A three-dimensional plasma and energetic particle experiment for the Wind spacecraft, *Space Sci. Rev.*, **71**, 125–153, 1995.

Lin, R.P., D. Larson, T. Phan, R. Ergun, J. McFadden, K. Anderson, C. Carlson, M. McCarthy, G.K. Parks, R. Skoug, R. Winglee, H. Rème, N. Lormant, J.M. Bosqued, C. d'Uston, T.R. Sanderson, and K.-P Wenzel, Wind observations of suprathermal particles in the solar wind, in *Geospace Mass and Energy Flow: Results From the International Solar-Terrestrial Physics Program*, J.L. Horwitz, D.L. Gallagher, and W.K. Peterson, Eds., Geophys. Monogr. Ser., **104**, 1–12, American Geophysical Union, Washington, D.C., 1998.

Lin, C.S. and R.A. Hoffman, Characteristics of the inverted-V event, *J. Geophys. Res.*, **84**, 1514–1524, 1979.

Lummerzheim D., M. Brittnacher, D. Evans, G.A. Germany, G.K. Parks, M.H. Rees, and J.F. Spann, High time resolution study of the hemispheric power carried by energetic electrons into the ionosphere during the May 19/20, 1996 auroral activity, *Geophys. Res. Lett.*, **24**, 987–990, 1997.

Mahaffy, P.R., personal communication, Code 699, Goddard Space Flight Center: Mahaffy, P.R., W.T. Kasprzak, D. Harpold, H.B. Niemann, R. Bitzel, B. Block, J. Demick, S. Feng,

C. Gunderson, S. Leake, J. Maurer, R. Miller, T. Owen, E. Patrick, M. Paulkovich, E. Raaen, J. Richards, F. Tan, S. Schwinger, S. Way, and J. Winchester, The Neutral Gas and Ion Mass Spectrometer for the CONTOUR Mission, originally prepared for *Space Sci. Rev.*, 2002.

Maksimovic, M., S. Hoang, N. Meyer-Vernet, M. Moncuquet, J.-L. Bougeret, J.L. Phillips, and P. Canu, Solar wind electron parameters from quasi-thermal noise spectroscopy and comparison with other measurements on Ulysses, *J. Geophys. Res*, **100**, 19881–19892, 1995.

Malter, L., Thin film field emission, *Phys. Rev.*, **50**, 48–58, 1936.

Martin, A., J. Vallerga, J. McPhate, and O. Siegmund, Further scrubbing and quantum efficiency results of the HST-COS Far-Ultraviolet Detector, *Proc. SPIE*, **4854**, 526–531, 2003.

McClure, J.P., W.B. Hanson, A.F. Nagy, R.J. Cicerone, L.H. Brace, M. Baron, P. Bauer, H.C. Carlson, J.V. Evans, G.N. Taylor, and R.F. Woodman, Comparisons of Te and Ti from OGO-6 and from various incoherent scatter radars, *J. Geophys. Res.*, **78**, 197–205, 1973.

McEntire, R.W., E.P. Keath, D.E. Fort, A.T.Y. Lui, and S.M. Krimigis, The Medium-Energy Particle Analyzer (MEPA) on the AMPTE CCE Spacecraft, *IEEE Trans. Geosci. Remote. Sens.*, **GE-23**, 230–233, 1985.

McFadden, J.P., C.W. Carlson, R.E. Ergun, F.S. Mozer, M. Temerin, W. Peria, D.M. Klumpar, E.G. Shelley, W.K. Peterson, E. Möbius, L. Kistler, R. Elphic, R. Strangeway, C. Cattell, and R. Pfaff, Spatial structure and gradients of ion beams observed by FAST, *Geophys. Res. Lett.*, **25**, 2021–2024, 1998a.

McFadden, J.P., C.W. Carlson, R.E. Ergun, C.C. Chaston, F.S. Mozer, M. Temerin, D.M. Klumpar, E.G. Shelley, W.K. Peterson, E. Möbius, L. Kistler, R. Elphic, R. Strangeway, C. Cattell, and R. Pfaff, Electron modulation and ion cyclotron waves observed by FAST, *Geophys. Res. Lett.*, **25**, 2045–2048, 1998b.

McFadden, J.P., C.W. Carlson, R.E. Ergun, D.M. Klumpar, and E. Möbius, Ion and electron characteristics in auroral density cavities associated with ion beams: No evidence for cold ionospheric plasma, *J. Geophys. Res.*, **104**, 14671–14682, 1999.

Miller, K.L., W.C. Knudsen, and K. Spenner, The dayside Venus ionosphere. I. Pioneer Venus retarding potential analyzer experimental observations, *Icarus*, **57**, 386–409, 1984.

Moore, T.E., D.J. Chornay, M.R. Collier, F.A. Herrero, J. Johnson, M.A. Johnson, J.W. Keller, J.F. Laudadio, J.F. Lobell, K.W. Ogilvie, P. Rozmarynowski, S.A. Fuselier, A.G. Ghielmetti, E. Hertzberg, D.C. Hamilton, R. Lundgren, P. Wilson, P. Walpole, T.M. Stephen, B.L. Peko, B. van Zyl, P. Wurz, J.M. Quinn, and G.R. Wilson, The low-energy neutral atom imager for IMAGE, *Space Sci. Rev.*, **91**, 155–195, 2000.

Morrow, M.L., W.H. Morrow, and L.N. Majorana, UV and VUV sources for in-flight calibration of space experiments, Space Astronomical Telescopes and Instruments II, *Proc. SPIE*, **1945**, 478–483, 1993.

Mukai, T., S. Machida, Y. Saito, M. Hirahara, T. Terasawa, N. Kaya, T. Obara, M. Ejiri, and A. Nishida, The Low Energy Particle (LEP) instrument onboard the Geotail satellite, *J. Geomag. Geoelectr.*, **46**, 669–692, 1994.

Niemann, H.B., J.R. Booth, J.E. Cooley, R.E. Hartle, W.T. Kasprzak, N.W. Spencer, S.H. Way, D.M. Hunten, and G.R. Carignan, Pioneer Venus Orbiter neutral gas mass spectrometer experiment, *IEEE Trans. Geosci. Electr. Remote Sens.*, **GE-18**, 60–65, 1980a.

Niemann, H.B., W.T. Kasprzak, A.E. Hedin, D.M. Hunten, and N.W. Spencer, Mass Spectrometric Measurements of the Thermosphere and Exosphere of Venus, *J. Geophys. Res.*, **85**, 7817–7827, 1980b.

Niemann, H.B., S. Atreya, S.J. Bauer, K. Biemann, B. Block, G. Carignan, T. Donahue, L. Frost, D. Gautier, D. Harpold, D. Hunten, G. Israel, J. Luhnine, K. Mauersberger, T. Owen, F. Raulin, J. Richards, and S. Way, The gas chromatograph mass spectrometer aboard Huygens, *ESA Special Publication*, **SP-1177**, ESA Publications Division, Noordwijk, 1997.

Niemann, H.B., S.K. Atreya, S.J. Bauer, K. Biemann, B. Block, G.R. Carignan, T.M. Donahue, R.L. Frost, D. Gautier, J.A. Haberman, D. Harpold, D.M. Hunten, G. Israel, J.I. Luhnine,

K. Mauersberger, T.C. Owen, F. Raulin, J.E. Richards, and S.H. Way, The gas chromatograph mass spectrometer for the Huygens Probe, *Space Sci. Rev.*, **104**, 553–591, 2002.

Nier, A.O., W.E. Potter, D.R. Hickman, and K. Maurersberger, The open-source neutral-mass spectrometer on Atmosphere Explorer-C, -D, and -E, *Radio Sci.*, **8**, 271–276, 1973.

Oberheide, J., P. Wilhelms, and M. Zimmer, New results on the absolute ion detection efficiencies of a microchannel plate, *Meas. Sci. Technol.*, **8**, 351-354, 1997.

Ogilvie, K.W., D.J. Chornay, R.J. Fritzenreiter, F. Hunsaker, J. Keller, J. Lobell, G. Miller, J.D. Scudder, E.C. Sittler, R.B. Torbert, D. Bodet, G. Needell, A.J. Lazarus, J.T. Steinberg, J.H. Tappan, A. Mavretic, and E. Gergin, SWE, A comprehensive plasma instrument for the Wind spacecraft, *Space Sci. Rev.*, **71**, 55–77, 1995.

Outlaw, R.A. and R.E. Stell, An In-Situ, Metal-Gas, Secondary Standard Assembly for Ultrahigh-Vacuum Instrumentation, *J. Vac. Sci. Technol.*,**8**, 608–610, 1971.

Paschmann, G., H. Loidl, P. Obermayer, M. Ertl, P. Laborenz, N. Sckopke, W. Baumjohann, C.W. Carlson, and D.W. Curtis, The plasma instrument for AMPTE IRM, *IEEE Trans. Geosci. Remote Sens.*, **GE-23**, 262–266, 1985.

Peart, B. and M.F.A. Harrison, Measurements of the ion detection efficiencies of Johnston electron multipliers, *J. Phys. E: Sci. Instrum.*, **14**, 1374, 1981.

Rème, H., F. Cotin, A. Cros, J.L. Medale, and J.-A. Sauvaud, The Giotto electron plasma experiment, *J. Phys. E - Sci. Instrum.*, **20**, 721–731, 1987.

Rème, H., M. Bosqued, J.A. Sauvaud, A. Dros, J. Dandouras, C. Aoustin, Ch. Martz, J.L. Medale, J. Rouzaud, E. Möbius, K. Crocker, M. Granoff, L.M. Kistler, D. Hovestadt, B. Klecker, G. Paschmann, M. Ertl, E. Künneth, C.W. Carlson, D.W. Curtis, R.P. Lin, J.P. McFadden, J. Croyle, V. Formisano, M. Di Lellis, R. Bruno, M.B. Bavassano-Cattaneo, B. Baldetti, G. Chionchio, E.G. Shelley, A.G. Ghielmetti, W. Lennartsson, A. Korth, H. Rosenbauer, I. Szemerey, R. Lundin, S. Olsen, G.K. Parks, M. McCarthy, and H. Balsiger, The Cluster ion spectrometry experiment, Cluster: Mission, Payload and Supporting Activities, W. R. Burke, Ed., European Space Agency, Paris, *ESA Special Publication*, **SP-1159**, ESA Publications Division, Noordwijk, 133–161, 1993.

Rème, H., J.M. Bosqued, J.A. Sauvaud, A. Cros, J. Dandouras, C. Aoustin, J. Bouyssour, Th. Camus, J. Cuvilo, C. Martz, J.L. Medale, H. Perrier, D. Romefort, J. Rouzaud, C. d'Uston, E. Möbius, K. Crocker, M. Granoff, L.M. Kistler, M. Popecki, D. Hovestadt, B. Klecker, G. Paschmann, M. Scholer, C.W. Carlson, D.W. Curtis, R.P. Lin, J.P. McFadden, V. Formisano, E. Amata, M.B. Bavassano-Cattaneo, P. Baldetti, G. Belluci, R. Bruno, G. Chionchio, A. Di Lellis, E.G. Shelley, A.G. Ghielmetti, W. Lennartsson, A. Korth, H. Rosenbauer, R. Lundin, S. Olsen, G.K. Parks, M. McCarthy, and H. Balsiger, The Cluster Ion Spectrometer (CIS) experiment, *Space Sci. Rev.*, **79**, 303–350, 1997.

Robertson, D.W., Building a new kind of graded-Z shield for Swift's burst alert telescope, *Proc. SPIE*, **4851**, 1374–1381, 2003.

Rosenbauer, H., R. Schwenn, H. Miggenrieder, B. Meyer, H. Grünwaldt, K.-H. Mühlhäuser, H. Pellkofer, and J.H. Wolfe, Die Instrumente des Plasmaexperiments auf den HELIOS-Sonnensonden, **BMFT-FB-W 81-015**, Max-Planck-Institut für Aeronomie, Katlenburg-Lindau, 1981.

Rymer, A.M., A.J. Coates, K. Svenes, G.A. Abel, D.R. Linder, B. Narheim, M. Thomsen, and D.T. Young, Cassini Plasma Spectrometer Electron Spectrometer measurements during the Earth swing-by on August 18, 1999, *J. Geophys. Res*, **106**, 30117–30198, 2001.

Sauvaud, J.-A., R. Lundin, H. Rème, J.P. McFadden, C. Carlson, G.K. Parks, E. Möbius, L.M. Kistler, B. Klecker, E. Amata, A.M. Di Lellis, V. Formisano, J.M. Bosqued, I. Dandouras, P. Décréau, M. Dunlop, L. Eliasson, A. Korth, B. Lavraud, and M. McCarthy, Intermittent thermal plasma acceleration linked to sporadic motions of the magnetopause, first Cluster results, *Ann. Geophys.*, **19**, 1523–1532, 2001.

Schwenn, R., H. Rosenbauer, and H. Miggenrieder, The plasma experiment on board Helios, *Raumfahrtforschung*, **19**, 226–232, 1975.

Scialdone, J.J., Self-Contamination and Environment of an Orbiting Satellite,*J. Vac. Sci. Technol.*, **9(2)**, 1007–1015, 1972.

Scialdone, J.J., A.E. Hedin, and C.J. Rice, Comparison of Satellite Self-Contamination Experiments and Scattering Return Flux Calculations, *J. Geophys. Res.*, **83**(A1), 195–198, 1978.

Scudder, J.D., F. Hunsaker, G. Miller, J. Lobell, T. Zawistowski, K.W. Ogilvie, J. Keller, D. Chornay, F. Herrero, R. Fitzenreiter, D. Fairfield, J. Needell, D. Bodet, J. Googins, C. Kletzing, R. Torbert, J. Vandiver, R. Bentley, W. Fillius, C. McIlwain, E. Whipple, and A. Korth, Hydra - A 3-Dimensional Electron and Ion Hot Plasma Instrument for the Polar Spacecraft of the GGS Mission, *Space Sci. Rev.*, **71**, 459–495, 1995.

Scudder, J.D., P.A. Puhl-Quinn, F.S. Mozer, K.W. Ogilvie, and C.T. Russell, Generalized Walén tests through Alfvén waves and rotational discontinuities using electron flow velocities, *J. Geophys. Res.*, **104**, 19817–19834, 1999.

Scudder, J.D., X. Cao, and F.S. Mozer, Photoemission current-spacecraft voltage relation: Key to routine, quantitative low-energy plasma measurements, *J. Geophys. Res.*, **105**, 21281–21294, 2000.

Seki, K., M. Nirahara, M. Hoshino, T. Terasawa, R.C. Elphic, Y. Saito, T. Mukai, H. Hayakawa, H. Kojima, and H. Matsumoto: Cold ions in the hot plasma sheet of Earth's magnetotail, *Nature*, **422**, 589–592, 2003.

Sharber, J.R., R. Link, R.A. Frahm, J.D. Winningham, D. Lummerzheim, M.H. Rees, D.L. Chenette, and E.E. Gaines, Validation of UARS particle environment monitor electron energy deposition, *J. Geophys. Res.*, **101**, 9571–9582, 1996.

Shelley, E.G., R.D. Sharp, R.G. Johnson, J. Geiss, P. Eberhardt, H. Balsiger, G. Haerendel, and H. Rosenbauer, Plasma composition experiment on ISEE-A, *IEEE Trans. Geosci. Electr.*, **GE-16**, 266–270, 1978.

Smart, D.F. and M.A. Shea, Galactic cosmic radiation and solar energetic particles, in *Handbook of Geophysics and the Space Environment*, A. S. Jursa, Ed., National Technical Information Service, Springfield, VA,, 6-1 – 6-29, 1985.

Stassinoupoulos, E.G., High-Energy Radiation Background in Space, A.C. Rester and J.I. Trombka, Eds., *AIP Conf. Proc.*, **186**, American Institute of Physics, New York, 1989.

Stickel, R.E., Jr., F.G. Kellert, K.A. Smith, F.B. Dunning, and R.F. Stebbings, Low energy ion counting efficiency of a Johnston electron multiplier, *Rev. Sci. Instrum.*, **51**, 396–397, 1980.

Strangeway, R.J., L. Kepko, R.C. Elphic, C.W. Carlson, R.E. Ergun, J.P. McFadden, W.J. Peria, G.T. Delory, C.C. Chaston, M. Temerin, C.A. Cattell, E. Möbius, L.M. Kistler, D.M. Klumpar, W.K. Peterson, E.G. Shelley, and R.F. Pfaff, FAST observations of VLF waves in the auroral zone: Evidence of very low plasma densities, *Geophys. Res. Lett.*, **25**, 2065–2068, 1998.

Su, Y.J., J.L. Horwitz, T.E. Moore, B.L. Giles, M.O. Chandler, P.D. Craven, M. Hirahara, and C.J. Pollock, Polar wind survey with the thermal ion dynamics experiment plasma source instrument suite aboard POLAR, *J. Geophys. Res.*, **103**, 29305–29337, 1998.

Thorness, R.B. and A.O. Nier, Device for Remote Opening of a Vacuum System, *Rev. Space Sci. Instrum.*, **3**3, 1005–1007, 1962.

Tsuruda, K., H. Hayakawa, M. Nakamura, T. Okada, A. Matsuoka, F.S. Mozer, and R. Schmidt, Electric field measurements on the GEOTAIL satellite, *J. Geomag. Geoelectr.*, **46**, 693–671, 1994.

Vallat, C., I. Dandouras, P.C. Brandt, R. DeMajistre, D.G. Mitchell, E.C. Roelof, H. Rème, J.-A. Sauvaud, L. Kistler, C. Mouikis, M. Dunlop, and A. Balogh, First comparisons of local ion measurements in the inner magnetosphere with energetic neutral atom magnetospheric image inversions: Cluster-CIS and IMAGE-HENA observations, *J. Geophys. Res.*, **109**, A04213, doi:10.1029/2003JA010224, 2004.

von Zahn, U., F.-J. Lubken, and C. Putz, BUGATTI experiments: Mass spectrometric studies of lower thermosphere eddy mixing and turbulence, *J. Geophys. Res.*, **95**, 7443–7465, 1990.

Waite, Jr., J.H., W.S. Lewis, W.T. Kasprzak, V.G. Anicich, B.P. Block, T.C. Cravens, G.G. Fletcher, W.-H. Ip, J.G. Luhmann, R.L. McNutt, H.B. Niemann, R.L. Thorpe, and R.V. Yelle, The Cassini Ion and Neutral Mass Spectrometer (INMS) investigation, *Space Sci. Rev.*,**114**, 113–231, 2004.

Weiss, W. and B. Wilken, The Giotto implanted ion spectrometer, (ISS): Principles of the electronic operation and data collection, *J. Phys. E: Sci. Instrum.*, **20**, 1510–1516, 1987.

Wilken, B., W.I. Axford, I. Daglis, P. Daly, W. Güttler, W.H. Ip, A. Korth, G. Kremser, S. Livi, V.M. Vasyliunas, J. Woch, D. Baker, R.D. Belian, J.B. Blake, J.F. Fennell, L.R. Lyons, H. Borg, T.A. Fritz, F. Gliem, R. Rathje, M. Grande, D. Hall, K. Kecsuemety, S. McKenna-Lawlor, K. Mursula, P. Tanskanen, Z. Pu, I. Sandahl, E.T. Sarris, M. Scholer, M. Schultz, F. Søraas, and S. Ullaland, RAPID, The imaging energetic particle spectrometer on Cluster, *Space Sci. Rev.*, **79**, 399–473, 1997.

Williams, D.J., R.W. McEntire, S. Jaskulek, and B. Wilken, The Galileo energetic particle detector, *Space Sci. Rev.*, **60**, 385–412, 1992.

Williams, D.J., R.W. McEntire, C. Schlemm, A.T.Y Lui, G. Gloeckler, S.P. Christon, and F. Gliem, Geotail energetic particles and ion composition instrument, *J. Geomag. Geolectr.*, **46**, 39–57, 1994.

Witte, M., H. Rosenbauer, E. Kepler, H. Fahr, P. Hemmerich, H. Lauche, A. Loidl, and R. Zwick, The interstellar neutral-gas experiment on Ulysses, *Astron. Astrophys. Suppl. Ser.*, **92**, 333–348, 1992.

Witte, M., M. Banaszkiewicz, H. Rosenbauer, and D. McMullin, Kinetic temperature of interstellar neutral helium: updated results from the Ulysses/GAS-instrument, *Adv. Space Res.*, **34** 61–65, 2004.

Wüest, M. and P. Bochsler, Simulation of ion backscattering from rough surfaces, *Nucl. Instrum. Methods B*, **71**, 314–323, 1992.

Wurz, P., Detection of energetic neutral particles, in *The Outer Heliosphere: Beyond the Planets*, K. Scherer, H. Fichtner, and E. Marsch, Eds., Copernicus Gesellschaft e.V., Katlenburg-Lindau, 251–288, 2000.

Wurz, P., J. Scheer, and M. Wieser, Particle scattering off surfaces: application in space science, *J. Surf. Sci. Nanotechn.*, **4**, 394–400, 2006.

Young, D.T., J.E. Nordholt, and J.J. Hanley, Plasma Experiment for Planetary Exploration (PEPE), DS1 Technology Validation Reports, JPL Publication, **00-10**, Pasadena, CA, 2000.

Zurbuchen, T.H., P. Bochsler, and F. Scholze, Reflection of ultraviolet light at 121.6 nm from rough surfaces, *Opt. Eng.*, **34**, 1303–1315, 1995.